Molecular thin films: characterization, control, and collection of light

Jessica M Topple
Department of Physics
McGill University

July 2011

A thesis submitted to McGill University in partial fulfilment of the requirements of the degree of Ph.D.

Abstract

Deposition of submonolayer coverages of 3,4,9,10-perylenetetracarboxylic diimide (PTCDI) onto NaCl(001) results in the bimodal growth of coexisting square and needle-shaped islands. The epitaxy of each island type was determined from molecular and atomic resolution non-contact atomic force microscopy (NC-AFM) images. Post-deposition, the needle islands grow while the square islands disappear completely within days. This is characterized as a dewetting transition, the dynamics of which has been described and empirically fit to the monomolecular growth model, a model typically applied to biological growth.

Methods of tailoring molecular thin film morphology and maturation rate were investigated. The island surface distribution, size, shape, and rate of dewetting of submonolayer coverages of PTCDI on alkali halides may be varied by changing growth conditions such as temperature and by templating the substrate with single atomic layer deep pits or depositing gold nanoclusters to modify island nucleation. This characterization is an important step in controlling the structure of thin organic films for devices that are sensitive to nanoscale film structure.

Film morphology of organic photovoltaic materials can have a dramatic influence on device performance. Building upon previous morphological studies of tailoring molecular island size and nucleation site distribution, thin films of PTDCI (an electron donor) and copper (II) phthalocyanine (an electron acceptor) molecular islands were grown under ultra high vacuum conditions. Topography and surface contact potential were simultaneously mapped in a preliminary NC-AFM and Kelvin probe force microscopy study investigating structure-function relationships in photovoltaic energy generation.

Résumé

Le dépôt de sous-couche simples de 3,4,9,10-pérylénetetracarboxylic diimide (PTCDI) sur du NaCl (001) résulte en une croissance bimodale d'îles en formes d'aiguille et de carré. L'épitaxie de chaque type d'île a été déterminé par imagerie microscopique á force atomique non-contact (NC-AFM) avec des résolutions atomiques et moléculaires. Aprés le dépôt, les îles en forme d'aiguille croissent tandis que les îles de forme de carrés disparaissent complètement en quelques jours. Ceci est caractérisé par une transition de démouillage, pour laquelle la dynamique a été décrite et empiriquement ajusté au modèle de croissance mono-moléculaire, un modèle généralement appliqué aux croissances biologiques.

Les méthodes d'adaptation de la morphologie des couches moléculaires minces et le taux de maturation ont été étudiés. La distribution de surface, la taille et la forme des îles, ainsi que le taux de démouillage des sous-couche simples de PTCDI sur les alkali-halides peuvent être modifiés en changeant les conditions de croissance telles que la température, en remodelant le substrat avec des trous profonds d'épaisseur atomique ou en déposant des nano-amas d'or pour modifier la nucléation des îles. Cette caractérisation est une étape importante pour le contrôler la structure des films organiques fins pour des appareils qui sont sensibles à la structure des films aux échelles nanoscopiques.

La morphologie des films de matériaux organiques photovoltaïques peut avoir une influence importante sur la performance de ces appareils. En s'appuyant sur des études antérieures portant sur l'adaptation de la taille des îles moléculaires et la répartition des sites de nucléation, des films minces d'îles de PTDCI (un donneur d'électrons) et de cuivre (II) phthalocyanine (un accepteur d'électrons) ont été cultivés sous ultra haut vide. La topographie et le potentiel de contact à la surface ont été cartographié simultanément dans une étude préliminaire de microscopies NC-AFM et sonde Kelvin pour caractériser les relations entre la structure et la fonction de la génération d'énergie photovoltaïque.

Acknowledgements

I thank my supervisor Peter Grutter for encouragement, guidence and advice. I thank Sarah Burke for patiently answering a barrage of questions and teaching me how to do just about everything in the lab. I thank Shawn Fostner for his help and for staying level headed through our instrumentation trials and tribulations. I thank Antoni Tekiel for his knowledge and careful attention to detail - the JEOL will be left in good hands. I thank Lynda Cockins for being a great sounding board and for her help with Kelvin probe. I thank Yoichi Miyahara for his excellent technical assistance and expertise. I thank the rest of the Grutter group for discussions, comraderie, and many interesting pizza lunches.

I thank Wei Ji for theory work on molecular diffusion, Roland Bennewitz for helpful discussion on the surface structure of alkali halides, Jody McGuire for explaining the chemistry of triplet states to me, and Chris Godbout for insights on the catalytic formation of graphene. I thank John Smeros and Robert Gagnon for keeping everything running smoothly, and especially for helping solve the mystery of the leaking quartz crystal monitor. I thank my summer students David Daivasagaya and Benjamin Bensoussan for their hard work processing images, and Sebastien Guillots for editing my résumé. I thank Steve Kecani and Pascal Bourseguin for machine shop work, and Elizabeth Shearon, Sonia Viera, Louise Decelles, Paula Domingues and Eddie Del Campo for help in the office. For financial support, I acknowledge NSERC and The Walter Sumner Foundation.

I thank my family for encouraging me and always seeming interested in my work. I thank my brother Ben for inspiring and helping me to present some images in an artistic way. Finally, I thank Jeff Bates. You have been the most amazing best friend, study buddy, lab-mate, husband and hockey coach I could ever have asked for.

Statement of Originality

The author, JT, claims the following aspects of the work contained herein constitute original scholarship and an advancement of knowledge. Some results have led to publications, noted with corresponding citations. Specific contributions include:

- The previously unexplored growth behaviour of of the prototypical organic molecule PTCDI when deposited on alkali halide substrates NaCl and KBr was thoroughly characterized.
- The unique dynamical dewetting behaviour of PTCDI deposited on NaCl warranted a publication [J.M. Topple, S.A. Burke, S. Fostner and P. Grutter, *Thin film evolution: Dewetting dynamics of a bimodal molecular system*. Phys. Rev. B, 79(20), 205414, (2009)]
- Methods of tailoring thin film morphology and maturation rate were explored by altering substrate structure and growth conditions, detailed in a further publication [J. M. Topple, S. A. Burke, W. Ji, S. Fostner, A. Tekiel, and P. Grutter, *Tailoring the morphology and dewetting of an organic thin film*. J. Phys. Chem. C, 115(1), 217-224 (2011)]
- Though PTCDI has been used as an electron acceptor molecule elsewhere, the study of ultra thin films of it in conjunction with electron donor molecule CuPc by KPFM is a unique and exciting step in organic photovoltaic research.

Contributions of Co-authors

I gratefully acknowledge the support and assistance of my co-authors, whose contributions to publications are described below.

- J.M. Topple, S.A. Burke, S. Fostner and P. Grutter, *Thin film evolution: Dewetting dynamics of a bimodal molecular system*. Phys. Rev. B, 79(20), 205414, (2009). *Appears in Chapter 2*

  S.A. Burke provided experimental guidance, assistance in the structure calculations of Table 1, and helped complete the published versions of Figures 1 and 3. All authors discussed interpretation of experimental analysis and article goals. All co-authors gave feedback, editing, suggestions and support during the writing of this article.
- J. M. Topple, S. A. Burke, W. Ji, S. Fostner, A. Tekiel, and P. Grutter, *Tailoring the morphology and dewetting of an organic thin film*. J. Phys. Chem. C, 115(1), 217-224 (2011). *Appears in Chapter 3*

  All co-authors gave feedback during the writing process of this article, in particular S.A. Burke provided substantial editing and suggestions for re-writes. W. Ji performed the diffusion energy barrier calculations.

Contents

List of Figures

List of Tables

1

Introduction

1.1 Motivation

1.1.1 Organic Electronics

The field of organic electronics uses molecules as the building blocks of a wide range of organic electronic and optoelectronic applications, including organic field effect transistors (OFETS), organic light emitting diodes (OLEDS), sensors, rectifying junctions, single molecule devices, non-linear optics and photovoltaics. The interesting optical and electronic properties of certain organic molecules advocate their use in such applications [1–3]. To this end, thin film growth of a variety of molecules on different substrates has been studied [4, 5]. Perylene derivatives are one such class of organic semiconducting molecules which are easily modified [6–15], and this thesis investigates the controlled growth of 3,4,9,10-perylenetetracarboxylic diimide (PTCDI). The morphology of thin films critically determines application relevant properties, and can be controlled during growth to some degree by experimental parameters [2,16]. However, post-growth dynamics may change the film structure and resulting properties.

Figure 1.1: Solar energy at McGill University: BigBelly Solar Compactor waste disposal on campus

1.1.2 Organic Photovoltaics

Organic photovoltaics (OPVs) is an exciting application of molecular electronics initiated by Weinberger and coworkers in 1981 [17]. In the search for sustainable methods of energy harvesting, solar cells hold a great deal of promise. The sun irradiates the earth with an annual average of about 180 W/m^2 of solar energy reaching the surface of the earth [18], which summed over the surface of the earth amounts to 2.9 x 10^{24} J annually. This is substantial compared to the projected 2011 global consumption of 5.5 x 10^{20} J [19]. However, capturing solar energy is a complex and inefficient process that still requires significant research and development. The solar photovoltaics industry grew by an order of magnitude from 2000 to 2009 [20]. In 2010, solar energy provided 1.2 x 10^{17} J of the United States total national energy supply of 1.0 x 10^{20} J [21], or about 0.1%. State of the art inorganic solar cells have reached a reported efficiency of 43.5% (Solar Junction) as of April, 2011. These devices are expensive and require the use of hazardous materials during fabrication. Organic solar cells hold promise as a cheap and safe alternative, but must overcome additional efficiency and reliability challenges to become a viable means of solar energy harvesting. Commercial organic solar cells have lagged in development, recently reaching efficiencies of 8.3% (Konarka) [22]. Recent findings indicate the functionality of organic photovoltaics is strongly dependent on morphology [23], particularly at interfaces between active materials. These materials are typically amorphously grown from solution and characterized under ambient conditions using ensemble optical and electronic techniques that reveal the average behaviour. High-resolution scanning probe performed on clean materials grown under ultra high vacuum conditions is presently an un-exploited technique with great potential for correlating the nanostructured morphology with fundamental physical processes in photoharvesting.

1.2 Background

1.2.1 Thin Film Growth

Studies of crystal growth kinetics date back to the classic 1951 article by Burton, Cabrera and Frank, known as “The BCF Paper” [24], and the popular 2000 book by Venables [25] gives a detailed overview of the subject.

Thin film growth can be described by a series of consecutive atomistic processes, illustrated in Fig.1.2. Additional considerations (such as added degrees of freedom) are needed to fully describe molecular thin film growth that will be neglected at present and revisited in Chapter 2. First, film particles arrive at a surface from some deposition source (such as thermal evaporation, sputtering, molecular beam epitaxy or chemical vapour deposition). The incident particles will either reflect, temporarily interact with the surface and then re-evaporate, or stick to the surface (adsorption). Adsorbed particles may stay in one place or may diffuse (hop along adjacent adsorption sites) across the surface until finding a more favourable binding site (such as a defect). Multiple adsorbed particles may diffuse into one another (coincidence), and may stick together to nucleate an island if the critical number of particles are present to make this energetically favourable. Film growth proceeds from here. The driving force for all surface dynamics is the minimization of free energy of the system, which depends on the thermodynamic balance of surface, bulk and interfacial stresses and energies.

Several film growth modes exist near thermodynamic equilibrium, as illustrated in Fig.1.3. In *layer-by-layer (Frank-van der Merwe) growth*, a complete layer forms before the next layer begins, because adatoms interact more strongly with the substrate than one another. In *island (Volmer-Webber) growth*, three dimensional (3D) islands are formed, because adatoms interact strongly with each other but weakly with the substrate. In *layer-plus-island (Stranski-Krastinov) growth*, wetting layer(s) form first, with 3D islands on top. This is because adatoms interact strongly with the substrate to form strained lower layers, but farther from the substrate this interaction is reduced, and adatom-adatom interactions dominate to create islands.

Island growth can be further characterized by the shapes and structures formed, which depend on the dynamics of the system and growth conditions. Ad-

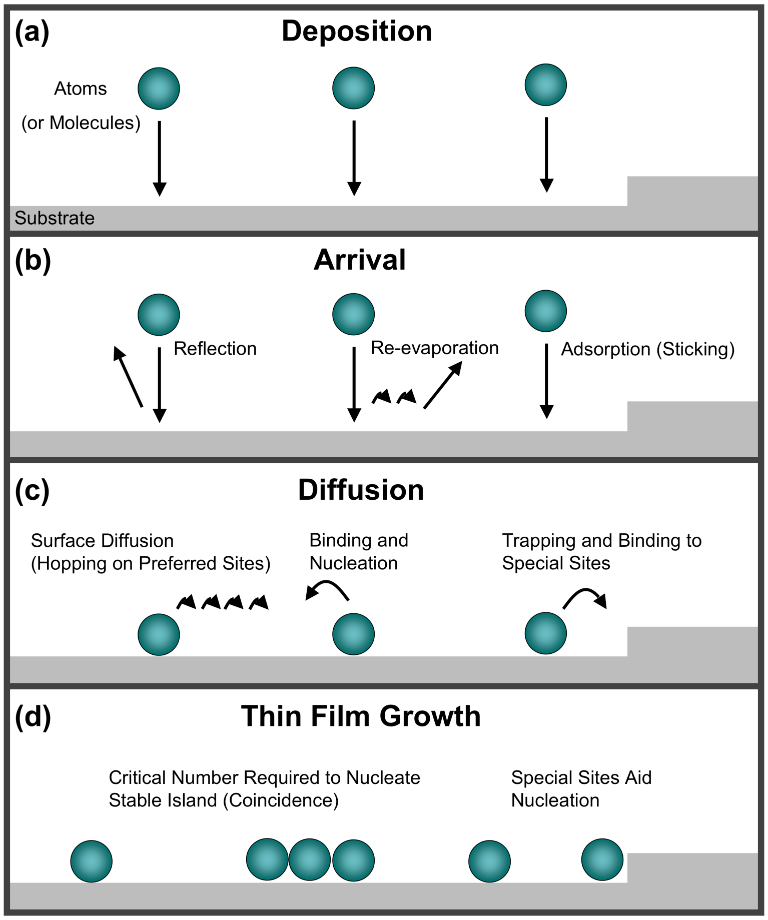

Figure 1.2: Atomistic processes of early film growth

sorbates coincident on islands may join the island if it is energetically favourable to do so, and may diffuse to reach a more stable site within the island if it has the time and energy to relax. Site stability depends on the number of nearest neighbours an adsorbate has (coordination number). Zhang and Lagally [26] define four island growth regimes as follows: In *the hit and stick diffusion limited aggregation growth regime*, adatoms do not have the energy or time needed to relax before being pinned by more adatoms, resulting in fractal islands with thin branches (width on the order of one adsorbate). This growth mode is not generally observed experiment-

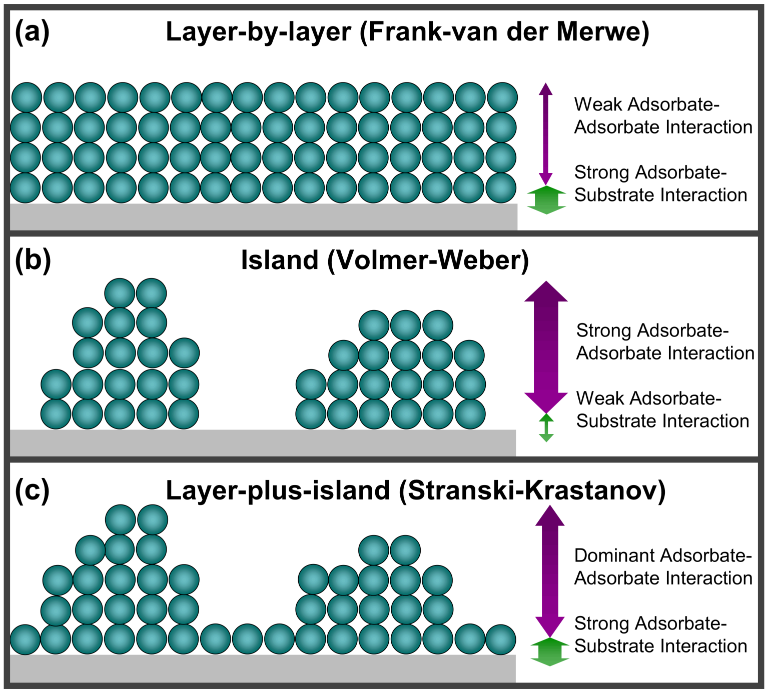

Figure 1.3: Near equilibrium thin film growth modes

ally. In *the extended fractal growth regime*, arriving adatoms relax to find at least two nearest neighbours, resulting in fractal islands with thicker branches (width on the order of four adsorbates). This growth mode is defined for triangular lattices but not square lattices. In *the island-corner barrier effect growth regime*, adatoms can diffuse along edges but not around corners, producing fractal islands with branch thicknesses depending on the diffusion rate. In *the compact island growth regime*, all corners can be crossed easily by adatoms. On triangular lattices this corresponds to at least two nearest neighbours and on square lattices at least three. The island shape is determined by competition between different step orientation energetics and may be influenced by the substrate.

Films may continue to evolve as a function of time even after deposition

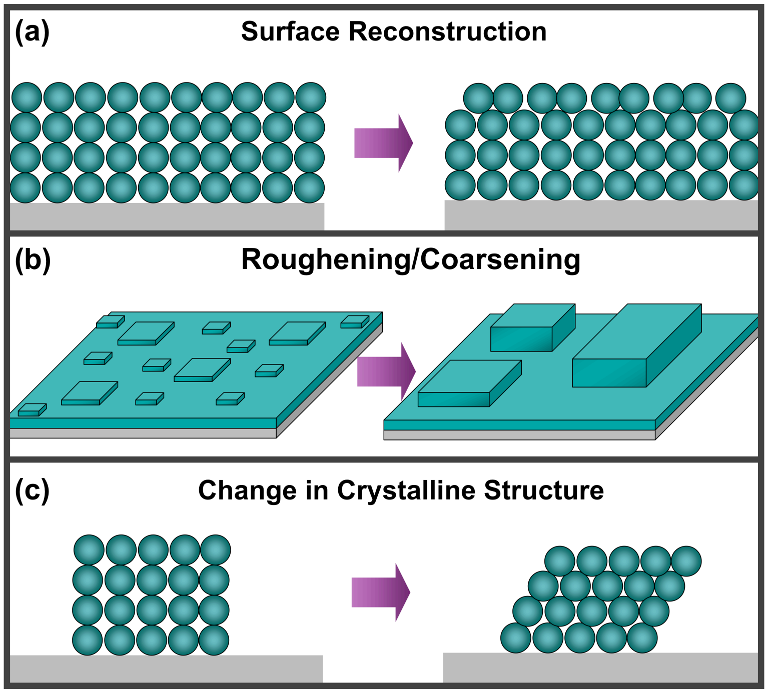

Figure 1.4: Post-deposition film ripening processes

is complete. *Ripening* involves the redistribution of adsorbates, driving the system towards a minimum free energy. Some examples are illustrated in Fig.1.4. Surface reconstructions can change the structure of the top layer(s) of atoms or molecules in a film (often to reduce the number of dangling bonds). Film *coarsening* or *roughening* is a form of ripening that can decrease film continuity and is often regarded as an undesirable degradation process for electronic and optical devices. Frequently, large islands or clusters grow at the expense of smaller ones (sometimes referred to as *Ostwald Ripening*). In some cases, this redistribution of adsorbates is associated with a change in crystalline structure. Fig.1.5 illustrates some of the processes which take place within individual islands. *Interlayer mass transport* is the process by which adsorbates from lower layers (which may

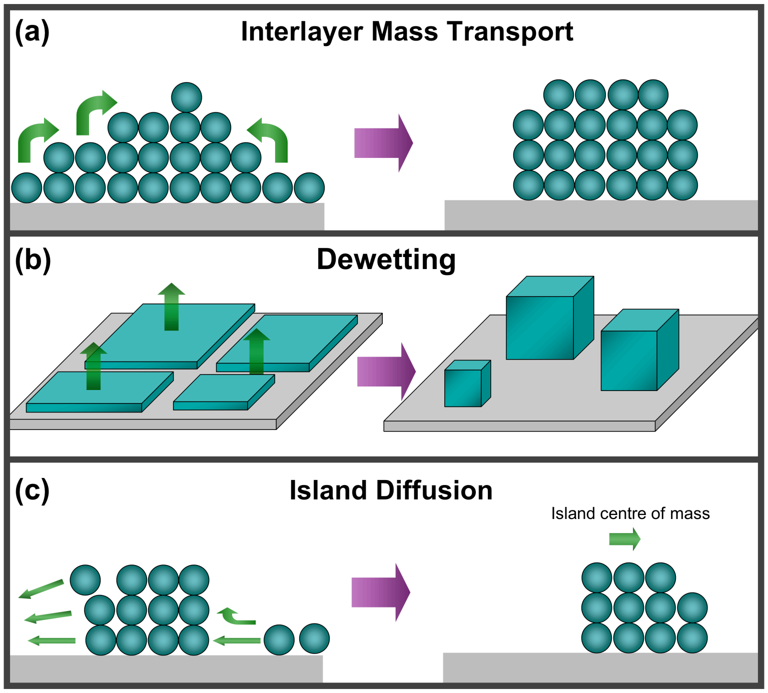

Figure 1.5: Island ripening processes

be strained due to substrate interactions) diffuse vertically to join upper layers. *Dewetting* is the specific case of interlayer mass transport in which molecules from the lowest (wetting) layer (which may or may not be a continuous film depending on deposition coverage and rate) rearrange to form islands. Dewetting can be associated with a structural change, as is exhibited by PTCDI deposited on NaCl and will be discussed in detail in Chapter 2. *Island diffusion* takes place when adsorbates are not stably bonded and can escape and diffuse between neighbouring islands and across the film surface. If the centre of mass of an island changes position, the island is said to have diffused. Island diffusion can be Brownian (random and temperature dependent) or directional in some specific cases where adsorbate diffusion is not uniform (also observed for PTCDI on NaCl, see Appendix A).

1.2.2 Atomic Force Microscopy

Atomic force microscopy (AFM) is a form of scanning probe microscopy (SPM) capable of atomic resolution imaging, developed by Binnig, Quate and Gerber in 1986 [27].

A sharp tipped *cantilever* is scanned over a sample surface in a manner similar to a turntable needle (stylus) on a record (see Fig.1.6). However, instead of using the tip deflection signal to actuate a speaker and produce sound, it is used to create a topographic map of the sample surface. The probe must be sharp in order to minimize feature broadening (tip convolution) in the resulting image.

Figure 1.6: Turntable stylus used to read audio track on records. *Photo credit: Ben Topple*

The *cantilever deflection signal* can be recorded in several ways. The most common method is by measuring the deflection of a laser beam reflected off the back of the cantilever surface with a quadrant photodetector [28], and is used for all experiments herein. The beam is aligned such that the signal recorded by the position sensitive photodetector can detect motion both along the cantilever axis and perpendicular to it [29]. Other detection methods include optical interferometry [30], and less commonly the use of piezoresistive cantilevers [31], capacitive sensing [32] and the original STM scheme used to detect tunnelling current in the first AFM [27].

Relative motion of the tip raster scanning across the sample surface is usually achieved by a piezoelectric tube scanner. AFM imaging can be done in either constant height or constant force mode (see Fig.1.7). In *constant height mode*, the cantilever is raster scanned in an xy-plane above the sample surface, and changes to the tip deflection signal are recorded as a function of position. In *constant force mode* (sometimes called topography mode [33], a feedback circuit is used to control the z-position of the tip (the distance normal to the sample surface plane, or "height") in order to maintain a constant tip deflection signal during scanning, and changes to z position are recorded as a function of position. Both modes have advantages and limitations. Constant force mode is rate limited by the response time of the feedback circuit, while constant height mode is sensitive to topographic artifacts and therefore only appropriate for samples that are flat relative to the tip-sample separation distance. Constant force mode is used herein, though we shall see later that our application is further specified as constant force *gradient* mode.

There are three main AFM imaging modes: contact mode, tapping mode, and non-contact mode. In *contact mode*, the AFM tip is brought into contact (repulsive interaction, discussed further below) with the sample surface, and the static cantilever deflection is measured and/or used for feedback (depending whether in constant height or constant force mode). This mode is sensitive to low frequency noise, drift and wear to both tip and sample. In *tapping mode* [34] (also called in-

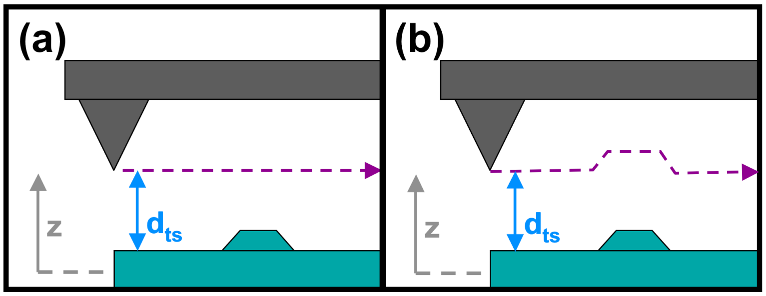

Figure 1.7: AFM imaging cantilever scan motion in (a) constant height and (b) constant force mode

termittent contact mode), the cantilever is oscillated by a piezo element at an amplitude on the order of 100 nm and the cantilever oscillation amplitude is measured and/or used for feedback as the tip "taps" across the surface. The tip reaches the repulsive force regime (see Fig.1.8) close to the surface, decreasing the cantilever oscillation amplitude. The associated decrease in lateral friction (dragging) forces on the tip during tapping mode reduces wear, but the apex will still be be blunted during imaging. Tapping mode is particularly useful for samples in ambient conditions, under which a water meniscus forms in surfaces. In *non-contact mode (NC-AFM)* [35], the cantilever is oscillated at a smaller amplitude (typically under 10 nm) and the oscillation amplitude and resonance frequency are measured and/or used for feedback in *amplitude modulation* and *frequency modulation* methods respectively. NC-AFM operates in the attractive force regime (see Fig.1.8) and never comes into contact with the sample, rendering it a "non-destructive" technique. Frequency modulated (FM) NC-AFM (developed by Albrecht *et al* in 1991 [35]) is the imaging mode used throughout this thesis.

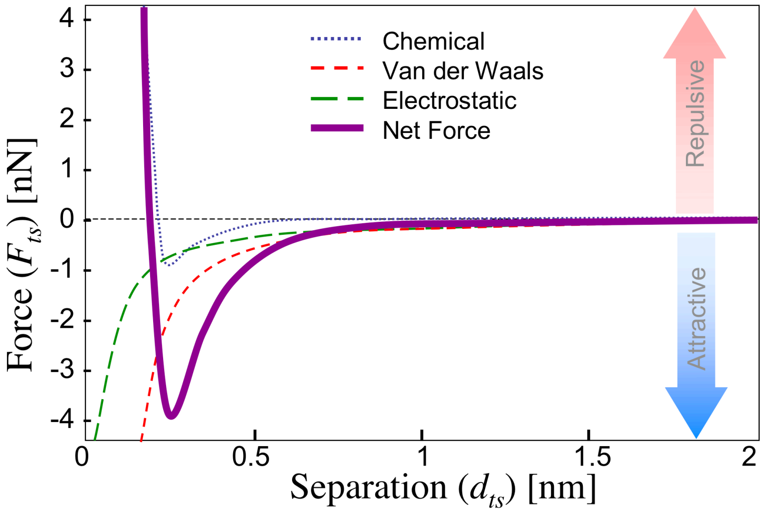

Figure 1.8: A typical "force-distance" curve used to explain typical NC-AFM imaging conditions

NC-AFM

The FM NC-AFM feedback loop used herein is illustrated in Fig.1.9. The cantilever is oscillated with a sinusoidal drive signal on the excitation piezoelectric element (sometimes called the shaker piezo). The laser deflection photodiode detects the cantilever oscillation signal, which is sent to a phase locked loop (PLL) amplitude controller box (which also contains an automatic gain controller (AGC) used to maintain a set oscillation amplitude) that modulates the drive signal sent to the shaker piezo. During FM NC-AFM imaging, the cantilever is oscillated on or near resonance, which shifts as a function of interaction force with the sample (explained below). The feedback maintains a constant frequency shift (relative to the "free" or non-interacting cantilever resonance) which corresponds to a constant tip-sample interaction during imaging (constant force mode) by compensating the tip-sample separation (tip height, z) with the xyz-piezo tube.

NC-AFM can be used in vacuum (typically with FM) and fluid (such as air

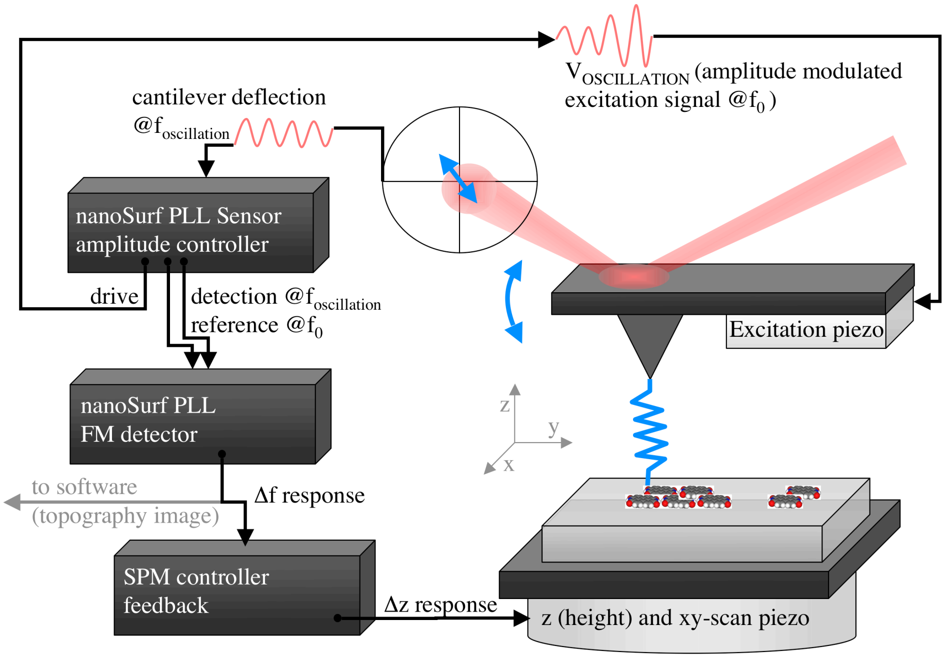

Figure 1.9: Feedback loop for force gradient mode frequency modulated NC-AFM. Details of the nanoSurf components can be found in Appendix E

and water, typically with AM) environments. It can detect a variety of forces, including long range electrostatics, Van der Waals and magnetic (requires a magnetic tip) forces, as well as short range chemical, mechanical contact, indentation, friction, and capillary forces. The force on the cantilever depends on the tip-sample potential energy V_{ts}:

$$F_{ts} = -\frac{\partial V_{ts}}{\partial z}. \tag{1.1}$$

Experiments take place under ultra high vacuum (UHV) conditions with highly doped silicon cantilevers (with an aluminum coating to increase laser reflection). A typical curve illustrates the expected electrostatic, Van der Waals and chemical force contributions as a function of tip-sample separation in Fig.1.8. The long range electrostatic and Van der Walls contributions are always attractive and typically approximately calculated assuming sphere-and-plane geometry [36]. The electrostatic contribution to the tip-sample potential is the electric potential difference (voltage) between them, V_{es}. The Van der Waals component, V_{VdW}, is calculated by:

$$V_{VdW} = \frac{A_H R}{6z}, \tag{1.2}$$

where A_H is the Hamaker constant (a material parameter depending on density and particle-particle interaction), *R* is the spherical tip radius, and *z* is the perpendicular distance between the centre of the nearest tip atom and the plane of the centres of the flat surface atoms. The short range chemical contributions have an attractive minimum at the equilibrium bonding distance and then become strongly repulsive at closer approaches. Chemical forces are usually described by Morse or Lennard-Jones potentials:

$$V_{Morse} = -E_{bond}[2e^{\kappa(z-z_0)} - e^{-2\kappa(z-z_0)}], \tag{1.3}$$

or

$$V_{L-J} = -E_{bond}[2\frac{z^6}{{z_0}^6} - \frac{z^{12}}{{z_0}^{12}}], \tag{1.4}$$

where E_{bond} is the chemical bonding energy (or potential well depth), κ is a decay length (or width of the well), and z_0 is the equilibrium distance between atoms.

The *cantilever spring constant*, *k*, is calculated as [36]:

$$k = \frac{E_Y w t^3}{4L^3}, \tag{1.5}$$

for a rectangular cantilever with dimensions width, *w*, thickness, *t*, and length, *L* where E_Y is the Young's modulus (the ration of tensile stress to strain, usually given as a material constant and assumes isotropy). The *resonance frequency*, f_0 of a harmonic oscillator (acting as a Hooke's Law spring where F = -kx and x is the mass displacement from equilibrium) is given by:

$$f_0 = \frac{1}{2\pi}\sqrt{\frac{k}{m}}, \tag{1.6}$$

where m is the effective mass of the oscillator. For a rectangular cantilever, this is approximated by:

$$f_0 = 0.162\frac{t}{L^2}\sqrt{\frac{Y}{\rho}}, \tag{1.7}$$

where ρ is the cantilever density [37]. These equations are based on Euler-Bernoulli beam theory and are approximations that only apply to the first harmonic (normal) mode of the cantilever moving in the plane intersecting the cantilever axis (pitch, not roll or yaw). They assume perfect clamping at the fixed (chip) end of the cantilever. However, the AFM tip is not typically located at the very end of the beam, and therefore the effective spring constant is increased. This is frequently neglected and illustrated incorrectly, and it is worth noting that the lever arm only extends to the loading point (the tip) along the cantilever axis (a person standing in the middle of a diving board does not dip as far as if they were to stand at the end - the spring constant is higher closer to the clamped end). Internal damping, imperfect clamping and beam geometry are all factors that influence real world cantilever dynamics such that it is difficult to accurately calculate. More complete models provide better approximations of cantilever motion by incorporating internal damping and a complex elastic modulus, such as the generalized model of Rast *et al* [38].

In dynamic imaging modes (tapping or non-contact), attractive interactions

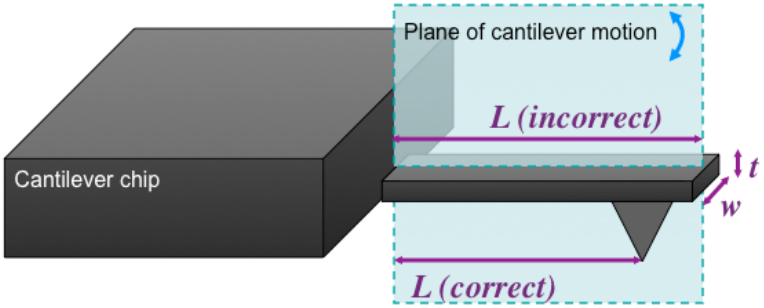

Figure 1.10: Correct and incorrect lever arm length, *L*, for spring constant, *k*, calculation of a rectangular cantilever

serve to decrease the cantilever resonance frequency (by acting opposite to the restoring force and decreasing the effective *k*) and repulsive forces increase it (by acting with the restoring force and increasing the effective *k*). The drive signal sent to the cantilever shaker piezo is maintained at a 90° phase shift relative to the measured cantilever oscillation in order to minimize the drive signal amplitude required (and energy dissipated). The frequency shift, Δf, has a settling time, $\tau \approx 1/f_0$, and depends on the sum of interaction forces acting on the cantilever as it sweeps up and down (in $\hat{z}$) near the surface (Fig.1.8) [36]:

$$\Delta f = -\frac{f_0}{2kA\pi}\int_0^{2\pi} F_{ts}(z_0 + A\cos\theta)\cos\theta d\theta, \qquad (1.8)$$

where A is the oscillation amplitude, F_{ts} is the tip-sample interaction force, z_0 the cantilever equilibrium position, θ is the phase angle and we integrate over one full oscillation. Sufficiently large amplitudes must be used during imaging to prevent “snap-to-contact”, which may occur if the tip-sample force gradient exceeds the cantilever spring constant (or equivalently, if the tip-sample force exceeds the cantilever restoring force $F = -kA$) [33, 36]. To avoid confusion in feedback about the non-monotonic section of the force-distance curve, imaging frequency shift setpoints are typically chosen on the right hand side of the force minimum, such that an increase in frequency shift corresponds to an increase in force and a decrease in tip-sample separation. If the slope of the force-distance curve (force gradient) is constant over the oscillation range, the frequency shift is approximated simply by [36] :

$$\Delta f = -\frac{f_0}{2k}\frac{\partial F_{ts}}{\partial z}. \tag{1.9}$$

However, the force gradient varies significantly over the large oscillation amplitudes typically used to prevent snap-to-contact (5-7 nm herein), so one must integrate over the range of force gradients to approximate the resulting frequency shift [36] :

$$\Delta f = -\frac{f_0}{2k}\int_{-a}^{a}\frac{\partial F_{ts}(z-q)}{\partial z}\frac{\sqrt{A^2-q^2}}{\pi A^2/2}dq, \tag{1.10}$$

where q is the instantaneous cantilever deflection.

Fortunately, a lovely approximation known as the *normalized frequency shift*, Γ, can be used to compare tip-sample interactions when oscillation amplitudes are large compared to the force gradient region [39]:

$$\Gamma = \frac{kA^{3/2}}{f_0}\Delta f. \tag{1.11}$$

This is a convenient way to compare interaction strength for cantilevers with different resonant frequencies and spring constants. The normalized frequency shift approaches a constant value at large amplitudes, and can therefore also be used to calibrate oscillation amplitude. This is done by sweeping the cantilever drive signal amplitude, monitoring the change in height, Δz, required to keep frequency shift constant, and solving for A [36]. It is worth noting that the net force applied between the tip and sample is not the only important factor when considering tip-sample interaction. The localized interaction depends not only on the tip-sample contact area but also on the deformation and shape of the tip (certainly it is more painful to have ones foot stepped on by a stiletto heel than a flat shoe, even though the weight of the stepper does not change and the total force applied is constant). Pressure (force/area) may be a more useful indication of tip-sample interaction, but in practice is difficult to calculate given the unknown nanoscale features of the bodies involved, and therefore we make do with normalized frequency shifts.

By sweeping the drive signal frequency (while maintaining a constant drive amplitude), cantilever oscillation spectra can be mapped (as illustrated in Fig.1.11). The quality factor (or Q-factor), Q, of a resonator relates its resonance frequency to the rate at which it dissipates energy during oscillation (damping). It is calculated by comparing the resonant frequency, f_0, with the width of the peak at half of the maximum total energy value (Δf, the full width at half max, FWHM, also known as the bandwidth). We measure the oscillation amplitude rather than energy (the total energy is the sum of potential and kinetic energy). The potential energy stored in the cantilever is calculated as:

$$E_p = \frac{1}{2}k(z - z_0)^2, \tag{1.12}$$

and all energy is stored as potential at the maximum amplitude (where velocity and kinetic energy are zero). Therefore the width of our resonance peak, Δf, is measured at the maximum amplitude divided by $\sqrt{2}$ (the full width at root half max, FWRHM), corresponding to half of the maximum total energy. The use of high Q cantilevers increases the force gradient sensitivity (inversely proportional to $\sqrt{Q}$) [35], with typical sensitivities on the order of 1 pm$\sqrt{Hz}$ [36] under vacuum.

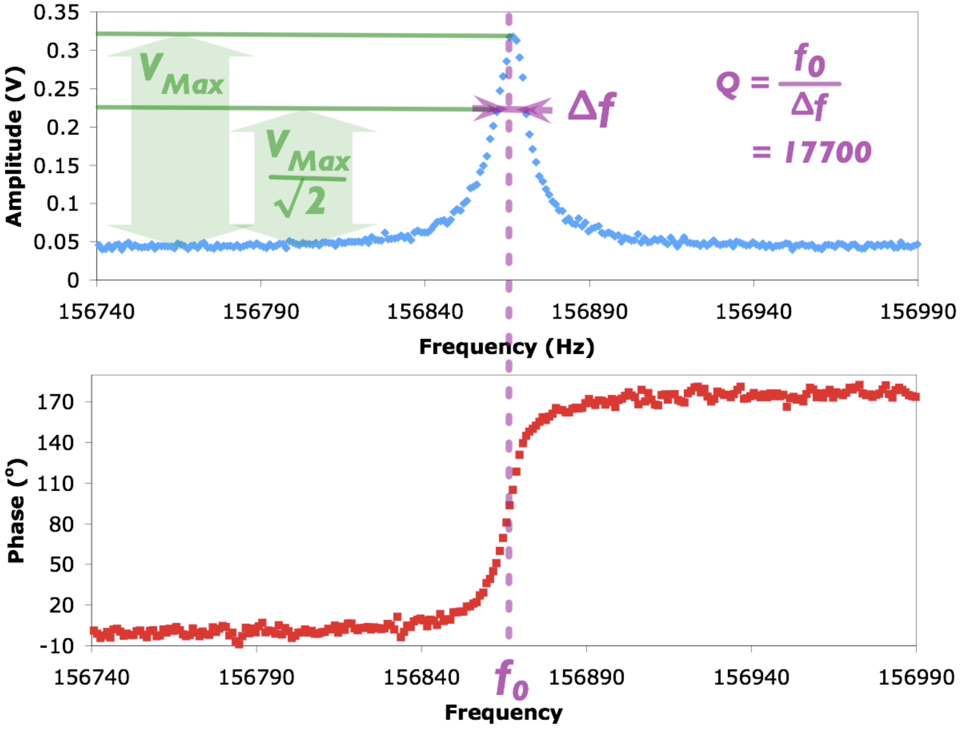

Figure 1.11: Frequency spectrum amplitude and phase resonant response for a better than typical PPP-NCLR cantilever (typical Q ~10000) in UHV, with the accompanying Q-factor calculation

KPFM

Kelvin Probe Force Microscopy (KPFM) is an AFM technique introduced by Nonnenmacher in 1991 [40], which is a scanning probe version of the Kelvin Probe technique developed in 1932 by Zisman [41], based on the Kelvin Method of measuring the electrostatic force between dissimilar metals invented by Lord Kelvin in 1861 [42].

The generalized principal of KPFM is illustrated in Fig.1.12. When the AFM tip is brought close to the surface, the Fermi energies match and charge flows between the two materials (due to space charge continuity). The resulting offset in charge produces an electric field between the tip and sample, accompanied by an attractive electrostatic force. This force can be negated by applying a voltage between the tip and sample equal to the difference in Fermi energies (and work functions) to shift the band-offset back to the original uncharged case. This is generally accomplished with a conductive tip on a conductive sample, and the applied voltage is said to equal the *contact potential difference (CPD)*,

$$V_{CPD} = \frac{\phi_t - \phi_s}{e}, \tag{1.13}$$

where ϕ_t and ϕ_s are the tip and sample work functions and e is the electron charge. The tip-sample electrostatic force varies parabolically as a function of voltage about this value,

$$F_{es} = -\frac{1}{2}\frac{dC(z)}{dz}\Delta V^2, \tag{1.14}$$

where $dC(z)/dz$ is the (geometry and material dependent) tip-sample capacitance gradient ΔV and is the difference between V_{CPD} and the applied tip-sample bias, so the zero-force value is also called the *contact potential minimum* [43]. The electrostatic force may be approximated for a conducting spherical tip and planar sample according to:

$$F_{es} = -\frac{\pi\epsilon_0 R \Delta V^2}{z}, \tag{1.15}$$

where ϵ_0 is the permittivity of free space and R is the tip radius [36].

KPFM may be performed simultaneously during NC-AFM imaging to map the surface local contact potential difference (LCPD, the physical interpretation of

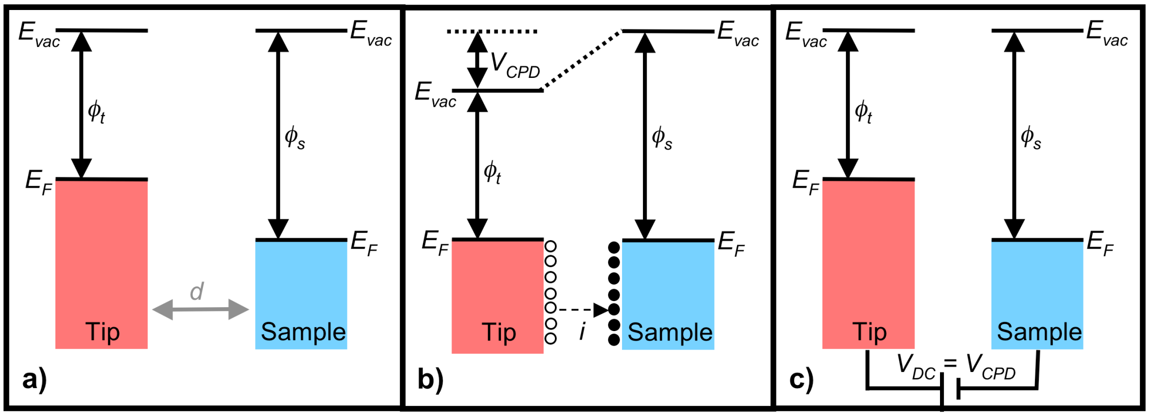

Figure 1.12: The standard picture of KPFM operation (after [43]): (a) tip and sample are separated by a large distance and are not in electrical contact. (b) tip and sample make electrical contact and charge flows to match Fermi energies, resulting in an attractive force. (c) Tip and sample are in electrical contact, with tip-sample bias applied to shift bands back to original offset, $V_{DC} = V_{CPD}$, at which point charge offset and force disappear.

values measured are still a subject of some debate, given that the ignored surface and interface states that may prove important for a sharp tip). *Frequency modulated (FM) KPFM* is accomplished by applying an oscillating bias, V_{AC}, at a modulation frequency, ω, with a DC offset, V_{DC}, to the tip and using a lock-in amplifier to track the frequency shift response [44] (amplitude modulation has recently been shown to suffer from lateral averaging and significant lift-height dependence [45, 46]). An additional feedback loop (shown in Fig.1.13) is used to determine and set the DC offset to the value that minimizes the frequency shift component at the Kelvin modulation frequency, as illustrated in Fig. 1.14. The difference between V_{CPD} and the applied tip-sample bias is now given by:

$$\Delta V = V_{CPD} - V_{ts} = V_{CPD} - (V_{DC} + V_{AC} sin(\omega t)). \tag{1.16}$$

The electrostatic force becomes:

$$F_{es} = -\frac{1}{2}(V_{CPD} - (V_{DC} + V_{AC}sin(\omega t)))^2 \frac{dC(z)}{dz}, \tag{1.17}$$

which may be expanded (using the double angle formula $cos(2\theta) = 1 - 2sin^2(\theta)$) and divided into three parts:

$$F_{es} = F_{DC} + F_\omega + F_{2\omega} \tag{1.18}$$

1. A *DC* term that produces static cantilever deflection,

$$F_{DC} = \frac{1}{2}\frac{dC(z)}{dz}((V_{CPD} - V_{DC})^2 + \frac{1}{2}{V_{AC}}^2) \tag{1.19}$$

2. An *AC* term that oscillates the cantilever at the Kelvin modulation frequency ω,

$$F_\omega = -\frac{dC(z)}{dz}(V_{CPD} - V_{DC})V_{AC}sin(\omega t) \tag{1.20}$$

3. A second *AC* term that oscillates at twice the modulation frequency,

$$F_{2\omega} = -\frac{1}{4}\frac{dC(z)}{dz}{V_{AC}}^2 cos(2\omega t) \tag{1.21}$$

The corresponding frequency shift measured by FM NC-AFM can be found by taking a derivative with respect to *z* (equation 1.8 above), and also divided into the three components potentially used for feedback:

1. The *DC* frequency shift term,

$$\Delta f_{DC} \propto \frac{dF_{DC}}{dz} = \frac{1}{2}\frac{d^2C(z)}{dz^2}((V_{CPD} - V_{DC})^2 + \frac{1}{2}{V_{AC}}^2) \tag{1.22}$$

2. The *AC* frequency shift term that oscillates at the Kelvin modulation frequency ω and is used in FM KPFM to measure V_{CPD},

$$\Delta f_{\omega} \propto \frac{dF_{\omega}}{dz} = -\frac{d^2C(z)}{dz^2}(V_{CPD} - V_{DC})V_{AC}sin(\omega t) \tag{1.23}$$

3. The *AC* frequency shift term that oscillates at twice the Kelvin modulation frequency 2ω and can be used for capacitance microscopy,

$$\Delta f_{2\omega} \propto \frac{dF_{2\omega}}{dz} = -\frac{1}{4}\frac{d^2C(z)}{dz^2}V_{AC}^2 cos(2\omega t). \tag{1.24}$$

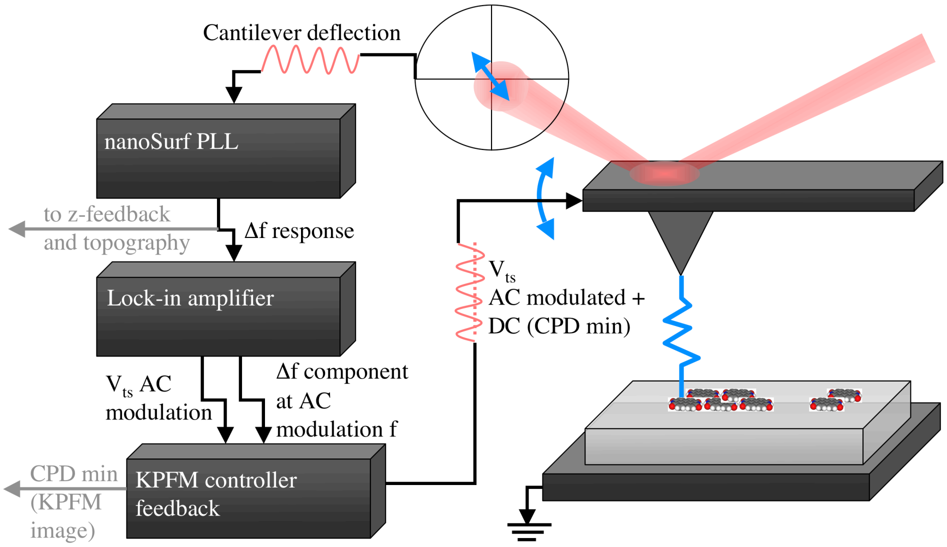

Figure 1.13: Feedback loop for force gradient mode FM-KPFM. Details of the nanoSurf components can be found in Appendix E

In our setup, highly doped silicon tips covered in native oxide and bulk insulating samples are used with the voltage applied between the tip and sample holder, illustrated in Fig.1.15. Electric field enhancement occurs at the tip that depends on the tip apex geometry (that might best be approximated by finite element analysis [47,48]), and the sample holder geometry is shown in Fig.1.19. The band structure and resulting LCPD measured across such a multi-material setup becomes difficult to interpret. Conductivities range from high in the metal back gate and degenerately doped silicon (which essentially acts as a metal), to moderate in semiconducting layers, to low in the bulk insulator and vacuum layers, and influence where the voltage drops take place. Each interface contains possible surface states, charges and defects which may contribute to electric field screening. It is probable that the electrostatic force is not compensated to zero everywhere between the biased tip and sample holder during KPFM, but the use of force gradients allows us to find the surface contact potential minimum by negating the *local* electric field between the tip apex and sample surface (elaborated on below). The interpretation of the LCPD values measured is difficult, so this technique is qualitative rather than quantitative, but still allows for useful characterization and comparison of sample surface properties. Sadewasser *et al.* proposed that KPFM also allows the measurement of “true height” by NC-AFM, which might otherwise be offset by electrostatics [49].

As discussed above, the frequency shift detected by FM NC-AFM is due to a force gradient. The modulated component of the force gradient detected in KPFM is electrostatic, caused by an electric field between the tip apex and sample, produced by an electric charge offset between them. It is not obvious how spatially localized the charge offset is (depends on tip and sample charge carrier mobilities and densities, just like the space-charge/band-bending/depletion region of a pn-junction). Charge carrier mobilities are rather low in bulk insulators such as KBr and NaCl (on the order of 100 cm^2/Vs for electrons and near zero for holes due to “self-trapping” polarons according to the Jahn-Teller effect: Asymmetric local lattice distortion occurs more prevalently when band edges are degenerate, and the valence band is more often degenerate than conduction band. This results in self-trapped holes for all alkali and silver halides [50]). Ionic solids tend to have low conductivities, less than 10^{-6} $(\Omega cm)^{-1}$ at room temperature, whereas metals generally have high conductivity, on the order of 10^{5} $(\Omega cm)^{-1}$, and large numbers of conduction electrons [50]. Silicon has typical room temperature mobility values of 1350 cm^2/Vs for electrons and 480 cm^2/Vs for holes [50,51], and an intermediate conductivity of about $1(\Omega cm)^{-1}$ when doped to an electron concentration, N_d of 10^{15} $(cm)^{-3}$ [51]. In our setup, instead of applying a bias directly to a conducting tip and sample to shift the band offset, we apply a voltage across the bulk cantilever and back electrode. In doing so, we may create an electric field between them across the entire multi-junction that negates the local tip-sample force gradient and minimizes the corresponding "CPD". In summary, *gradients are key* in allowing us to qualitatively measure local surface properties even with this strange multi-material biasing geometry.

In dealing with nanoscopic volumes that may be more akin to surface states than bulk materials, it is also not obvious whether or not tunnelling occurs across the vacuum gap during NC-AFM imaging between the tip and sample to match the Fermi energies (some controversy lies here). Not all AFM tips produce detectable KFPM imaging contrast, and imaging quality varies from tip to tip. The dominant influence of the tip apex has been discussed by Barth *et al.* and supported with theoretical modeling [52]. However, for many tip-sample combinations, there exists a sufficient tip-sample charge offset and corresponding force gradient to successfully characterize the surface with KPFM.

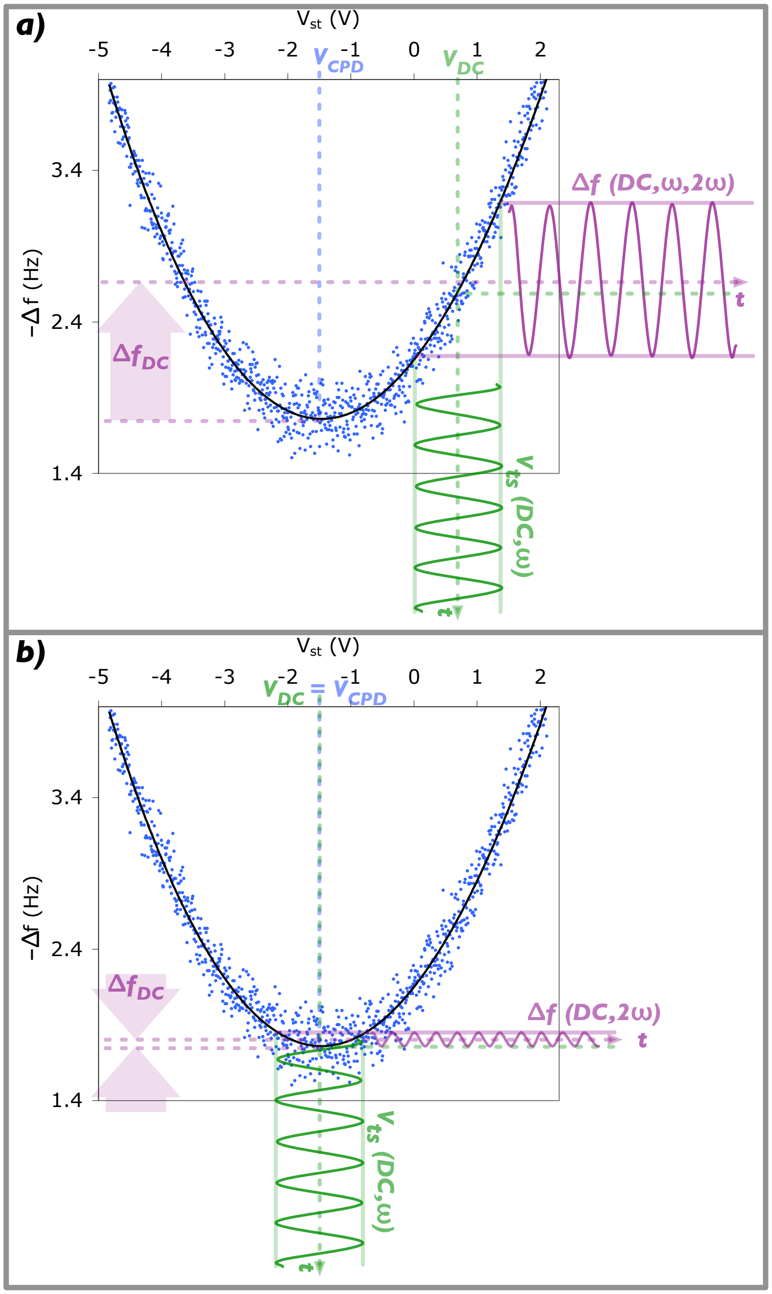

Figure 1.14: A typical static frequency shift - voltage spectrum, Δf versus V_{st} illustrating the parabolic CPD "minimum" ("st" indicates that here the high bias is applied to the sample instead of the tip) recorded at a point over an island of CuPc on NaCl. Corresponding KPFM signals (tip-sample voltage in green, frequency shift response in purple) are given for two cases: (a) a 1 V_{rms} oscillating bias with 0.7 V DC-offset is applied between tip and sample (b) the KPFM feedback has successfully set $V_{DC} = V_{CPD}$ by minimizing the frequency shift Δf modulated at Kelvin modulation frequency ω

.

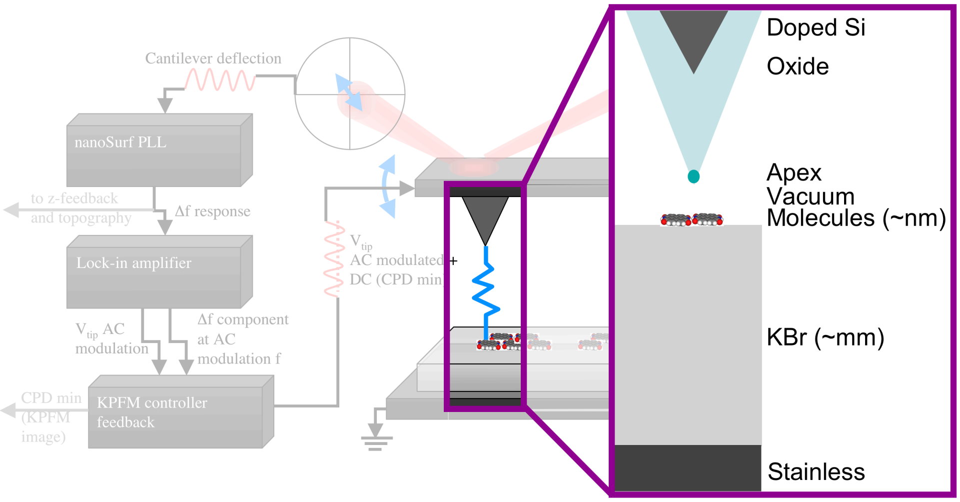

Figure 1.15: Kelvin probe bias voltage applied across a multi-material geometry

1.3 Experiment

1.3.1 Molecules

3,4,9,10-Perylenetetracarboxylic diimide (PTCDI) is an organic semiconductor with interesting electronic and optical properties [6–14] (discussed further in Chapter 4). Copper phthalocyanine (CuPc) is also semiconducting and widely used as an absorber in photovoltaic applications due to its photovoltaic and photoconductivity characteristics and a hole injection material in OLEDs [49, 53–60]. Both (illustrated in Fig.1.16) are candidate molecules for molecular electronics [4, 5].

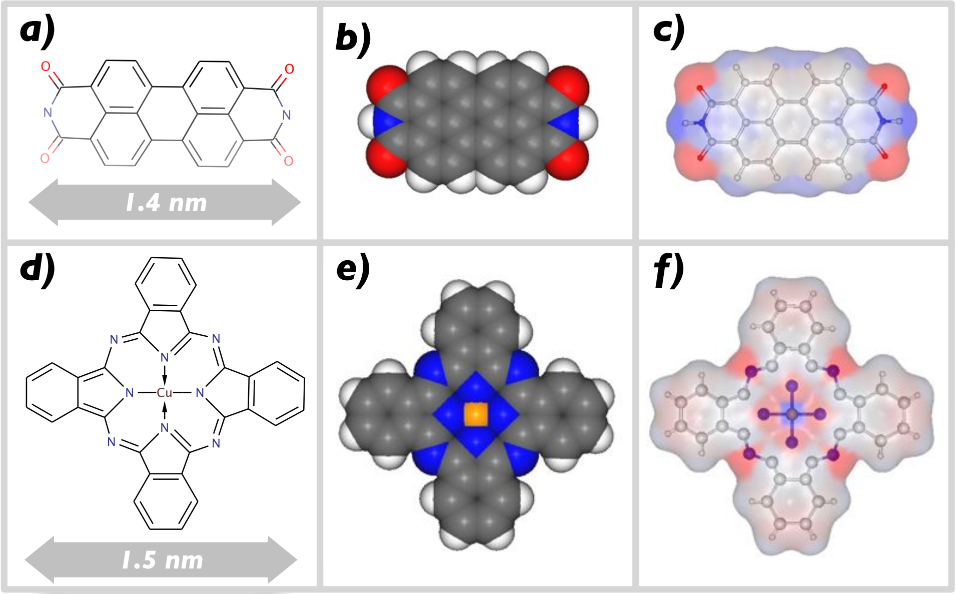

Figure 1.16: PTCDI and CuPc molecules (a and d) structure, (b and e) space fill and (c and f) Van der Waals surface with wireframe overlay (all rendered using Marvin by ChemAxon).

1.3.2 Substrates

Insulating substrates such as alkali halides provide the ability to electrically isolate deposited structures [61] from the underlying surfaces, facilitating characterization of their electronic properties and prevent leakage currents that might otherwise hamper device characterization. NaCl and KBr have large band gaps of ∼8.5 eV and ∼7.4 eV respectively [62, 63], and can easily provide large, clean, atomically flat terraces because they cleave preferentially along the $\{100\}$ planes, an example shown in Fig.1.17. Both have the same "rock salt" crystal structure and "checkerboard" surface with lattice constants of 0.565 nm for NaCl and 0.660 nm for KBr. Cleaving takes place under UHV to avoid contamination. Interactions with these substrates influence the growth of deposited PTCDI [6]; the negative oxygen atoms are generally expected to sit over the alkali-halide substrate cations [13, 16, 64].

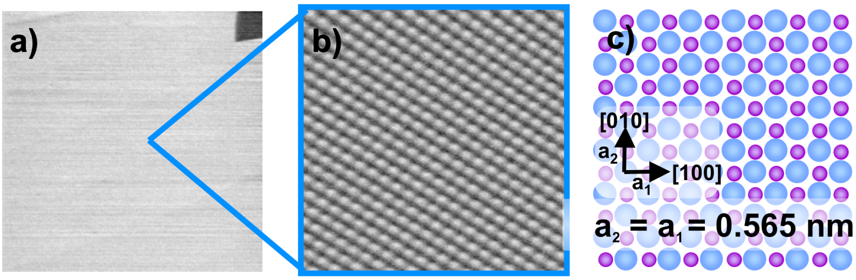

Figure 1.17: Cleaved NaCl surface, (a) 1 μm x 1 μm NC-AFM image of an atomically flat terrace with a single atom-deep step in the top corner, (b) 7 nm x 7 nm NC-AFM image with atomic contrast on one ionic species, (c) illustration of "checkerboard" lattice structure.

1.3.3 Instrument

The surface science of molecule-on-insulator systems has not yet been thoroughly studied, in part due to the obstacles in performing scanning tunnelling microscopy (STM) on such samples. Non-contact atomic force microscopy (NC-AFM) is a non-destructive, high resolution technique ideal for imaging bulk insulator surfaces [35, 36]. NC-AFM has been successfully used to image several systems of molecules deposited on insulators [65–67]. The primary instrument used for all experiments herein is the commercial JEOL JSPM 4500A UVH AFM/STM/SEM system. It is an ultra high vacuum (UHV) system and consists of two primary chambers: the preparation chamber and the measurement chamber, (Fig.1.18). The image resolution, noise, sensitivity, drift and stability have been thoroughly characterized by a previous student [68] and will not be repeated here. The UHV environment (with typical pressure on the order of 1×10^{-8} Pa) is achieved by baking the system to $\sim$150°C during the initial pump down with a turbomolecular pump (Pfeiffer TMU 261, backed by a roughing pump), and maintained with ion pumps and titanium sublimation pumps in each chamber. Samples enter the system through the fast loadlock and remain under UHV for the duration of the experiment.

Preparation Chamber

The preparation chamber is used to prepare clean alkali-halide substrates and to deposit molecules, metals and pits. It features a cleaving station, a three-crucible thermal molecule evaporator (Kentax TCE-BSC), a four-pocket electron-beam evaporator (Oxford Applied Research), and a quartz crystal deposition monitor (Inficon). It also contains a low energy electron diffractometer (LEED) and

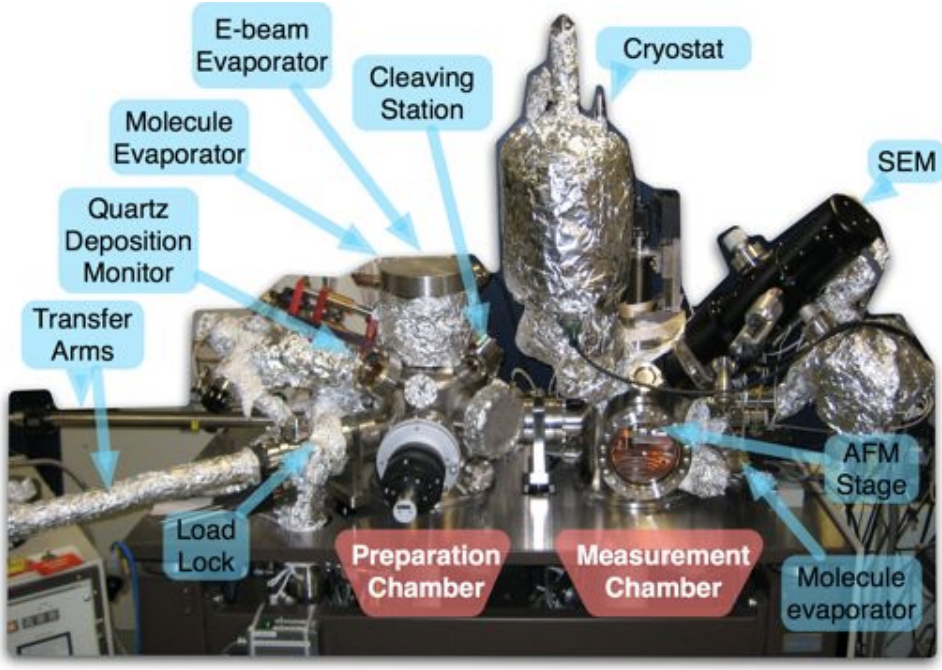

Figure 1.18: The JEOL JSPM 4500A UHV system

Auger spectrometer, as well as an ion sputtering gun, which are not generally used on alkali-halide samples due to charging effects.

Typical sample preparation is as follows: single crystal NaCl or KBr (Korth Kristalle, Germany) samples are cleaved *in situ* (sample holder shown in Fig.1.19), and heated to ∼150°C for approximately one hour in a parent holder that contains a tungsten filament. The molecule evaporator is used to thermally deposit molecules, generally onto room temperature substrates. PTCDI (Alfa Aesar, 98% purity) evaporates at approximately 300°C, and CuPc at approximately 350°C, having first been outgassed at 200°C overnight. Pits are created by irradiating the surface with charge using the electron beam evaporator below the evaporation threshold, at a sample temperature of ∼250°C with typical charge doses of $1.2 \pm 0.1\ \mu\mathrm{C/cm^2}$ [46, 67]. Gold is also deposited using the electron-beam evaporator.

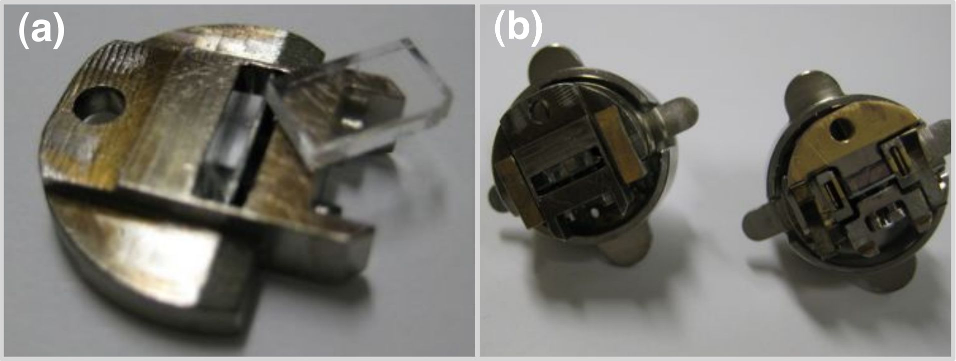

Figure 1.19: (a) Cleaved KBr crystal in JEOL sample holder, (b) two examples of crystal sample holders placed in parent holders used to transfer sample position

Deposition rates are calibrated using the quartz crystal deposition monitor (assuming densities of 1.7 g/cm^3 for PTCDI, 1.62 g/cm^3 for CuPc, and 19.3 g/cm^3 for gold). Typical molecule deposition rates range from 48 to 96 pm/min, and gold from 7 to 15 pm/min. Prepared samples are subsequently passed via transfer arm into the measurement chamber for characterization.

Measurement Chamber

The measurement chamber features a scanning probe setup that may be configured for either scanning tunnelling microscopy (STM) or atomic force microscopy (AFM); the latter used here. Beam deflection is used for cantilever oscillation detection, shown with the imaging stage in Fig.1.20. It also contains a scanning electron microscope (SEM) column and detector, a cryostat for sample cooling with liquid nitrogen or helium (to temperatures of approximately 80 K or 30 K respectively), a single-crucible molecule evaporator (modified Kurt J. Lesker, described in Appendix B) and windowed optical access (see also Appendix D). Samples in the imaging stage may be illuminated during characterization, as pictured in Fig.1.21

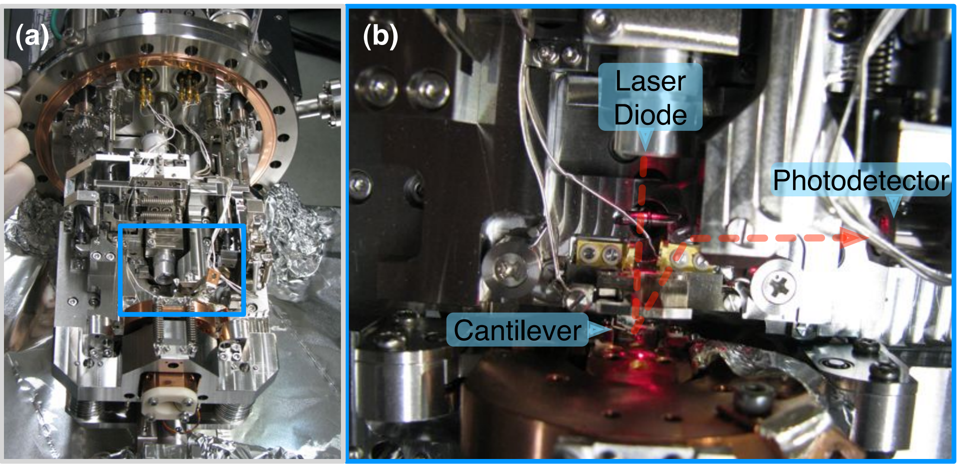

Figure 1.20: (a) sample imaging stage (b) close-up of blue rectangle area with simplified laser deflection path indicated

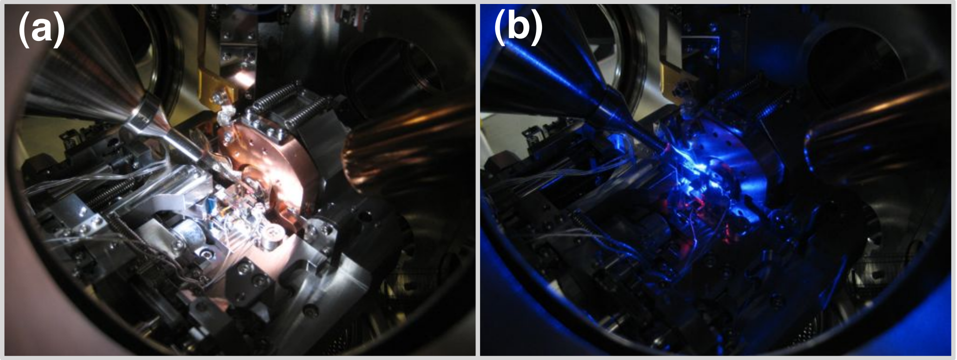

Figure 1.21: Sample in imaging stage illuminated with (a) white LED light and (b) blue laser light (473 nm 50mW max Melles Griot)

Typical sample characterization is as follows: samples are imaged by NC-AFM using a modified nanoSurf easyPLL with distance control for constant frequency shift topography mode. Nanosensors cantilevers (PPP-NCLR) with typical resonance frequencies of 160-170 kHz, spring constants of ∼40 N/m, and oscillation amplitudes of 6-7nm are used (cantilever holder shown in Fig.1.22). KPFM is done by applying an oscillating bias with a DC-offset to the cantilever using a lock-in amplifier (Princeton Applied Research 5110) with DC values from -10 to 10 v, modulation frequencies of 800-1000 Hz, and oscillation amplitudes of 0.7-1.2 V_{rms}. AFM image sizes generally range from 5 nm to 2 μm. For all microscopy images presented in this thesis, the fast raster scan direction is approximately along the alkali halide [100] direction and the slow scan direction is approximately along the [0$\bar{1}$0] direction (typically with a slight rotation of 5-10° counterclockwise, caused by sample positioning, as shown in Fig.1.17) and Fig.1.19). The SEM is used to collect larger scale images on the order of μm to cm, and may be used to precisely position cantilevers over samples, as illustrated in Fig.1.23 The SEM, similar to LEED and Auger, is not typically used on alkali-halides for more than brief periods of time and at low magnifications to minimize the creation of undesired sample pits and charging.

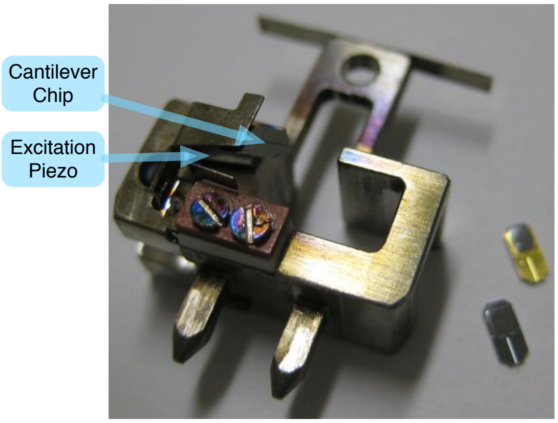

Figure 1.22: Cantilever in JEOL AFM cantilever holder, held in place and electrically contacted by top spring clip and excited by white piezoelectric element. Ordinary and gold coated cantilever chips shown beside holder

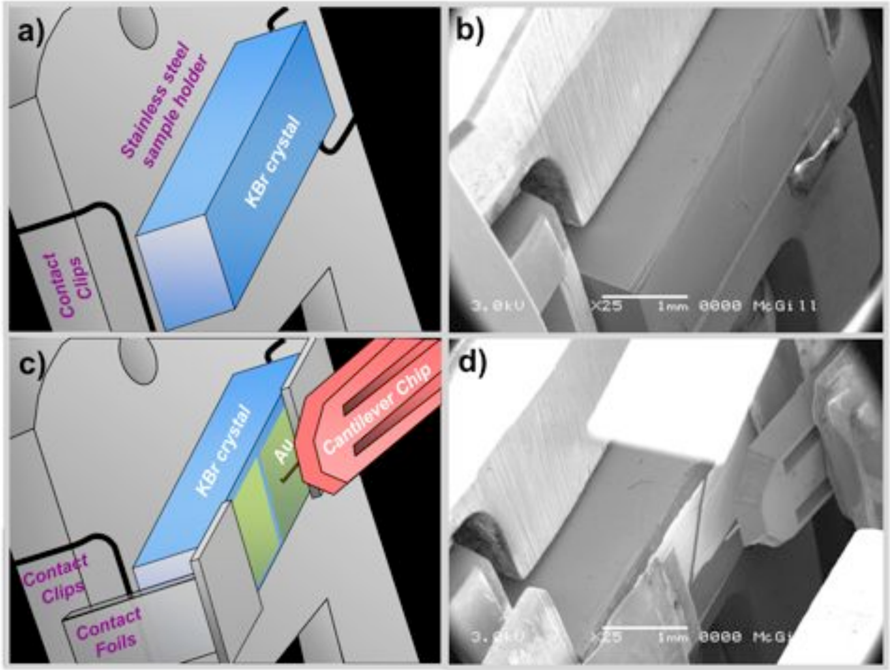

Figure 1.23: Use of the SEM to precisely position cantilever over sample: (a) labeled illustration of sample holder containing cleaved KBr sample as imaged by SEM in (b), (c) labeled illustration of KBr sample prepared with deposited Au contact pads and contact clips attached, using SEM to position the tip in the gap sample as shown in (d)

2

Molecular Dewetting

THIS CHAPTER IS BASED ON:

J.M. Topple, S.A. Burke, S. Fostner and P. Grutter, *Thin film evolution: Dewetting dynamics of a bimodal molecular system*. Phys. Rev. B, 79(20), 205414, (2009)

2.1 Growth

Bimodal growth systems exhibiting dewetting between two-dimensional (2D) and three-dimensional (3D) morphologies have been observed previously [16, 69–73]. The dewetting scenario is consistent for all bimodal and multimodal systems: atoms or molecules must overcome a potential energy barrier to reach the most stable state (the minimal free energy), and are limited by kinetic factors such as temperature and physical barriers (steps). This type of process, in general, is akin to other coarsening scenarios such as Ostwald ripening in that the growth process is competitive. Stable islands grow at the expense of metastable islands through mass transport driven by the minimization of the global free energy.

The analysis which applies to atomistic processes [24–26] of this nature can also be applied to describe the dynamics of molecular dewetting. Thurmer *et al.* [70] concluded that the transitional morphologies observed for Ag on Si(111) were influenced by substrate step density, annealing time, and temperature. These atomic systems are in many ways analogous to the molecular case. Bimodal growth has also been observed for molecular systems [16, 73] but the dynamics of the dewetting transition have thus far not been characterized. Kowarik *et al.* concluded that organic materials have 3 additional issues which may alter growth behaviour and epitaxy as compared to that for inorganic materials [74]:

1. Internal degrees of freedom (vibrational, conformational and orientational)
2. Molecule-molecule and molecule-substrate weak van der Waals force interactions
3. Interaction potentials with surroundings spread over a large area.

3,4,9,10-Perylenetetracarboxylic diimide (PTCDI) is an organic semiconductor with interesting electronic and optical properties [6–14], similar to the well studied 3,4,9,10-perylenetetracarboxylic dianhydride (PTCDA) [75, 76]. The crystalline structures of both molecules are influenced by hydrogen bonding between molecules; PTCDA anhydride groups tend to form hydrogen bonds to the perylene core edges while PTCDI N-H groups form hydrogen bonds to oxygen atoms of neighboring molecules [12], leading to the formation of different crystalline structures for the two very similar molecules.

The substrate also influences the growth of both PTCDA and PTCDI [6], and in the case of alkali halides the negative oxygen atoms are expected to sit over the substrate cations [13, 16, 64]. Insulating substrates are an advantageous choice on which to build “proof of concept” molecular electronic devices, providing the ability to electrically isolate the device from the underlying surface [61]. However, the surface science of molecules on insulators is not well understood, and therefore we attempt to obtain a more complete understanding of interactions between organic molecules and insulating substrates with NC-AFM.

The bimodal growth of PTCDI on NaCl is an interesting case in that one may observe in detail the dewetting transition over the course of days at room temperature. Other multimodal systems generally either dewet on much faster or slower time scales. Systems such as C_{60} on NaCl [66] show evidence of dewetting but evolve too quickly to observe metastable structures at room temperature. Many other systems must be annealed to provide the additional energy to observe dewetting on a reasonable time scale [16, 69–73].

2.2 Experimental Procedures

Preparation and characterization of samples took place in the JEOL JSPM 4500A UHV AFM system. Single crystal NaCl samples were cleaved *in situ* and heated to ∼150°C for 1 h. PTCDI molecules (Alfa Aesar, 98% purity) were thermally deposited at 300°C onto room temperature substrates, having first been outgassed at 200°C overnight. Deposition rates were calibrated using a quartz crystal microbalance and ranged from 0.008 to 0.015 Å/s. Samples were subsequently imaged by NC-AFM. Nanosensors cantilevers (PPP-NCLR) with typical resonance frequencies of 160-170 kHz, spring constants of ∼40 N/m, and oscillation amplitudes of 6-7 nm were used.

2.3 Epitaxy

Images taken within a few hours of deposition reveal two coexisting morphologies: needle shaped islands comprised of multiple layers of PTCDI with edges at an angle of 16 ± 1° relative to the NaCl <110> directions, and square shaped, 1-2 layer islands aligned with the <100>, shown in Fig.2.4. The two shapes are associated with different epitaxies (discussed further below). Images with molecular resolution of the PTCDI and atomic resolution of the underlying NaCl were used to determine the structure of each island type, illustrated in Fig.2.1.

2.3.1 Square Islands

The square shaped islands are usually comprised of a single layer of PTCDI, with individual molecules oriented along the NaCl <011> directions (two possible orientations). Based on the image in Fig.2.1a, we propose a (2×2) brick wall structure with each molecule in equivalent position with respect to the substrate, illustrated in Fig.2.1c. A stable second layer occasionally forms provided the island area is large enough ($\gtrsim$ 400 nm^2), but is often observed to be transient. Molecules in square islands are highly mobile and therefore difficult to image. This indicates that they are less energetically favorable than needle islands, which sustain imaging frequency shifts on the order of -20 Hz (normalized frequency shift of -3 fN$\sqrt{m}$) without alteration.

2.3.2 Needle Islands

Needle shaped islands have been observed exclusively with heights of two or more layers. The nucleation of 3 needle islands beginning with bilayers was captured in a sequence of NC-AFM images (see Appendix A), demonstrating a minimum of two layers required for the needle-phase to exist. Needle islands nucleate preferentially at defects and step edges, a behavior described previously

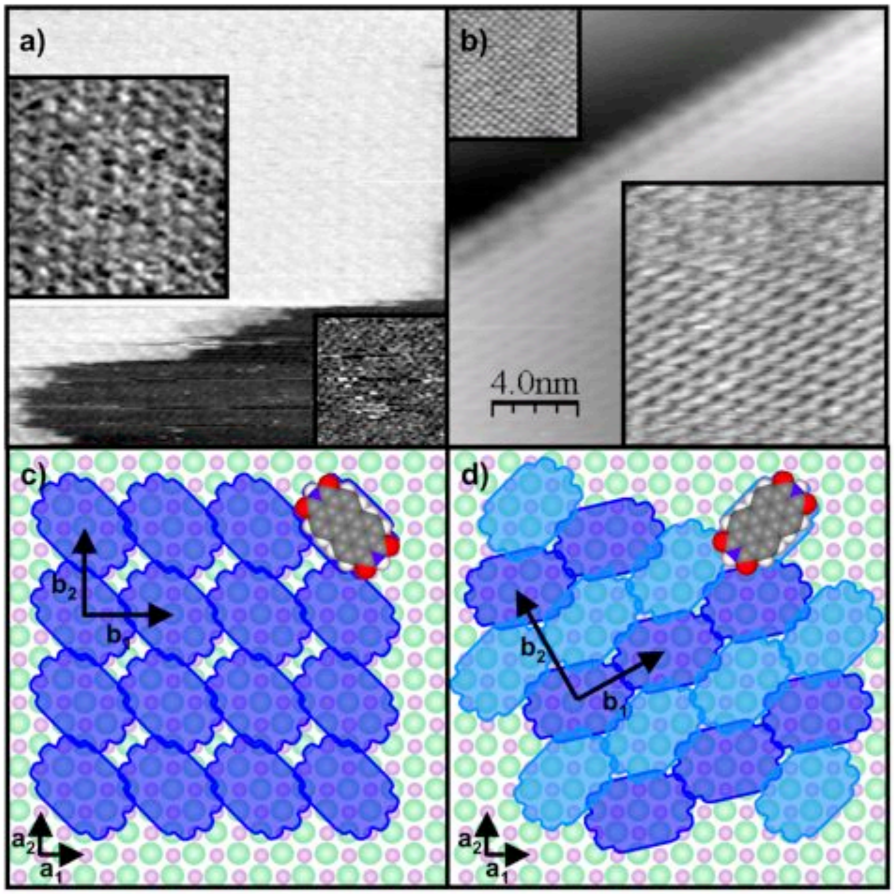

Figure 2.1: (a,c) Molecular and atomic resolution images of (a) a 1 ML square island of PTCDI on NaCl, Δf = -15 Hz, and (b) a multilayer needle island of PTCDI on NaCl, Δf = -24 Hz. Large and small inset regions of PTCDI and NaCl respectively have been flattened and adjusted for contrast to make the structures more visible using WSxM [77]. (c) (2×2) brick wall square island structure. (d) Needle island structure (top layer of molecules only shown for clarity).

for stable C_{60} islands on KBr [66]. The more densely packed crystalline structure of the needle islands resembles those determined for PTCDI on a variety of other substrates as well as the bulk $(10\bar{2})$ plane [6–14]. However, the bulk $(10\bar{2})$ is slightly corrugated with slightly smaller lattice parameters than the flat-lying structures typically observed on surfaces [5]. Lattice parameters determined from molecular and atomic resolution images for both needle and square islands are given in Table 2.1.

Structure	b_1 (Å)	b_2 (Å)	θ (°)	β (°)
Square	11.3 ± 0.4	10.9 ± 0.8	1 ± 3	93 ± 4
Needle	13.2 ± 0.3	16.5 ± 0.4	29 ± 1	90 ± 2

Table 2.1: Square and needle island structure parameters

2.3.3 Overlayer Epitaxy

The lattice vectors of an adsorbed species may be related as a linear combination of the underlying substrate lattice vectors (illustrated in Fig.2.2) by a transformation matrix, *[C]* [5]:

$$\begin{bmatrix} \vec{b_1} \\ \vec{b_2} \end{bmatrix} = [C] \begin{bmatrix} \vec{a_1} \\ \vec{a_2} \end{bmatrix} = \begin{bmatrix} p & q \\ r & s \end{bmatrix} \begin{bmatrix} \vec{a_1} \\ \vec{a_2} \end{bmatrix}, \tag{2.1}$$

where the $\vec{a_n}$ are the substrate lattice vectors (taken as exactly 0.565 nm on NaCl and 0.660 nm on KBr with angle α = 90°) and the $\vec{b_n}$ correspond to the molecular island lattice vectors given in Table 2.1.

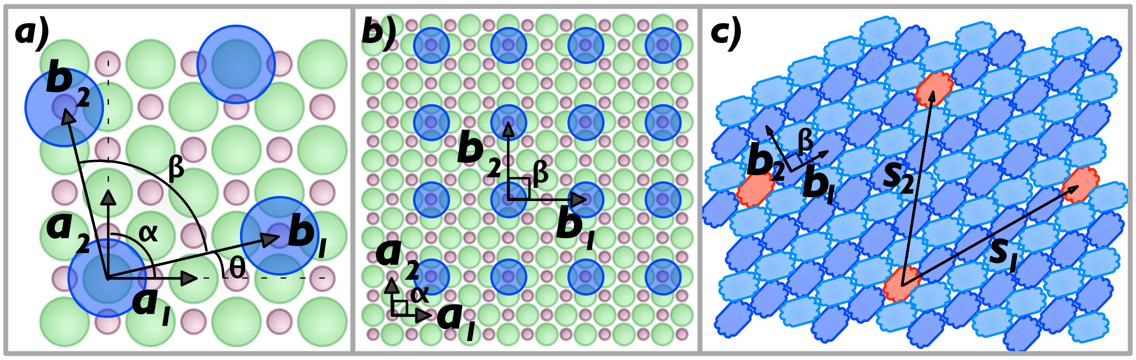

Figure 2.2: (a) The seven parameters used to describe an epitaxial interface, illustrated for an alkali halide substrate (green and pink) with an arbitrary molecular overlayer (blue). (b) The (2×2) structure observed for square shaped islands on NaCl. (c) The needle island structure with red molecules indicating the superstructure observed on NaCl in Fig.2.3

We interpret the square shaped island epitaxy as simply:

$$[C_{square}] = \begin{bmatrix} 2 & 0 \\ 0 & 2 \end{bmatrix}, \tag{2.2}$$

which may be given in terms of Wood's notation as (2×2). Because every overlayer lattice site coincides with a symmetry equivalent substrate lattice site, it is considered *commensurate* [5].

The needle island epitaxy is more complicated. The transformation matrices relating the epitaxy of needle islands of PTCDI on NaCl are calculated from the measured lattice parameters as:

$$[C_{needleNaCl}] = \begin{bmatrix} 2.04 \pm 0.05 & 1.13 \pm 0.04 \\ -1.42 \pm 0.10 & 2.55 \pm 0.06 \end{bmatrix}. \tag{2.3}$$

This overlayer structure is not commensurate, since molecules sit over a variety

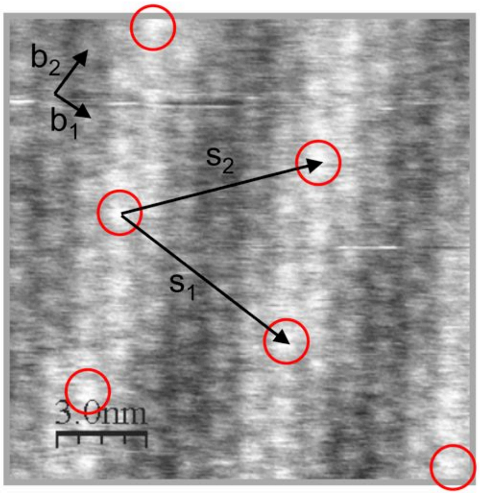

Figure 2.3: 15 nm x 15 nm, Δf = -20 Hz image of the top of a 3 layer tall needle island, with bright molecules circled to highlight periodicity. The opposite canting of adjacent rows is also visible, as illustrated in Fig.2.1d.

of different substrate lattice sites. Because only one of the matrix coefficients is an integer within error, the long range ordering of the overlayer structure is not immediately apparent. However, the observation of a Moiré pattern, such as in Fig.2.3 suggests that registry with the substrate lattice exists. Although the film is not commensurate, it may be *coincident* [5]. According to the terminology of Hooks *et. al.*, it is most likely coincidence-II [5].

If a superstructure exists, molecules should be in equivalent position with respect to the substrate at points separated by some integer multiples of both the $\vec{b_n}$ and $\vec{a_n}$. The bright spots in Fig.2.3 correspond to:

$$\begin{bmatrix} \vec{s_1} \\ \vec{s_2} \end{bmatrix} = \begin{bmatrix} 5 & 0 \\ 3 & 3 \end{bmatrix} \begin{bmatrix} \vec{b_1} \\ \vec{b_2} \end{bmatrix}, \tag{2.4}$$

Or an equivalent unit cell can be defined with the same area, for example:

$$\begin{bmatrix} \vec{s_1} \\ \vec{s_2} \end{bmatrix} = \begin{bmatrix} 3 & 3 \\ -2 & 3 \end{bmatrix} \begin{bmatrix} \vec{b_1} \\ \vec{b_2} \end{bmatrix} . \tag{2.5}$$

Taking the first option and using our transformation matrix *[C]* to find the superstructure in terms of the $\vec{a_n}$, we find:

$$\begin{bmatrix} \vec{s_1} \\ \vec{s_2} \end{bmatrix} = \begin{bmatrix} 10.2 \pm 0.2 & 6.1 \pm 0.2 \\ 1.9 \pm 0.3 & 11.1 \pm 0.2 \end{bmatrix} \begin{bmatrix} \vec{a_1} \\ \vec{a_2} \end{bmatrix} . \tag{2.6}$$

These correspond to integer values within error. We also note that other superstructures may exist as a result of strain relaxation in upper layers, or different needle islands may have slightly different structures with respect to the substrate. Modelling is needed to determine the energetically most favourable structure and if other structures with similar energies exist.

2.4 Dewetting

At room temperature, the metastable square islands shrink and disappear within days of deposition, while the stable needle islands grow larger, as illustrated in Fig.2.4. Other images were taken well outside of the consecutively imaged area to ensure that the NC-AFM tip did not influence the dewetting dynamics and indeed showed the same dewetting progress, shown in Fig.2.5. Needle islands grow in both height and area, and tend to elongate rather than widen. This anisotropy is expected, given the hydrogen bonding that typically causes PTCDI molecules to form rows. The square islands of PTCDI on NaCl are comparable to the "metastable 2D islands" of Au observed on $SrTiO_3(001)$ by Silly and Castell [72], the "transitional morphologies" of Ag on Si(111) [70] described by Thurmer *et al.* [70], as well as the metastable ML $p(3 \times 3)$ structure of PTCDA molecules on NaCl reported by Burke *et al.* [16], all of which dewet upon annealing.

2.4.1 Evolution of Island Populations

The population of molecules in each island type was calculated from the measured volumes and density calculated from the lattice constants determined above and a measured needle interlayer spacing of 0.315 ± 0.015 nm (assuming the same interlayer spacing for the square structure, a reasonable assumption for perylenes [7]).

$$P_{isltype} = \bar{h}_{isltype} n_{molec} \sum A_{isl}, \tag{2.7}$$

where $P_{isltype}$ is the number of molecules in each island type per image, $\bar{h}_{isltype}$ is the average island height for each type per image, n_{molec} is the molecule number density and A_{isl} is the area of each island. The resulting populations were plotted as functions of time and fit as shown in Fig.2.4h. Error bars represent one standard deviation of population per island type per image (propagated from measurement uncertainties of height, density and island area), and are particularly large in the needle island case due to the distributions of component measurements, for example variations in needle island height (some islands straddle multiple terraces and/or have incomplete upper layers).

An empirical fit was used to quantify the timescale of the dewetting transition. The growth function found to best fit the data for the needle (stable) islands

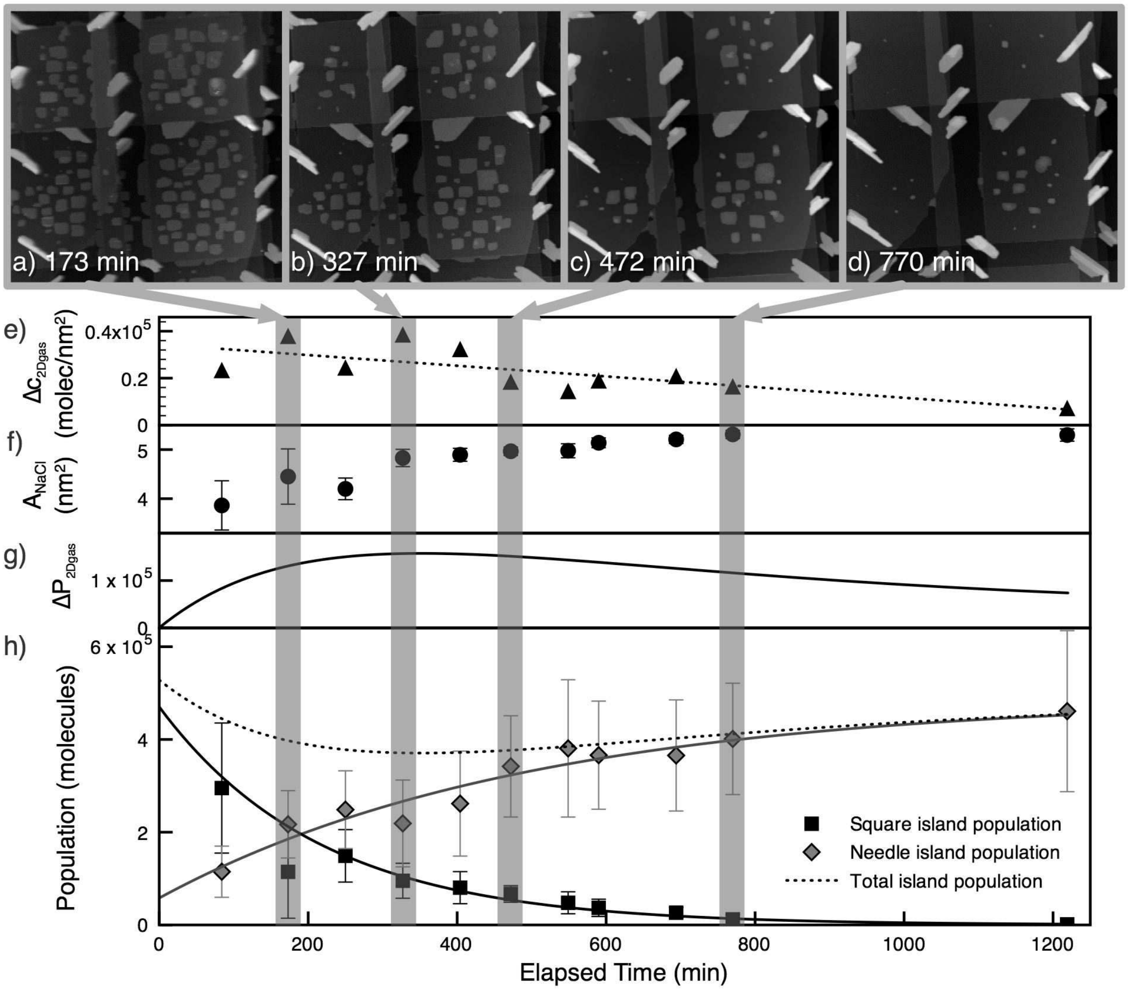

Figure 2.4: Post-deposition growth of needle islands and the disappearance of square islands over time. (a-d) 770 nm x 770 nm, Δf = -2 to -4 Hz, 0.3 ML PTCDI on NaCl images and corresponding time since deposition, with both square and needle shaped islands visible. (e) Differential concentration of 2D molecular gas (molecules/nm^2), (f) area of exposed NaCl substrate, (g) differential population of 2D molecular gas (population less an unknown steady state offset), and (h) population of square and needle islands plotted as functions of time, with monomolecular growth and decay fits.

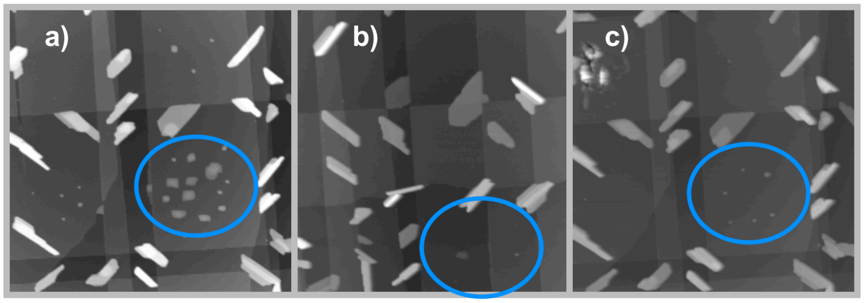

Figure 2.5: 770 nm x 770 nm NC-AFM images verifying that dewetting is not tip-induced: (a) taken at elapsed time 770 min in movie spot, (b) at 877 min hundreds of nm away, (c) elapsed time 1208 min. Circles indicate areas in which square islands are present.

is that of monomolecular growth, which is generally used to describe growth of biological systems [78]. This function assumes that the growth rate of a particle (island) is proportional to the difference between the current and final size which is consistent with a finite number of units (molecules) in the system. As the particle size increases the growth rate slows due to the reduction in available resources from the background concentration field.

$$\frac{dP}{dt} = \frac{1}{\tau}\left(P_\infty - P\right), \tag{2.8}$$

where P is the current population of molecules (size of the island), τ is a time constant $\tau > 0$, and P_∞ is the final population of molecules in the island. Considering the stable islands as sinks for the background concentration field, the right hand term can also be considered a flow of molecules into the island: the change in island size corresponds to the number of molecules that arrive and attach in a characteristic time. In this way, the time constant τ encapsulates both diffusion and attachment parameters. This solves to the growth function:

$$P = P_\infty - \delta e^{-\frac{t}{\tau}}, \tag{2.9}$$

where δ is the difference between the initial and final populations $(P_\infty - P_o)$.

An analogous decay function was fit to the square island population:

$$P = P_o e^{-\frac{t}{\tau}}, \tag{2.10}$$

which similarly illustrates the flow of molecules out of these islands.

Island Type	Needle	Square
$P_\infty\,(\times 10^5)$	50 ± 9	0
$P_o\,(\times 10^5)$	6 ± 7	48 ± 8
$\tau(min)$	500 ± 200	220 ± 10

Table 2.2: Fit parameters for monomolecular growth/decay of needle/square islands of 0.3 ML PTCDI in 770 nm x 770 nm area.

The fit parameters for both island types are given in Table 2.2. P_o and P_∞ are the initial and post-dewetting island populations, but the time constant τ provides some quantitative insight into the dynamics of dewetting and could be used for comparison with modeling. τ_{Needle} and τ_{Square} reflect the net capture rate of molecules into the needle islands and the net escape rate out of the square islands respectively. The diffusion constant, coverage, step density, geometry, and sticking probability for different island edges are all factors which will affect τ. The rate of dewetting is expected to be tuneable by adjusting experimental parameters such as temperature [16] and substrate preparation to induce desired film behaviour (explored in Chapter 3) . An independent data set with significantly lower step density and 0.2 ML coverage was observed to dewet with just over double the above τ values (shown in Fig.2.6 and Table 2.3) and produced considerably larger islands, demonstrating the combined influence of substrate structure and coverage. Due to the predominant nucleation of needle islands at step edges, the dewetting process is dependent upon the initial state of the sample and is highly sensitive to substrate structure. Substrate areas with high step density tend to contain many small needle islands and dewet quickly, while areas with low step density tend to slowly form fewer, larger islands as dewetting is limited by diffusion and nucleation site density. The influence of these parameters on the timescale for dewetting is a subject of future interest.

Island Type	Needle	Square
$P_\infty\,(\times 10^5)$	7.9 ± 0.2	0
$P_o\,(\times 10^5)$	0.2 ± 0.2	9.1 ± 0.6
$\tau(min)$	1180 ± 60	480 ± 20

Table 2.3: Independent data set fit parameters for monomolecular growth/decay of needle/square islands, 0.2 ML PTCDI in 400 nm x 400 nm area. The τ values for this data set are just over double those for the main data set, which had a higher coverage (0.3 ML) and step density. The ratio of τ_{Needle} to τ_{Square} is consistent (~2.5) for both data sets

The observed dynamical behaviour of PTCDI dewetting is similar to that recently reported by Käfer *et al.* for pentacene on SiO_2 and gold [79]. The transition from the "thin film phase" of pentacene to a bulk-like phase was monitored dynamically by x-ray photoelectron spectroscopy measurements of the covered and bare surface areas. The surface area covered with pentacene, i.e., the total integrated base of all islands, was found to fit well to a sigmoidal Weibull function which transitions from the initial covered area to the final covered area exponentially. Although the time constants found in that study differ by approximately an order of magnitude (likely a result of faster diffusion of pentacene on SiO_2 and gold than the larger PTCDI on NaCl), the dynamical behaviour is strikingly similar.

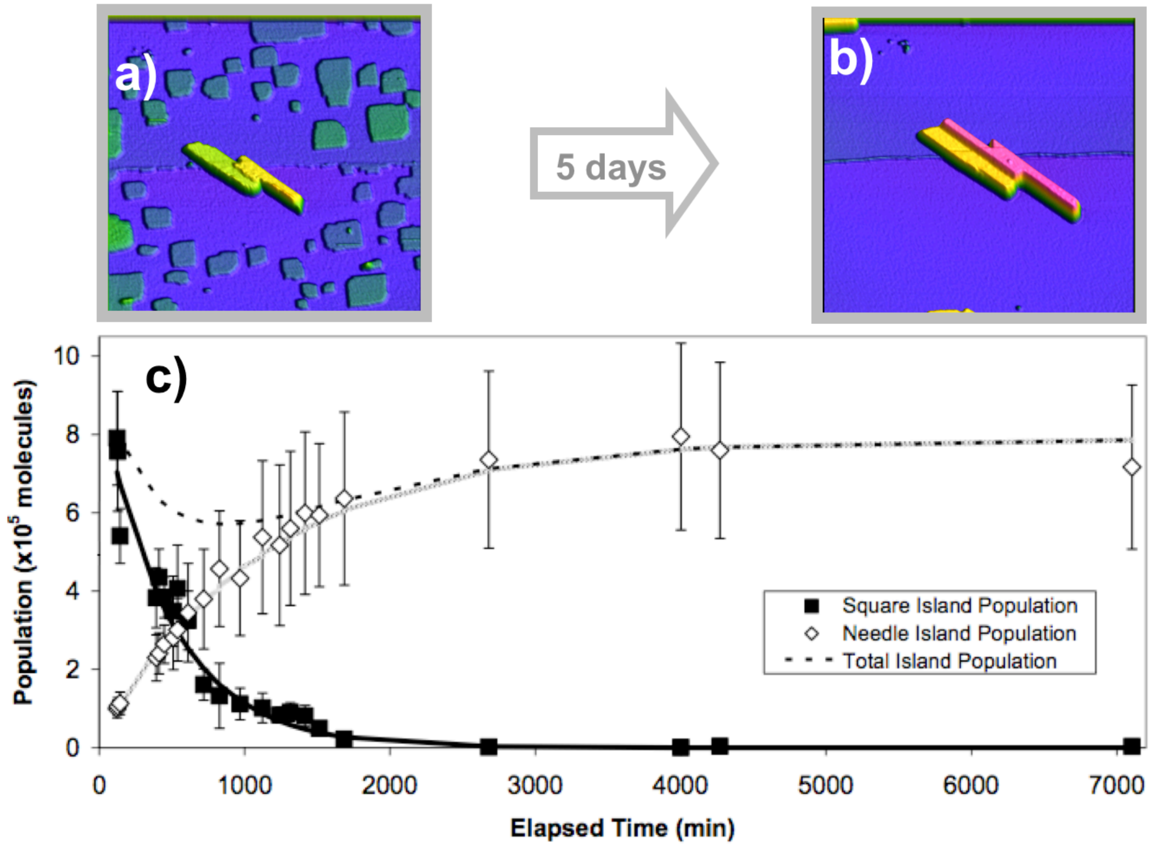

Figure 2.6: (a and b) 400 nm x 400 nm NC-AFM images (3D rendered to show texture) illustrating (a)“before” and (b) “after” dewetting of an independent data set, 0.2 ML of PTCDI on NaCl under RT and UHV conditions, elapsed time $\sim$ 5 days, Δf $\sim$ -4 Hz. (c) Island populations as a function of time. Note how the total island population dip and subsequent increase described in the main body of the paper are verified. The main data set provides a better sampling of the population as it encloses a larger area and includes many of each island type, whereas this data set contains only a single needle shaped island, but the trend is clear.

2.4.2 2D Molecular Gas

If the flux of molecules out of the square islands equals the flux into the needle islands (steady state), then τ should be the same for both fits and they should sum to a constant (assuming negligible desorption at room temperature). This is not the case (as verified by the independent data set, see Fig.2.6). Since τ is shorter for the square islands and, as they dewet, additional NaCl surface area is exposed, we propose that the lost population of molecules go into another state, diffusing over the surface in the form of a 2D molecular gas [80] faster than the AFM is able to image.

To support the assumption that the AFM is unable to image diffusing molecules we use the lattice gas model and assume a low 2D gas density such that molecules move by thermally activated hopping between adjacent sites at frequency ν [67]:

$$\nu = \nu_0 e^{-\frac{E_D}{k_B T}}, \tag{2.11}$$

where ν_0 is the attempt frequency, E_D is the diffusion barrier, k_B is the Boltzmann constant and T is the temperature. Taking estimated values of $\nu_0 = 10^{13}$ Hz [67,81], $E_D = 0.4$ eV [82] and room temperature, we calculate a hopping frequency of $\nu = 2 \times 10^6$ Hz. The probability of a molecule remaining on the same site for time t is [67]:

$$\mathbb{P} = e^{-\nu t}, \tag{2.12}$$

and taking a typical AFM scan speed of 1.67 ms per pixel as t, we find a vanishingly small probability of a 2D gas molecule resting long enough to image for even a single point.

One must now consider 3 fluxes: the capture rate for square islands (which becomes negative after deposition), the capture rate for needle islands, and the flux in and out of the 2D gas. The sum of the three populations of molecules can be written as:

$$P_{Total} = P_{Needle} + P_{Square} + P_{2Dgas}. \tag{2.13}$$

To account for the initial decrease and subsequent increase in total island population, consider that:

$$P_{2Dgas} = c_{2Dgas} A_{NaCl}, \tag{2.14}$$

where c_{2Dgas} is the 2D gas number density or concentration, and A_{NaCl} is the area of exposed NaCl substrate. This neglects the population of molecules diffusing on the islands (which should be reduced given the energy cost of interlayer mass transport [26,83]).

The time evolution of the 2D gas population is shown in Fig.2.4g. Taking the measured differential population of the 2D gas and exposed area of the NaCl (see Fig.2.4f) as the area in which this population resides, the differential 2D concentration can be calculated as a function of time (see Fig.2.4e). An undetermined offset may also be present. The decreasing number density of the 2D gas reflects a concentration field which is not constant with time, but rather becomes depleted as molecules are incorporated into the stable needle island population and fewer molecules are supplied by the square islands. P_{2Dgas} initially increases as more A_{NaCl} is exposed by dewetting, then decreases with c_{2Dgas} as A_{NaCl} approaches a constant (see Fig.2.4g). This differs with other models of ripening behaviour which usually consider a constant concentration field. This is also consistent with the observation that no significant further ripening of the needle islands is observed after the total consumption of the metastable island population.

2.4.3 Evolution of Island Size Distribution

The use of a scanning probe technique also allows for an analysis of the size distribution of the islands and how these evolve with time. Fig.2.7 shows the island volume distributions of the square and needle islands at different times. The square islands decrease in both size and number, as can be seen from the histograms which shift towards smaller island volume. The needle islands both grow in size and have increasingly broad distributions. At longer times, the needle islands also appear to exhibit a large size tail which is atypical of processes such as Ostwald ripening.

Several factors may influence the observed size distribution evolution. In typical coarsening scenarios, the background concentration field is assumed (a) constant, and (b) homogeneous. As shown for the dewetting process observed here, the concentration field feeding the growth of stable needle islands decreases with time, limiting the growth process. The needle islands act as sinks (with higher stability and higher sticking probability) and the square islands act as sources (with lower stability and therefore higher molecule escape probability). Close inspection of the images reveals that the square islands closest to the needle islands dewet faster than those farther away, resulting in clusters of square islands of which the edge islands shrink and disappear first, creating depletion regions (see Fig.2.4 and Fig.2.6). If the cluster of square islands is large, edge islands may also appear to retreat from the needle islands (see Appendix A). Shrinking indicates that the net flux of molecules out of a square island is greater than the flux in, and retreating indicates that the flux of molecules in and out of an island is not isotropic. Since all sides of the square islands are crystallographically equivalent (see Fig.2.1c), a difference in flux indicates a difference in the local 2D gas

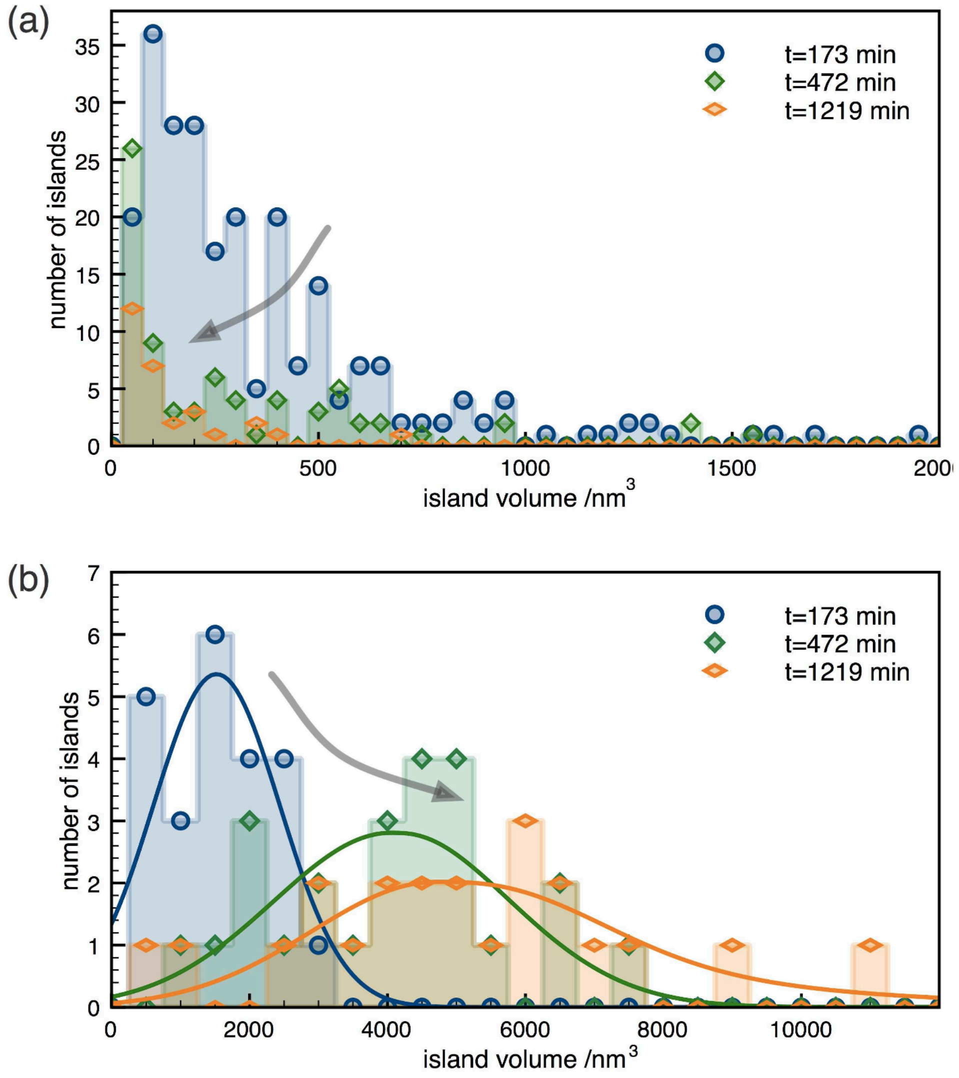

Figure 2.7: Island volume histograms of (a) square (metastable) islands and (b) needle (stable) islands for three different times. Solid lines in (b) are fits to a gaussian with an exponential tail and are intended only as a guide to the eye.

number density. In other words, this indicates that the 2D gas number density is lower near the growing needle islands and higher among clusters of the metastable square islands. Under this interpretation, the steady-state 2D gas number density required to maintain a constant square island population (independent of any Ostwald ripening which might occur within this population) would be higher than that for a constant needle island population; hence the bimodal system dewets. The difference in time scales between the disappearance of square (metastable) and growth of needle (stable) islands supports the supposition that the background concentration field is inhomogeneous.

We also observe that the needle islands do not grow isotropically, but rather have different growth rates in each dimension, growing fastest in length: $dl/dt > dh/dt, dw/dt$. An added complication in analyzing the size distributions of the needle islands arises from the tendency for these islands to nucleate at steps or other defects. Ideally, the dewetting process would be studied on a perfect flat crystalline terrace so that the homogeneous growth of the needle islands would not be influenced by adjacent islands. However, due to the surprisingly large diffusion length observed for PTCDI on NaCl, as with other molecules on alkali halides [16, 66], needle islands are always heterogeneously distributed at step edges or other defects, which act as traps [25] and may result in non-negligible spatial correlations between neighbouring islands. For example, adjacent needle islands in similar orientations occasionally coalesce, but growth towards a perpendicular neighbouring island has been observed to cease before coalescence can occur (see Appendix A).

2.5 Summary

Bimodal growth and post-deposition dewetting of PTCDI on NaCl have been observed. Molecules diffuse out of metastable square islands to join more energetically favorable needle islands over time. We find that the dynamics of this transition are empirically well described by the monomolecular growth model, which is anticipated to be applicable to bimodal systems in general, though the dewetting timescale may vary significantly. The dynamics of dewetting quantified here are expected to be tunable via experimental parameters (such as temperature, substrate preparation, etc.), which can also impact the resulting growth structures. The characterization of the influence of these factors is a subject for continued exploration. Comparative modeling, such as within a Kinetic Monte Carlo framework [84, 85], is required to discern the effect of kinetic factors and individual molecular scale processes on the overall growth dynamics, for which this quantitative analysis provides a basis. The characterization and understanding of this dynamical evolution is an important step in controlling the structure of thin organic films for nanoscale devices which are sensitive to the nanoscale film structure.

3

Tailoring Morphology

THIS CHAPTER IS BASED ON:

J.M. Topple, S.A. Burke, W. Ji, S. Fostner , A. Tekiel and P. Grutter, *Tailoring the Morphology and Dewetting of an Organic Thin Film*. J. Phys. Chem. C, 115(1), 217-224, (2011)

3.1 Morphology

The morphology of thin films in organic electronic devices is a crucial parameter, as film structure has a strong influence on application relevant properties [4, 5, 46, 86–88]. Film morphology can be controlled to some degree by growth conditions [2, 16], but post-deposition dynamic processes such as dewetting (Fig.3.1) and other forms of ripening can alter the film structure and resulting properties [16, 69–73, 89–92], potentially leading to problems with device stability and functionality.

Recent interest in organic semiconductors has motivated research on a variety of organic materials for electronic and optoelectronic applications [1–3, 88]. Perylene derivatives are one such class of organic semiconducting molecules which are easily modified [6–15], and this chapter will continue our investigation of the controlled growth of 3,4,9,10-perylenetetracarboxylic diimide (PTCDI). Thin

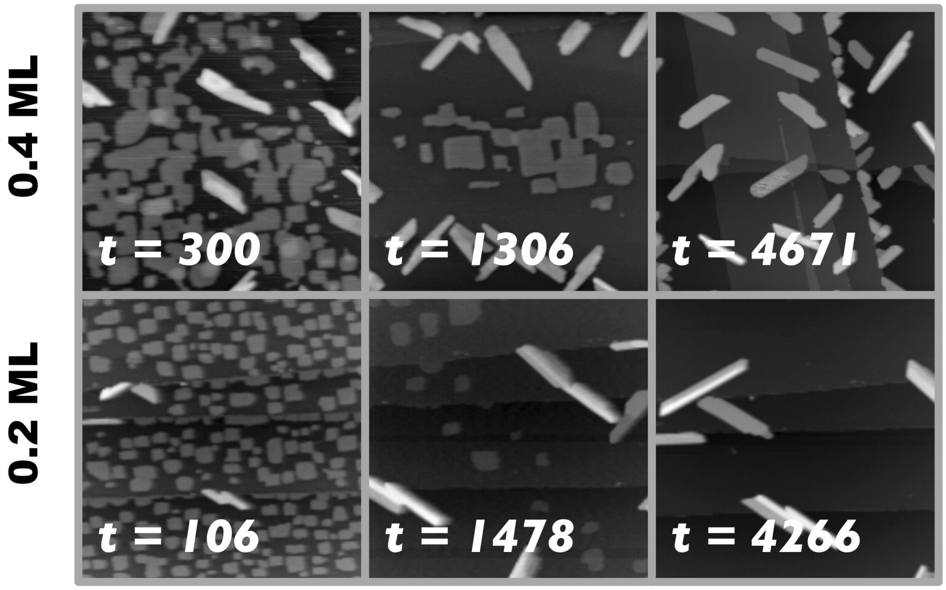

Figure 3.1: Dewetting of PTCDI on NaCl for two coverages with elapsed times (minutes) since deposition. All images 600 nm×600 nm, Δf = (top row) -3.7, -2.2, -4.0 (bottom row) -1.9, -2.4, -3.9 Hz; corresponding normalized frequency shifts Γ = -0.5, -0.3, -0.6 and -0.3, -0.3, -0.6 fN$\sqrt{m}$

films of a range of organic molecules have been studied on many different substrates (see recent reviews [4, 5] and references therein). A variety of thin molecular films deposited on insulators have been successfully imaged using NC-AFM [15, 65–67, 93–96]. Such studies address the question of which structures and growth modes occur and why, prompting the next question: Can we control the result?

Controlling and tailoring the structure of organic thin films, as well as the maturation time to reach a stable device-ready film structure is a desirable ability. This chapter explores control over thin film morphology by adjusting growth parameters such as temperature and by varying substrate structure in three ways:

1. Templating with pits
2. Templating with gold nanoclusters

3. With use of two different alkali-halide substrates.

When deposited on room temperature NaCl (001), PTCDI molecules undergo post-deposition dewetting in a dynamic process described in Chapter 2, [91]. Heating can induce enhanced Ostwald ripening within a molecular island population. By selectively distributing nucleation sites for island growth (in Volmer-Weber thin films), the resulting film morphology and homogeneity may be altered. Alkali-halide substrates templated with monolayer deep rectangular pits (created by charge stimulated desorption of the surface prior to molecule deposition), have been used in previous studies [67,95,97,98] as traps for molecules and to promote the formation of molecular structures that may otherwise be unstable or meta-stable. Gold deposited on KBr has been observed to form nanoclusters [99–101] and the effect of these nanoclusters on subsequent deposition of molecules has been explored [102,103]. The structure of the interface between metal clusters and a molecular layer is of general interest for organic electronic and optoelectronic contact geometry properties [104–106]. Here the impact of templating, as well as surface structure and other growth parameters on film growth behaviour and morphology are shown to provide means of tailoring of island dimensions and subsequently film continuity, homogeneity and surface area for films of given coverages. This will consequently affect optoelectronic and other size and structure dependent properties [4,5,46,86–88].

3.2 Growth on Atomically Flat Alkali-Halides

When deposited on NaCl (001) at room temperature, PTCDI molecules initially form two coexisting island growth structures: square-shaped islands and needle-shaped islands. The metastable square islands dewet into the stable needle islands within days of deposition (see Fig.3.1), as escaping edge molecules diffuse away and join more energetically favourable sites. The dynamics of dewetting of PTCDI on NaCl was described previously, and here we explore experimental factors that can be used to control thin film morphology and enhance or inhibit dewetting.

In contrast, PTCDI deposited on KBr does not form square islands at room temperature, and has been exclusively observed to form stable needle-shaped islands similar to those found as the stable structure on NaCl (see Fig.3.2). KBr and NaCl share the same crystal structure, with different lattice constants of 0.660 nm and 0.565 nm respectively. The molecule-substrate interaction is dominated by the electrostatic interaction between the O atoms in C=O groups of PTCDI and the Na/K cations on both substrates. The metastable square-shaped island brick-wall structure that forms on NaCl is mediated by this molecule-substrate interaction, with the intermolecular spacing corresponding to the length between two Na cations (with 3 lattice periods between them) [91] like the p(3×3) structure that is formed by a similar molecule, PTCDA when deposited on NaCl [16]. Conversely, the stable needle-shaped island structures that form on both NaCl and KBr are dominated by molecule-molecule interactions and more closely resemble the bulk crystalline structure [91], forming canted rows due to hydrogen bonding between N-H end groups and the oxygen atoms of adjacent molecules [12]. The lack of formation of square-shaped islands on KBr is likely caused by the subtle difference in substrate structure, rendering the metastable square island structure that forms on NaCl unstable and unable to form on KBr.

Needle islands on NaCl are generally 2 to 3 molecular layers taller than

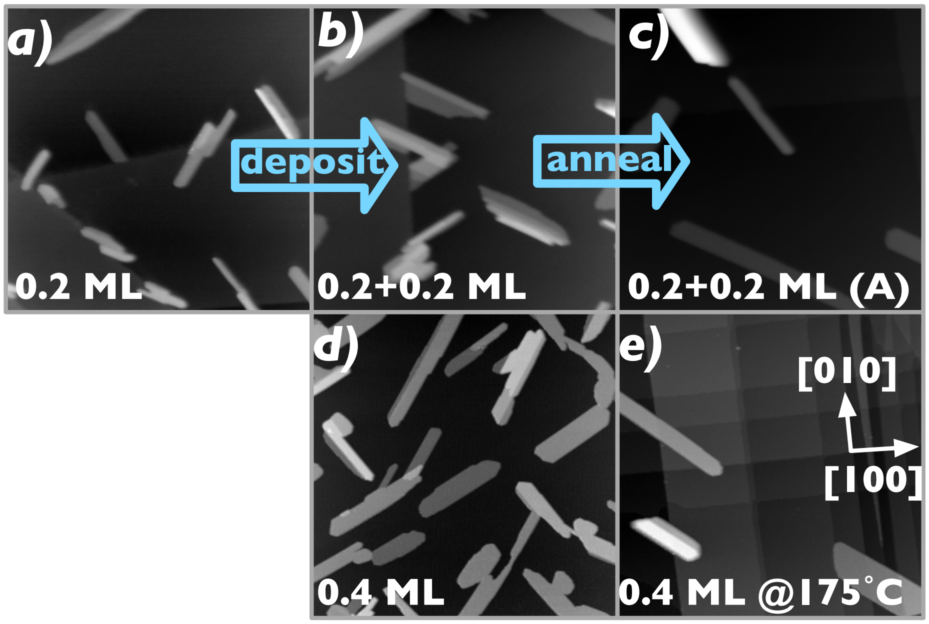

Figure 3.2: 600 nm×600 nm images of PTCDI on KBr (a-d) and NaCl (e), films consisting exclusively of needle islands. (a) 0.2 ML, Δf = -2.0 Hz; Γ = -0.3, fN$\sqrt{m}$; (b) 0.4 ML deposited in 2 subsequent depositions of 0.2 ML, on the same sample show in (a), Δf = -2.8 Hz; Γ = -0.4 fN$\sqrt{m}$; (c) the sample show in (b) after gentle heating overnight at ~150°C, Δf = -3.2 Hz; Γ = -0.4 fN$\sqrt{m}$; (d) 0.4 ML deposited in a single deposition, Δf = -3.1 Hz; Γ = -0.4 fN$\sqrt{m}$; and (e) 0.2 ML PTCDI on NaCl heated to ~175°C during deposition, note the high step density Δf = -2.0 Hz; Γ = -0.3 fN$\sqrt{m}$

those grown on KBr (discussed further below and summarized by Fig.3.3), and are otherwise similar in appearance, size, structure and stability under high resolution imaging conditions. The difference in height may be due to height dependent strain [46, 83], or may be a result of the differing substrate interactions that accommodate a metastable structure only on NaCl. Additionally, needle islands on both substrates have been observed exclusively with heights of 2 monolayers (ML) or more. Molecule-molecule interactions appear to mediate the growth and islands form a bulk-like crystalline structure, despite the substrate lattice mismatch. The mismatch may still induce some strain, but the interface structure of a multilayer island must be determined by methods other than AFM. PTCDI films deposited on NaCl can evolve for days after deposition before producing a stable film, and needle islands are always pinned to defects. On KBr, molecules readily form needle-shaped islands with apparently less selectivity over the surface position. As a general result, shorter, more densely packed needle islands form on KBr than are observed post-dewetting on NaCl for the same coverage of molecules.

3.2.1 Nucleation: The Importance of Defects

Needle-shaped islands of PTCDI on NaCl nucleate at defects (such as substrate step edges, kink sites and adsorbates) and are subsequently pinned to the nucleation site [91], similar to behaviour observed by others for C_{60} [66], DiMe-PTCDI on KBr (001) [15, 107] and Co-salen molecules [92]. Substrate step density has an important effect on the resulting film morphology, as needle islands tend to decorate step edges. PTCDI demonstrates interesting step preferences on both NaCl and KBr substrates, some of which may be observed in Fig.3.1 and Fig.3.4. NaCl and KBr cleave preferentially along the $\{100\}$ planes to maintain charge neutrality [108–110], and step edges in Fig.3.4 that appear to be along the $[\bar{1}10]$ direction are probably actually comprised of small $< 100 >$ edges with kinks [111–113] (however, this remains to be experimentally verified and corroborated with theory. Surface step edge structure in alkali-halides is surprisingly unstudied and difficult to predict, given the non-equilibrium nature of formation under UHV where dynamic surface adsorption-desorption relaxation mechanisms are not at play [114, 115]. This problem may be best addressed by a stress-induced materials failure approach such as random walk crack propagation [116, 117] but has received little attention since the 1970's). Needle-shaped islands of PTCDI on KBr are occasionally observed in the middle of terraces, but preferentially nucleate

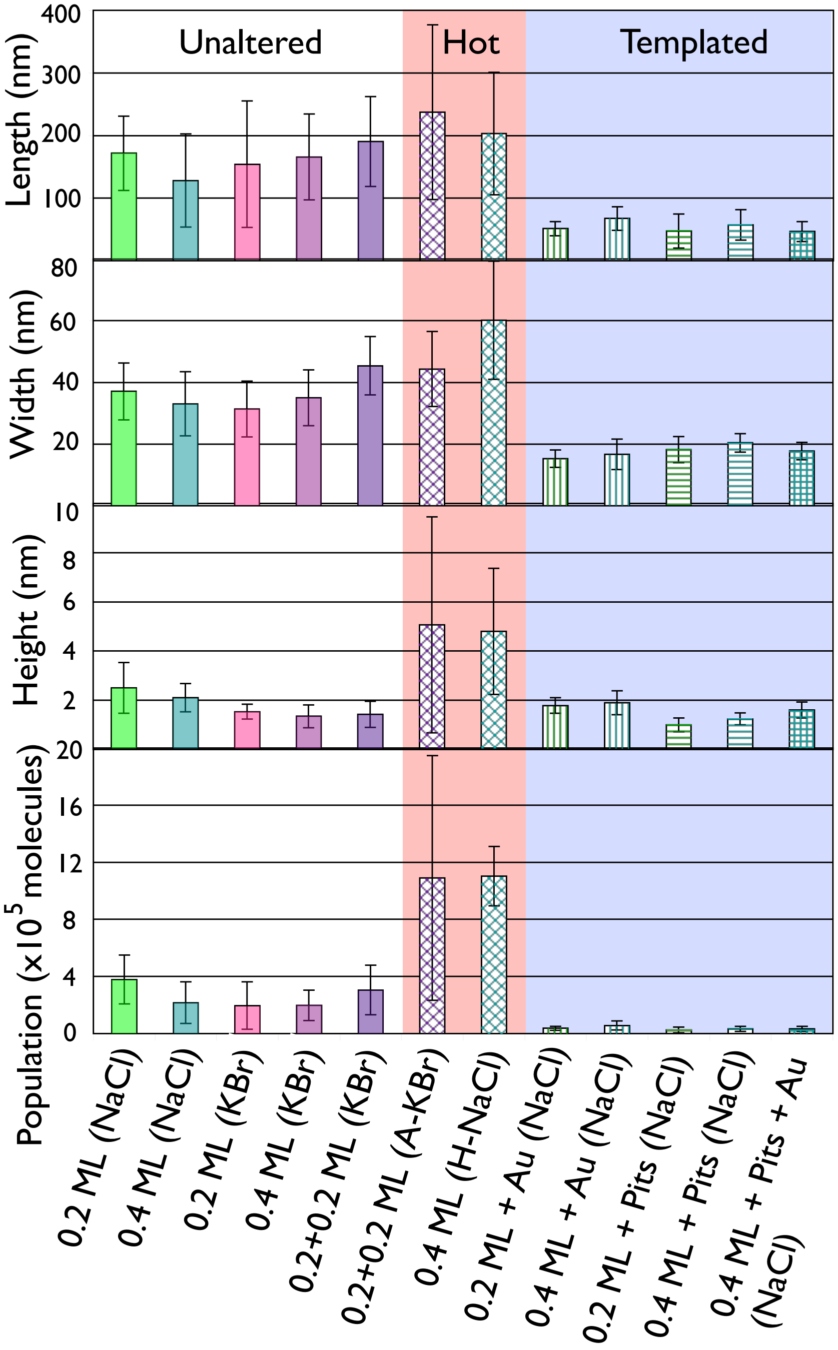

Figure 3.3: Post-dewetting needle island average length, width, height and population per island with standard deviations for varying coverages and substrate structures. Standard deviations are indicative of broad distributions from variation between islands, not measurement uncertainty. Uncertainty on individual island measurements generally ranges from approximately 3% for large islands to 12% for small islands. "A-" and "H-" indicate samples that were annealed after growth or heated during molecule deposition respectively.

Table 3.1: Post-dewetting needle island average length, width, height, area, volume and population per island with standard deviations for varying coverages and substrate structures. Note: Standard deviations are indicative of broad distributions from variation between islands, not measurement uncertainty. Uncertainty on individual island measurements generally ranges from approximately 3% for large islands to 12% for small islands. “A-” and “H-” indicate samples that were annealed after growth or heated during molecule deposition respectively.

Experiment	$\bar{l}$ (nm)	$\bar{w}$ (nm)	$\bar{h}$ (nm)	$\bar{A}$ (nm^2)	$\bar{V}$ (nm^3)	$\bar{n}$ (molecules)
0.2 ML (NaCl)	170 ± 60	37 ± 9	2.5 ± 1.0	5300 ± 1900	13000 ± 6000	38000 ± 17000
0.4 ML (NaCl)	130 ± 70	33 ± 10	2.1 ± 0.9	4300 ± 2000	7400 ± 5000	22000 ± 15000
0.2 ML (KBr)	150 ± 100	31 ± 9	1.5 ± 0.3	5000 ± 4400	7500 ± 6400	20000 ± 17000
0.4 ML (KBr)	170 ± 70	35 ± 9	1.4 ± 0.5	6100 ± 3500	7600 ± 4100	20000 ± 11000
0.2+0.2 ML (KBr)	190 ± 70	45 ± 9	1.4 ± 0.5	8500 ± 4700	12000 ± 7000	31000 ± 17000
0.2+0.2 ML (A-KBr)	240 ± 140	44 ± 12	5.1 ± 4.4	9400 ± 5900	42000 ± 33000	109000 ± 86000
0.4 ML (H-NaCl)	200 ± 100	60 ± 19	4.8 ± 2.6	11000 ± 6000	42000 ± 8000	110000 ± 21000
0.2 ML Au (NaCl)	50 ± 10	15 ± 3	1.8 ± 0.3	700 ± 200	1300 ± 500	3700 ± 1400
0.4 ML Au (NaCl)	70 ± 20	17 ± 5	1.9 ± 0.5	1000 ± 400	1900 ± 1100	5700 ± 3200
0.2 ML Pits (NaCl)	50 ± 30	18 ± 4	1.0 ± 0.3	800 ± 500	800 ± 700	2500 ± 2000
0.4 ML Pits (NaCl)	60 ± 25	20 ± 3	1.2 ± 0.2	900 ± 400	1200 ± 600	3400 ± 1700
0.4 ML Au+Pits (NaCl)	50 ± 20	18 ± 3	1.6 ± 0.3	700 ± 300	1100 ± 600	3200 ± 1800

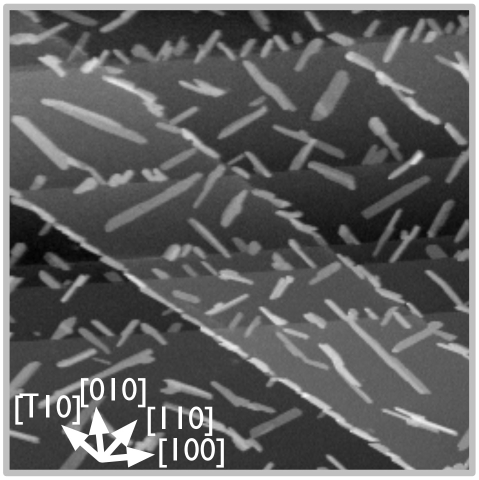

Figure 3.4: 1000 nm×1000 nm image of 0.5 ML PTCDI on KBr showing needle islands nucleating from a variety of different step edges, Δf = -2.0 Hz; Γ = -0.3 fN$\sqrt{m}$

from step edges. A contrasting behaviour for a similar molecule was observed by Fendrich *et al.*, who described DiMe-PTCDI molecules deposited on NaCl and KBr to form molecular wires requiring step edges for stability on KBr while loose ends were stable on NaCl [15].

Double steps (two atomic layers tall) in NaCl and KBr appear to be excellent nucleation sites for needle islands, and are often nearly completely covered by smaller than average needle islands on the bottom side (see top right image in Fig.3.1), presumably due to enhanced interaction between the oxygen atoms of PTCDI and the second level sodium ions which become accessible and promote stacking. Needle islands nucleated at single steps often straddle both sides of the step. A single NaCl step is not tall enough for second layer PTCDI molecules to reach the NaCl atoms (with a step height of 0.283 nm versus island layer height of ∼0.315 nm [7,91]), thus the lack of sodium ion interaction for second level molecules may account for the reduced density of needle islands nucleated at single step edges. The long axis of molecular islands are often approximately parallel to the $< 110 >$ directions of the substrate. Islands tend to grow following the double step edges if the steps are approximately along the $< 110 >$ directions of the substrate (see Fig.3.4), while steps approximately along the $< 100 >$ directions of the substrate tend to nucleate islands that do not follow the step edge and have shorter than average length. Gold clusters and other adsorbates in general are less selective and tend to decorate any step edge, and can subsequently nucleate PTCDI needle island growth.

3.3 Making Islands Larger

3.3.1 Additional Deposition

Additional molecules may be deposited onto a stable film to increase molecular island size without drastically changing the distribution of islands over the surface. 0.2 ML of PTCDI were deposited on KBr to produce a stable film, the film was imaged (Fig.3.2a), and then an additional 0.2 ML were deposited the next day (Fig.3.2b). A single deposition of 0.4 ML is shown for comparison in Fig.3.2d (and see Fig.3.3 for resulting island dimensions). The film produced after the second deposition of 0.2 ML (Fig.3.2b) contained islands that were longer, wider but similar in height and surface distribution to those observed after the initial 0.2 ML deposition (Fig.3.2a). Analysis of several images suggests that molecules of the second deposition generally join existing layers of islands without nucleating new islands or layers. It is reasonable to assume that the edges of previously established islands provide the most energetically favourable binding sites. When compared to a single deposition of 0.4 ML (Fig.3.2d), the doubly deposited film contained islands which were again longer, wider, and similar in height, yet the doubly deposited islands had a larger inter-island spacing (note that the substrate step density plays a role in dictating the island surface distribution and dimensions, and will be discussed further below). Therefore, it appears possible to set the island surface distribution with an initial deposition, and then increase the island size with subsequent depositions.

3.3.2 Heating

Heating of a stable film after growth (annealing) can be used to induce Ostwald ripening and increase the size of compact islands while thinning out the distribution of islands over the surface. The KBr sample discussed above (Fig.3.2a and b) was subsequently annealed at ∼150°C overnight. After annealing (Fig.3.2c), the islands observed were longer, spread farther apart, and many were significantly taller than those observed prior to heating. The tallest island observed was 13 nm tall, corresponding to a height of about 40 molecular layers. Alternatively, a sample may be heated during molecule deposition to influence growth in a similar way, again resulting in larger islands. Deposition onto a warm NaCl substrate (∼175°C, Fig.3.2e) exclusively produces large needle-shaped islands comparable in size to those grown on KBr (Fig.3.2c). The measured island dimension distributions are illustrated in Fig.3.3, though difficulties in finding and imaging such large islands resulted in a small number of islands (9 on annealed “A-KBr” and 8 on heated “H-NaCl”) from which to take statistics. Branched islands indicative of coalescence were rarely seen for the post-deposition annealing on KBr case (Fig.3.2c), and never observed on NaCl heated during deposition (Fig.3.2e). This, combined with the larger inter-island spacing and bare step edges that are typically decorated during room temperature deposition indicates higher mobility of the molecules. Similar observations have been made as a result of annealing for many systems [16,69–73]. Heating is a means of increasing the average island size (particularly height) [16] and inter-island spacing, thereby tailoring the morphology of the resulting thin film.

3.4 Making Islands Smaller

3.4.1 Tip Induced Nucleation

It is possible to induce site-specific nucleation by poking the sample with the AFM tip during dewetting to create a local defect, as illustrated in Fig.3.5 (see also Appendix A). Needle island growth was nucleated at a position where the AFM tip interacted with the surface, producing a small local rearrangement or indentation. This method allows for precise positioning of defects over a small range accessible by imaging, but control over a large scale is desirable for thin film device applications.

3.4.2 Surface Templating

The importance of step density lends itself to the notion that control over the density of nucleation sites can be achieved by careful modification of the surface. NaCl substrates were templated with single monolayer deep pits, gold nanoclusters, or the two combined prior to PTCDI deposition, as illustrated in Fig.3.6. Single crystal NaCl samples were cleaved *in situ* and heated to $\sim$150°C for one hour. Pits were created by irradiating the surface with charge using an electron

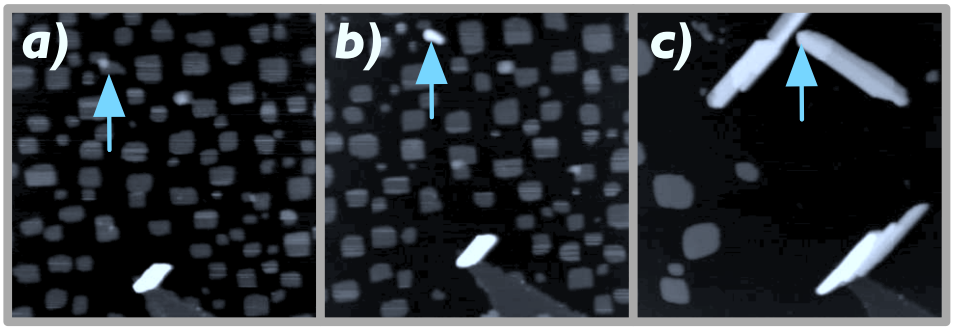

Figure 3.5: 500 nm×500 nm images of 0.2 ML PTCDI on NaCl (a) with a single needle-shaped island visible (and some unstable second layers on square islands) 203 minutes after deposition, (b) newly nucleated needle-shaped islands immediately after poke, 254 minutes after deposition, and (c) needle-shaped islands 2227 minutes after deposition. Arrow indicates indent location. Δf = -3.8, -4.0 and -4.3 Hz; Γ = -0.5, -0.6 and -0.6 fN$\sqrt{m}$

beam evaporator below the evaporation threshold, at a sample temperature of ~250°C with a charge dose of 1.2 ± 0.1 μC/cm^2. The details of pit creation are described elsewhere [46, 67, 100, 102, 118], and the average pit size and surface density can be controlled by varying the charge dosage and substrate temperature during deposition respectively. Gold was deposited using the same evaporator, at a coverage of 0.005 nm for all samples shown. A molecular evaporator was used to thermally evaporate PTCDI (Alfa Aesar, 98% purity, outgassed at 200°C overnight) at 300°C onto room temperature substrates. Deposition rates were calibrated (assuming densities of 1.7 g/cm^2 for PTCDI and 19.3 g/cm^2 for gold) using a quartz crystal microbalance. Molecule deposition rates ranged from 48 to 96 pm/min, and gold was deposited at 7 to 15 pm/min. In each experiment, substrates were imaged by NC-AFM prior to templating and after each subsequent step of surface preparation to ensure quality and a well characterized surface for PTCDI growth.

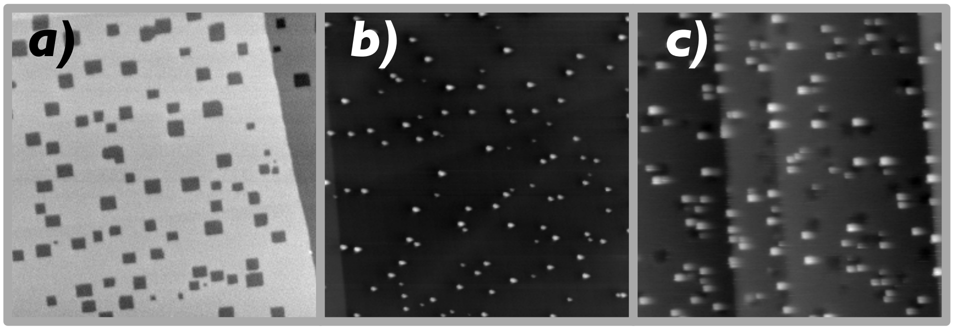

Figure 3.6: 300 × 300 nm NC-AFM images of (a) pit templated NaCl, (b) gold templated KBr and (c) NaCl templated with both pits and gold.

3.4.3 Pits

Monolayer deep rectangular pits in the NaCl substrate provide a relatively homogeneous surface distribution of kink sites over the surface which can nucleate needle-shaped islands, as shown in Fig.3.7). Pits can also act as traps for PTCDI molecules, and occasionally small, single layer islands of trapped molecules form that fill the square-shaped pit and are the only monolayer structures that are stable over long times. A comparison of dimensions for post-dewetting needle-shaped islands for varying substrate structures is given in Fig.3.3 with values listed in Table 3.1.

Complete dewetting of the square-shaped islands occurs very quickly, within an hour of PTCDI deposition, whereas un-templated (unaltered) samples may take in excess of 50 hours to completely dewet. The resulting needle islands tend to be about a factor of 10 smaller in volume and somewhat less elongated (aspect ratios of ∼2.5:1 compared to ∼4:1) than those for the same coverage on unaltered NaCl (see Fig.3.7 and Fig.3.8). The size and density of pits (and thus the separation and density of kinks) can be controlled by varying temperature and charge

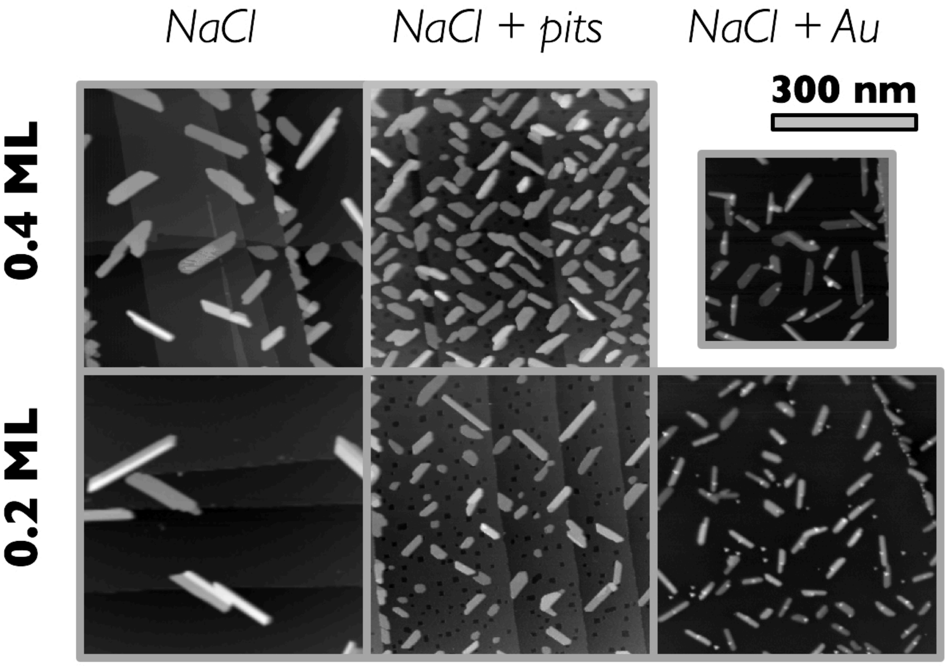

Figure 3.7: Changes in resulting film morphology with varying substrate structure. NC-AFM images of two coverages of PTCDI deposited on NaCl, Δf = (top row) -4.0, -3.0, -4.6 (bottom row) -3.9, -2.0, -2.0 Hz; Γ = -0.6, -0.4, -0.6 and -0.6, -0.3, -0.3 fN$\sqrt{m}$

dose [118]. However, double layer step edges are still favoured as nucleation sites even over the pits. Thus, it is impossible to create a totally homogeneous surface distribution on a typical NaCl sample (which contains many steps).

Fig.3.8 gives a detailed view of PTCDI growth on pit templated NaCl samples. Pit-templated samples contain molecules trapped by pits that may subsequently nucleate multilayer growth with the same crystal structure as needle-shaped islands. In some cases the needle islands appear to be confined to the pit. Such islands may nucleate later in the dewetting process (possibly due to a higher dewetting barrier) and then have a lower population of molecules to trap as the 2d gas population of diffusing molecules is depleted and thermalized. This may explain the presence of pit confined multilayer islands apparent in the 600 nm image of the 0.2 ML coverage case of Fig.3.8.

For both coverages illustrated in Fig.3.8, the multilayer islands are clearly visible while single layer pit-trapped islands are only visible for small image sizes. This lack of contrast is due to the similarity in heights of NaCl steps and PTCDI layers: NaCl pits have a depth of 0.283 nm, while PTCDI islands have a layer height of ∼0.315 nm [7, 91]. This complicates determining the population of post-dewetting pit-trapped molecules for both single and multilayer islands - multilayer islands can also include pits, and the structure and filling of molecules in covered pits cannot be determined by AFM. However, we neglect this small fraction of the molecule population in our analysis.

High resolution images of needle-shaped islands of PTCDI on NaCl, KBr and gold-templated KBr are shown in Fig.3.9. Images such as Fig.3.9(a and b) are used in the determination of crystal structure, using the visible substrate lattice as a metric. Because of the difficulty in obtaining high-resolution NC-AFM images

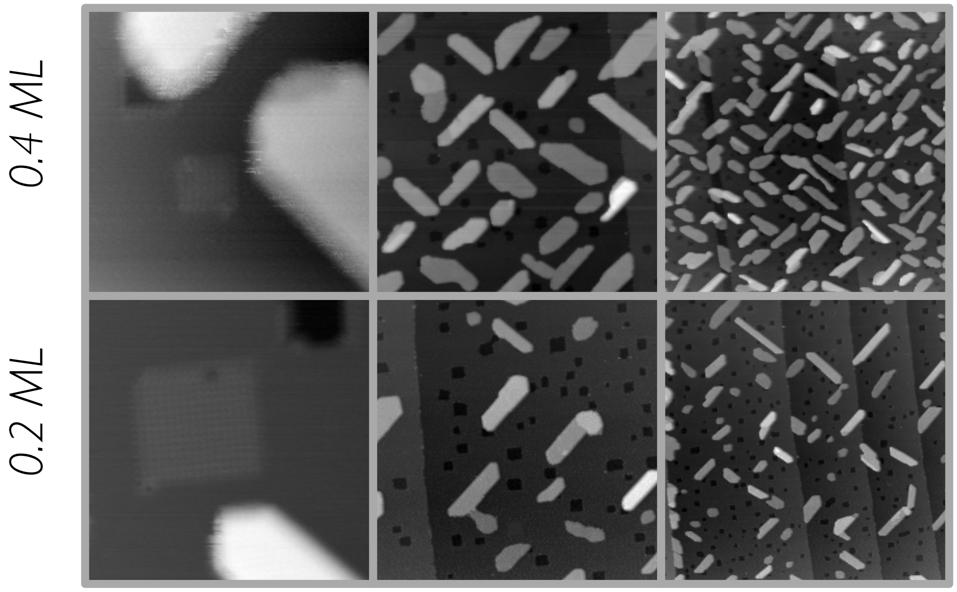

Figure 3.8: PTCDI deposited onto pit-templated NaCl for two different coverages. (Left column) 40 × 40 nm, (middle column) 300 × 300 nm, (right column) 600 × 600 nm NC-AFM images

when gold nanoclusters are present, atomic resolution was not obtained for the gold templated sample. However, based on the molecular resolution visible in Fig.3.9(c), it is reasonable to assume the bulk-like crystalline structure for needle islands grown on gold templated samples, similar to the needle-shaped islands observed for other surface preparations.

The epitaxy of all PTCDI structures observed herein are shown in Fig.3.10. Pit-trapped islands have the same structure as the metastable square-shaped islands observed previously on unaltered NaCl. Both form single monolayer (2×2) brick wall structures with all molecules in equivalent positions with respect to the NaCl substrate (Fig.3.10d and g), in contrast with the characteristic canted row structure observed in the needle-shaped islands (Fig.3.10e, f, h and i) and on a variety of other substrates [6–14]. The crystalline structures of the monolayer squ-

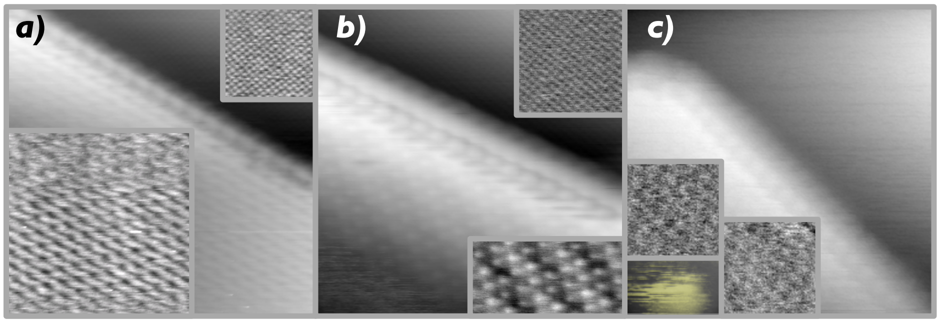

Figure 3.9: NC-AFM images of needle islands of PTCDI with insets flattened for enhanced contrast (a) on NaCl, 25 × 25 nm, (b) on KBr. 20 × 20 nm, and (c) on gold templated KBr, 20 × 20 nm, with gold nanocluster false colored for illustrative purposes.

are island and multilayer needle islands PTCDI on NaCl were discussed earlier in Chapter 2. All lattice constants are given in Table 3.2, determined from atomic and molecular resolution images and the well known lattice constants of NaCl and KBr.

Structure	b_1 (nm)	b_2 (nm)	θ (°)	β (°)
Needle (NaCl)	1.32 ± 0.03	1.65 ± 0.04	29 ± 1	90 ± 2
Needle (KBr)	1.42 ± 0.02	1.75 ± 0.05	29 ± 1	93 ± 3
Square (NaCl)	1.13 ± 0.04	1.09 ± 0.08	1 ± 3	93 ± 4
Pit (NaCl)	1.15 ± 0.04	1.14 ± 0.04	1 ± 1	88 ± 2
Preferred NaCl sites	1.13	1.13	0	90

Table 3.2: Needle, square and pit lattice constants

In both pit-trapped and square-shaped islands, the molecule-substrate interaction appears to influence growth sufficiently to hold a single monolayer of molecules to the preferred adsorption sites, the same sites preferred for PTCDA on NaCl calculated by Ji *et al.* [16, 61]. PTCDA molecules trapped in pits have been observed with a strained (2×4) herringbone-like structure and a variety of structural defects, which exhibit different optoelectronic properties depending on structure [98]. PTCDI molecules appear to fill pits more uniformly (defects have

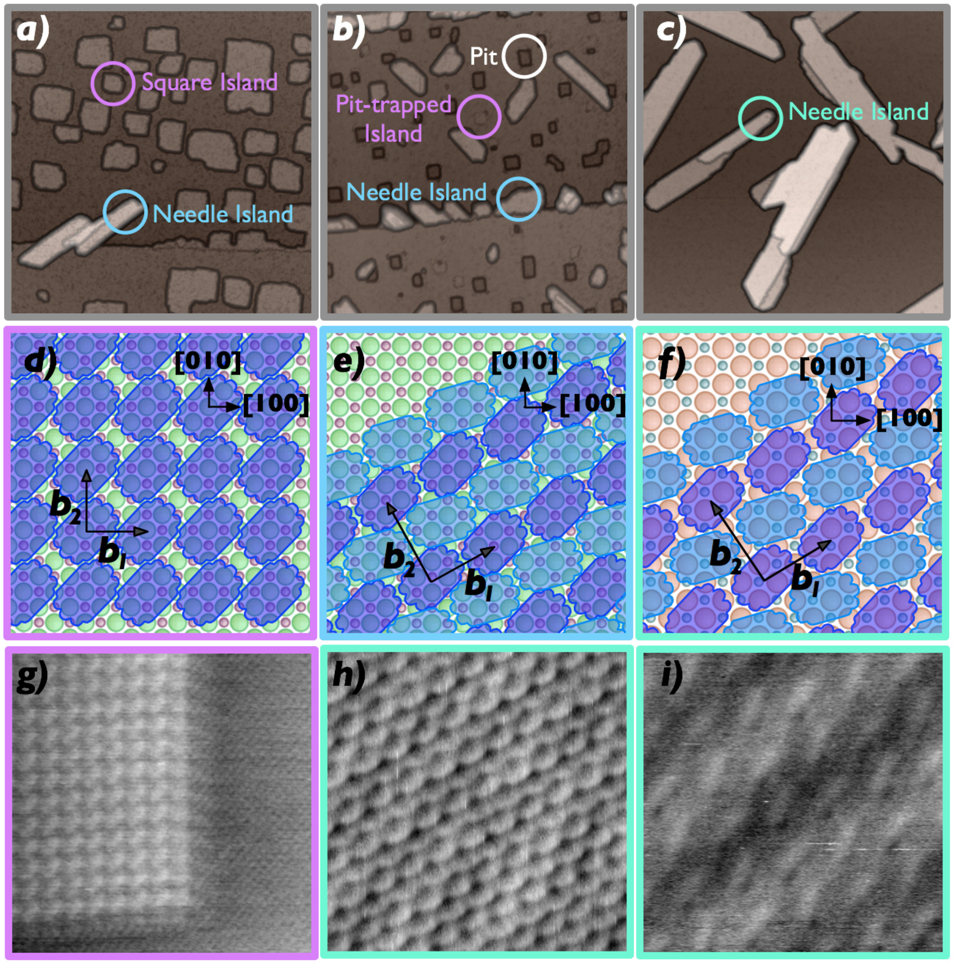

Figure 3.10: Epitaxy of PTCDI on NaCl and KBr. (Top row) 300 nm×300 nm images of (a and b) 0.2 ML deposited on flat and pit-templated NaCl, (c) 0.4 ML deposited on KBr, 3D-rendered to enhance pit visibility. Δf = -4.0, -2.2, -2.3 Hz; Γ = -0.6, -0.3, -0.3 fN$\sqrt{m}$ (Middle row) Illustrations of (d) (2×2) brick wall structure of both square island and pit-trapped molecules on NaCl, (e and f) needle island structure observed on NaCl and KBr respectively (top layer of molecules only shown for clarity). (Bottom row) (g) 15 nm×15 nm image of molecules trapped in a pit with surrounding NaCl lattice, (h and I) 10 nm×10 nm and 5 nm×5 nm images illustrating needle-island structure of PTCDI on KBr. Δf = -6.0, -14.8, -17.4 Hz; Γ = -0.8, -2.1, -2.5 fN$\sqrt{m}$

only been observed in corners) and should therefore produce a narrower range of electronic properties.

Although pit-trapped islands and square-shaped islands in the middle of terraces have the same structure, pit-trapped structures are probed more easily, which we attribute to the added stability arising from the pit edges [95, 97]. The pit edges likely offer an additional edge-molecule interaction that strengthens the molecule-surface interaction, giving rise to higher diffusion and dewetting barriers (the dewetting barrier is the energetic barrier arising from the change in PTCDI configuration during the transition from the square island structure to the needle island structure). The brick wall structured islands are less stable than the needle islands, but needle islands require a defect to nucleate and are pinned to the site [91]. Brick wall structure filled pits have been observed as long as 10086 minutes (8 days) after deposition. A higher dewetting barrier may partially explain the long life of these filled pits - despite the presence of kink sites at pit corners, a higher dewetting barrier would delay the nucleation of needle islands. It is possible to disturb square islands by imaging with a frequency shift on the order of -10 Hz (corresponding to a normalized frequency shift of $\sim$ -1.4 fN$\sqrt{m}$), pit-trapped structures may be disrupted by imaging with frequency shifts in excess of -25 Hz, while needle islands are stable in excess of -30 Hz (corresponding normalized frequency shifts of $\sim$ -3.5 and -4.3 fN$\sqrt{m}$ respectively). Comparatively, Kawai *et al.* observed cutting of meso-(4-cyanophenyl)-substituted Zn(II) porphyrin molecular wires self-assembled on KBr(001) (nucleated from step edges and gold nanoclusters) at -3.6 fN$\sqrt{m}$, and noted that the molecules were weakly bound to both the substrate and the rest of the wire [119].

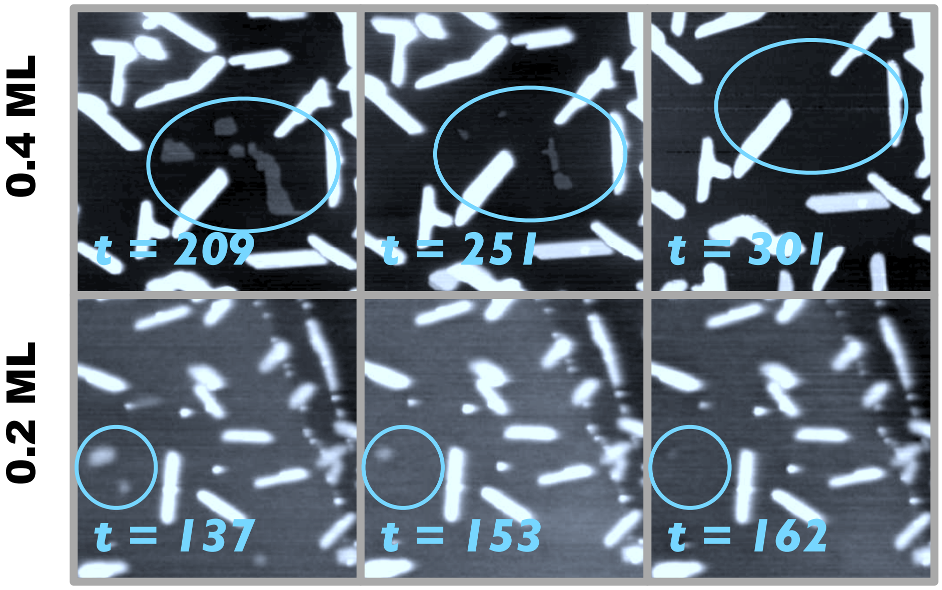

Figure 3.11: 300 nm×300 nm images illustrating dewetting for two PTCDI coverages on gold-templated NaCl, with square-shaped islands disappearing in circles (elapsed time since deposition given in minutes, z-scale contrast altered to make square islands visible). Δf = (top row) -2.0, -2.5, -4.6 (bottom row) all -1.5 Hz; Γ = -0.3, -0.3, -0.6 and -0.2 fN$\sqrt{m}$

3.4.4 Gold

Gold nanoclusters tend to decorate steps in the NaCl, although some still form in the middle of terraces, similar to gold deposited on KBr [100–103, 119, 120]. Like the pits, gold clusters also act as nucleation sites for needle islands and dewetting is completed relatively quickly, within about 5 hours (see Fig.3.11). Resulting islands tend to be similar in length to those formed by the same coverage of PTCDI on pit-templated NaCl, but are ∼15% narrower and nearly twice as tall, as can be seen in Fig.3.3 and Fig.3.7.

The affinity of PTCDI to nucleate from gold promotes it as a promising electrical contact material for organic electronics. Because the gold nanoclusters are not quasi-2 dimensional like the pits (and steps), the islands on gold-templated samples may be modulated by the dimensions of the gold clusters, which are generally taller and narrower than pits. PTCDI molecules typically extend from both sides of the gold, with the gold nanocluster in the middle of the needle-shaped island, in contrast to cyanoporphyrin wires grown on Au decorated KBr observed by the group of Glatzel and Kawai *et al.* [103, 119]. The gold seems to decrease the tendency of needle islands to grow in width, promoting interlayer mass transport and the formation of upper layers. Zhong *et al.* modelled the efficient ascending interlayer transport of oligoethylene-bridged diferrocene molecules on Ag(110), which form mesalike islands in what they describe as a strain-driven ascending process, preferentially attaching to upper unstrained layers with higher effective binding energies than strained layers close to the substrate [83].

3.4.5 Pits + Gold

Combining the two templating methods is a promising means of creating controlled nanoscale hybrid molecule-metal structures [102], and also results in a more homogeneous surface distribution of gold nanoclusters over the surface. Pits were created initially, followed by deposition of 0.05 nm of gold and then 0.4 ML of PTCDI, similar to previous experiments done by Mativetsky *et al.* with PTCDA molecules deposited on KBr [102]. The resulting film exhibited rapid dewetting, which was complete within an hour, and had intermediate needle island dimensions given in Fig.3.3. Fig.3.12 gives a detailed view of PTCDI grown on a NaCl sample templated with pits and 0.05 nm of gold. The AFM tip tends to pick up gold nanoclusters at normalized frequency shifts above $\sim$-0.4 fN$\sqrt{m}$, making high-resolution imaging difficult. In contrast to the pit-templated samples, no single layer pit-trapped islands were observed. However, like the pit templated samples, there are a larger proportion of small multilayer islands with the needle island structure confined to pits, such as the one indicated by the arrow in Fig.3.12.

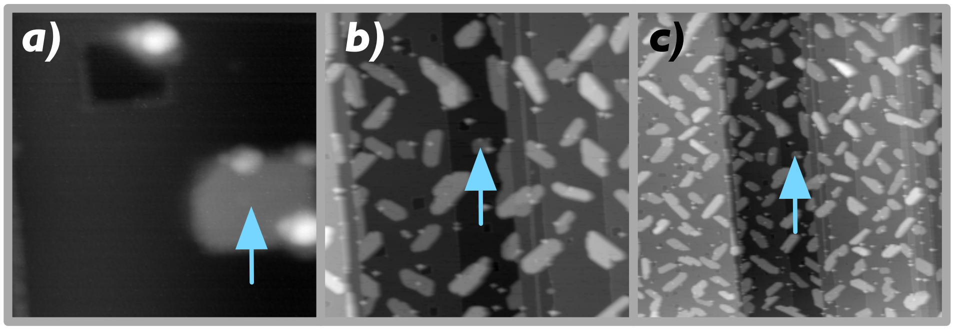

Figure 3.12: 0.4 ML PTCDI deposited onto pit and gold templated NaCl. (Left) 40 x 40 nm, (middle) 300 × 300 nm, (right) 600 × 600 nm NC-AFM images

3.5 Nucleation Site Growth Dependence

3.5.1 Comparison of Morphologies

In general, templated surfaces contain more nucleation sites than unaltered surfaces, and can produce many small needle-shaped islands close together (presuming negligible Ostwald ripening, see Fig.3.3). The dimensions of needle-shaped islands also depend on the coverage of molecules deposited. More molecules for the same surface preparation generally results in larger islands (this is true only if the nucleation site surface distribution is kept constant. A higher step density produces smaller islands in the top left image of Fig.3.7). Unaltered NaCl and KBr are easily cleaved to produce atomically flat terraces on the order of microns in size, resulting in fewer nucleation sites and therefore larger, more spread out needle islands. PTCDI islands grown on unaltered substrates tend to be about three times the length and an order of magnitude larger in volume than those of the same coverage grown on templated substrates. The size of the needle-shaped islands produced in a film depends on the density of nucleation sites, and the lack of control over the positioning of step edges of alkali-halide surfaces results in a large variation of molecular island size (standard deviation of $\sim$50% in volume) and surface distribution (double step edges are densely decorated) when grown on unaltered substrates. Also, islands grown on gold-templated NaCl substrates tend to be about twice the height and $\sim$15% narrower than those grown on pit-templated substrates for the same coverage of molecules deposited. While the reason for this difference in geometry is not well understood, it appears that the islands are modulated by the dimensions of the gold clusters.

3.5.2 Contaminants as Nucleation Sites

It should be noted that while this study includes samples prepared exclusively under UHV, the environment is expected to play a crucial role in film structure. Contaminants may act as nucleation sites, diffusion barriers, surfactants, strain reducers, and create defects. Atomic steps and kink sites are well known as traps for contaminants [24–26] due to their lower coordination numbers, which may in turn nucleate needle island growth [66] and suppress the formation of metastable structures.

3.6 Molecular Behaviour

3.6.1 Diffusion

By providing more nucleation sites, it is possible to create a higher surface density of smaller islands, but one must also consider the dynamics of the growth process. PTCDI molecules are capable of diffusing long distances (on the order of hundreds of nanometers) before binding to a stable site (see for eg. Fig.3.5 and Fig.3.7) as films evolve over the course of days at room temperature, and at elevated temperatures may travel even farther and over higher energy barriers (such as steps). The relatively low diffusion barriers for single PTCDI molecules diffusing between adjacent preferred adsorption sites on NaCl at room temperature have been calculated using density functional theory (by Wei Ji, see supplementary information of [82] for details) to be 0.41 eV and 0.27 eV along and perpendicular to the long molecular axis respectively. Diffusion barriers and travel distances play an important role in the resulting film morphology [91]. In the dewetting scenario, needle-shaped islands are populated by molecules escaping from the surrounding metastable square-shaped islands. Even with negligible Ostwald ripening between needle-shaped islands, there is competition for the capture of free molecules diffusing from the square-shaped islands. If more needle-shaped islands nucleate, diffusing molecules travel smaller distances before being trapped, resulting in faster dewetting, smaller needle-shaped islands and a more homogenous distribution of islands over the surface. Smaller molecule travel distances require shorter transit time, thus templated substrates produce stable films within a matter of hours instead of days at room temperature.

3.6.2 Anisotropic Growth

We speculate that a diffusing molecule incident on the side of a needle island may hop along the side of an unfavourable edge until it reaches a location with sufficient stability to attach, similar to adatom behaviour in the atomistic compact island growth regime [26]. Given the tendency of PTCDI molecules to join end-to-end [12, 91], needle islands tend to elongate with time. This behaviour is akin to the more pronounced anisotropic growth of wirelike islands of DiMe-PTCDI on KBr and NaCl (001) [15], and exploited by Kawai *et al.* for "self-healing" meso-(4-cyanophenyl)-substituted Zn(II) porphyrin molecular wires [119]. The end-to-end intermolecular interaction is due to the hydrogen bonding between N-H and C=O groups, so growth occurs preferentially from the ends of islands as existing rows tend to elongate over the formation of new adjacent rows.

3.6.3 Suppression

If a PTCDI needle island extends during growth towards an adjacent island with a different orientation (as may be the case more frequently for higher coverages), the islands may coalesce, or if coalescence is unfavourable, the growth in this direction may be suppressed (see Fig.3.5 and Appendix A). If suppressed, molecules diffusing along the island sides with insufficient coordination to attach would be unable to further elongate the island in that direction, and may continue to diffuse until eventually either reaching a different favourable location or being joined by other molecules to form a new row and thus widen the island. Such suppression may occur more frequently for samples with high nucleation site density and relatively short island heights at a given coverage, such as the pit-templated case in Fig.3.7. In such instances, the surface area covered by islands may be sufficiently high that island dimensions are not dictated by competitive dewetting and substrate structure alone, and suppression may arise where many needle-shaped islands with differing orientations grow in close proximity to one another. This suppression is exemplified in Fig.3.13, showing two subsequent 1 ML depositions of PTCDI on KBr. After the second deposition, the closely packed needle-shaped

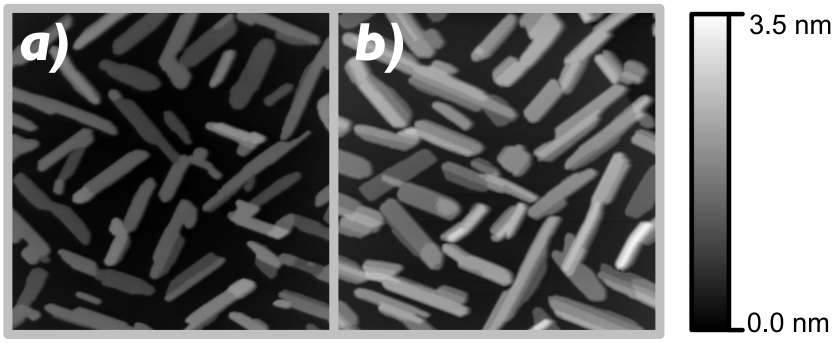

Figure 3.13: 600 nm×600 nm images of subsequent depositions of PTCDI on KBr, illustrating suppression (a) 1 ML, average island height 1.1 ± 0.2, Δf = -2.0 Hz; Γ = -0.3 $fN\sqrt{m}$ and (b) 2 ML, average island height 1.7 ± 0.5 nm Δf = -2.9 Hz; Γ = -0.4 $fN\sqrt{m}$

islands maintain similar island surface distributions due to suppression, and increase from 1.1 ± 0.2 nm to 1.7 ± 0.5 in average height (partial coalescence creates ambiguity in determining other island dimensions). This procedure is akin to templating in that the island surface distribution is set by an initial deposition, but in this case, existing island edges generally act as the most stable binding site for additional molecules, providing another means of tailoring the resulting thin film morphology.

3.7 Summary

Growth conditions and surface structuring can provide a means of control over organic thin film morphology, which should lead to controllable device relevant properties. The electronic properties of molecular islands are determined by structure, and are key to the performance of potential molecular devices. For example, needle-shaped and square-shaped islands should offer different charge carrier mobilities owing to the different intermolecular orientations resulting in different wavefunction overlap. Defects and grain boundaries may lead to a change in the resistivity of islands and thin films. The influence of experimental factors on the morphology of PTCDI thin films was investigated, and parameters were identified that may be varied to induce desired behaviour and produce tailored film morphologies. Two methods of increasing stable needle island size were explored. Two-step depositions can be used to increase the average needle island size without changing the distribution of islands on the surface, producing a more dense island surface distribution than is accessible by a single deposition. Heat can be applied either during molecule deposition or afterwards (annealing) to increase the kinetic energy of molecules and enhance ripening, producing larger islands distributed more sparsely over the surface. Deposition onto cooled substrates was also attempted, as detailed in Appendix B, and met with limited success. Defects act as island nucleation sites and play a crucial role in determining film structure. Templating a surface with monolayer deep pits or gold nanoclusters can increase the nucleation site density and tailor the size, shape, surface distribution, and dewetting time of needle-shaped PTCDI islands nucleated on NaCl. To gain a microscopic picture of how these "tuning knobs" influence large anisotropic molecules on surfaces, there is a need for comparative modeling, such as within a kinetic Monte Carlo framework [83–85]. However, the experiments shown here demonstrate some of the methods that can be applied to modify the final stable film morphology including and even exploiting the effects of dewetting. The ability to control molecular film morphology through substrate modification, especially where dewetting occurs, is a general concept and may prove useful in the context of dialling in thin film properties for devices.

4

Organic Photovoltaics

4.1 Principles and Challenges

Film morphology of organic photovoltaics (OPVs) has a dramatic influence on device performance [23, 121]. The degree and homogeneity of donor and acceptor mixing is critically important for the formation of heterojunctions. The active layer structure can influence exciton and charge carrier mobilities, as will be discussed in detail below. Defects, interfaces and regions of differing crystallinity play assorted roles in the various stages of charge carrier generation and transportation [122]. Rough interfaces and the presence of voids can increase the series resistance and also the chance of device short circuiting. The presence of even small amounts of impurities can drastically decrease device performance [123]. As a result, many devices are oxygen and water sensitive [124], and OPV lifetimes rarely exceed a few years [125]. However, the detailed mechanisms by which these many factors impede device performance are largely unknown. To date, the structure-function relationship of organic films is poorly understood, and remains one of the outstanding challenges to improving device performance [124, 126, 127].

It is perhaps surprising, then, that most state of the art OPV active materials are designed to look something like scaled down versions of spaghetti with meatballs (typically long polymer chains blended with fullerenes, see Fig.4.1) [128–130].

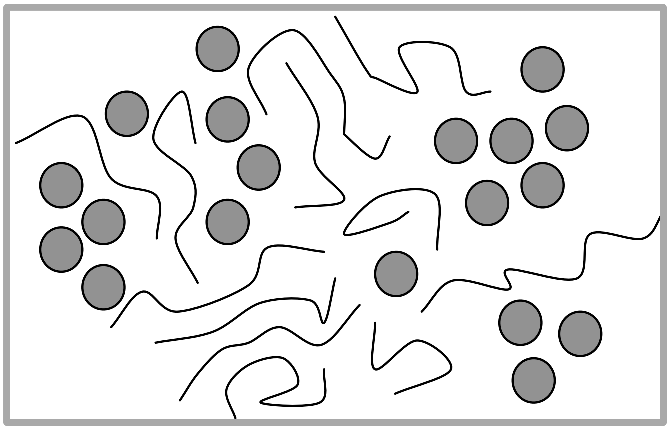

Figure 4.1: A typical illustration representing the OPV active layer, containing conjugated polymers (represented by curved lines) and fullerene derivatives such as PCBM (represented by grey circles)

They may contain a variety of conjugated polymers, macromolecules, nanocrystals, fullerenes and other small molecules, and are typically solution deposited in ambient conditions (see review articles [131–133] and references therein). Characterization methods applied to solar cell materials (and relatedly organic thin film transistor, light emitting diode, and other organic optoelectronic device materials) are predominantly ensemble techniques that measure optical (absorption, photoluminescence) and optoelectronic (current/photocurrent, voltage/photovoltage and derivate properties such as power conversion, current density and external quantum efficiency) device properties. The film morphology may be characterized by x-ray diffraction, TEM [128, 134] and/or ambient AFM, but the nanoscale morphology is generally an unknown combination of amorphous, crystalline and interfacial regions [23].

Thus, it seems appropriate and timely to explore the nanoscale morphology and optoelectronic properties of clean, well defined OPV molecular thin films deposited under UHV with NC-AFM and KPFM. Building upon our previous morphological studies of tailoring molecular island size and nucleation site distribution described in Chapters 2 and 3, this chapter presents preliminary studies of molecular electron donor and electron acceptor thin films. We simultaneously observe the surface topography with NC-AFM and local contact potential difference (LCPD) distribution with KPFM to investigate the structure-function relationship in OPVs. We illuminate samples and explore changes in LCPD with the hopes of shedding light on fundamental processes of photovoltaic energy generation.

4.1.1 Harvesting Light with Molecules

Organic photovoltaic devices use molecules as active light harvesting materials instead of the more common and well developed inorganic semiconductors, and are very promising in terms of fabrication costs and materials safety [135,136]. However, they propose an additional challenge: when light is absorbed, bound pairs of electrons and holes called *excitons* are formed instead of the free electrons and holes created in inorganic solar materials. An effective solar cell must capture light efficiently and must also be able to convert it into a collectable current to produce a net power output. In order to collect a current of these bound charge carriers, excitons must dissociate and separate so that an external electric field can sweep the electrons and holes in opposite directions towards electrodes. This is typically accomplished through the use of molecular heterojunctions, located within the active regions of heterojunction solar cell devices [59,130,135].

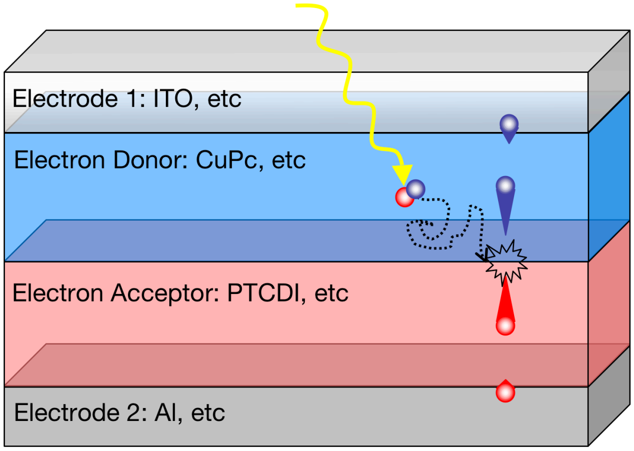

Figure 4.2: Basic bilayer heterojunction organic solar cell, illustrating light absorption, exciton formation, exciton diffusion, exciton dissociation across the heterojunction, free charge carrier diffusion and collection at the electrodes

4.1.2 Heterojunction Devices

The basic bilayer heterojunction organic solar cell is illustrated in Fig.4.2. It is comprised of two active layers: the electron donor layer and the electron acceptor layer. These layers are typically composed of amorphous, polycrystalline or partially crystalline polymer materials that are solution processed and may be heat treated or doped to improve device performance. Bulk heterojunction devices (BHJs) operate in the same way as bilayer devices, but the active molecular layers are interpenetrating or mixed to produce a larger donor-acceptor interface area. If the mixing is heterogeneous (containing regions of pure donor and acceptor molecules) it is referred to as a dispersed heterojunction device. If mixing is homogeneous it is called a blended heterojunction device (though the distinction between dispersed and blended is blurred for small domains as illustrated in Fig.4.1).

Light harvesting with an OPV heterojunction device involves six consecutive processes [59, 130, 135] (the first five of which are illustrated in Fig.4.2):

1. *Light absorption:* Light is absorbed by an organic material to produce an exciton (a bound electron and hole pair, discussed in detail below)
2. *Exciton diffusion:* The exciton diffuses randomly through the material during its lifetime (further discussed below). Typical diffusion lengths of excitons in organic materials are on the order of 10-20 nm [59,130,137]
3. *Exciton dissociation:* Excitons separate into free charge carriers at the donor-acceptor interface (or recombine via several loss mechanisms)
4. *Free charge carrier transport:* The dissociated electrons and holes move apart in the presence of an external electric field, typically produced by materials with different work functions at the electrodes
5. *Collection:* The charge carriers are collected by the electrodes if a current path exists (or are trapped until they recombine). Grain boundaries and defects may hinder charge collection
6. *Driving external load:* The resulting current can drive an external load. Solar cell devices operate similarly to electrochemical cells, except that charge carriers are created by photon absorption and never need to be replenished. Therefore, solar cells allow energy harvesting whereas electrochemical cells allow energy storage (electrodes deplete and must be recharged)

4.1.3 Excitons

The formation of bound excitons is the key difference between silicon and organic photovoltaics [124,138], and the study of excitons represents an important aim of this research. This section presents the background information needed to recognize the goals of studying OPVs with NC-AFM and KPFM.

In inorganic semiconducting solar cells, the dielectric constant is typically large (on the order of ε = 10 [139]) and polarization of the materials provides screening between an excited electron and the associated hole such that they cannot "see" one another through coulomb attraction, and are swept apart by the inherent electric field across a pn-junction. Free charge carriers are produced almost immediately upon excitation, as the energy needed to separate the electron and hole is below $\sim k_BT$. However, organic materials typically have lower dielectric constants (on the order of ε = 3 [124, 140]) so electrons and holes generally cannot escape one another's coulomb attraction upon excitation. Rather, they remain bound in a slightly lower energy configuration than free charge carriers (illustrated in Fig.4.3). The resulting quasiparticle is called an exciton.

Excitons come in a variety of flavours that can be classified according to electronic and vibrational excitation energies and spatial extent [140, 142]. Some excitons can be unbound at electron donor-acceptor interfaces (heterojunctions), producing free electrons and holes that may generate current [143]. Others act as loss mechanisms that decrease device efficiency. The basic OPV excitation phenomena are illustrated in Fig.4.3. *Frenkel excitons* (named after Yakov Frenkel) are closely bound electron-hole pairs with a spatial extent of around that of the crystalline unit cell (i.e. confined to one or a few molecules) with relatively flat highest occupied molecular orbital (HOMO) and lowest unoccupied molecular orbital (LUMO) dispersions [144]. *Wannier-Mott excitons* (named after Gregory Wannier and Nevill Mott) are more weakly bound due to screening and therefore more delocalized, with semiconductor band dispersion features spanning across more than one unit cell [145]. *Charge-transfer excitons* occur across material interfaces [140], such as when an excited electron transfers from the electron donor

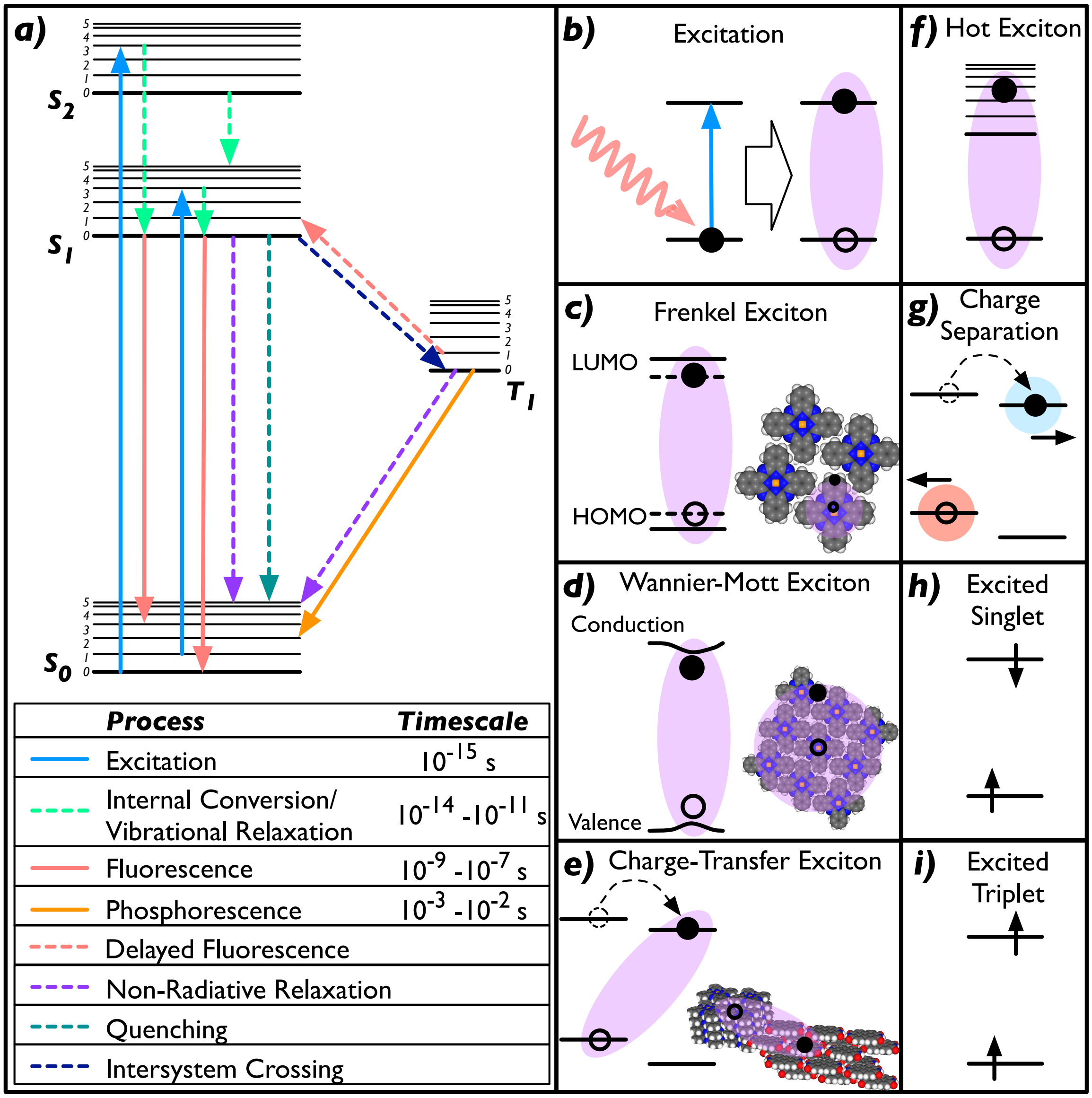

Figure 4.3: Excitation processes: (a) Jablonski diagram of absorption and relaxation processes with ground state S_0, first and second excited singlet states S_1 and S_2 and first excited triplet state T_1. Fine lines represent vibrational energy states, and approximate timescales are given, based on [141]. (b) Excitation by photon absorption. (c) Frenkel exciton, tightly bound. (d) Wannier-Mott exciton, delocalized. (e) Charge-transfer exciton, straddling the donor-acceptor interface. (f) Hot exciton, electron in higher lying energy states that disputably may facilitate dissociation/diffusion. (g) Charge separation, electron and hole escape one another's Coulomb attraction. (h and i) Schematic representation of Pauli exclusion in excited singlet and triplet states of paired electrons.

material to the electron acceptor (or conversely, when a hole transfers from the electron acceptor to the donor) and the charges remain coulombically bound, with an energy slightly lower than that of the band gap. Such states can be energetically favourable and long lived, and act as a loss mechanism in OPVs. Associated polarons are discussed below. *Hot excitons* are a hot topic at present, as there is dispute over whether or not excitons with additional vibrational energy can facilitate efficient charge carrier separation across the donor-acceptor heterojunction [140, 146, 147].

The screening of a charge in a dielectric material is caused by polarization of the material immediately surrounding it. The combination of the charge and the polarization field surrounding it is called a *polaron*. The surrounding material may also spatially distort to produce phonons (lattice vibrations). Significant spatial distortion or conformational changes may be visible in high-resolution NC-AFM if sufficiently long-lived and frequently recurring to produce a change in cantilever frequency shift. Excitons are charge-neutral and hydrogen-like, but if they are spatially delocalized and segregated, such as in a charge-transfer exciton, they will have a dipole moment. The combination of charge and distortion field surrounding these two bound charges is called a *geminate polaron pair*, and are probed and identified by a variety of optical techniques [140, 143]. Geminate polaron pairs straddling heterojunctions may be visible in KPFM and high-resolution NC-AFM as a change in LCPD and structure of molecules near the interface upon illumination.

Singlet states have typical lifetimes on the order of nanoseconds, while triplets can have decay times from microsceconds to seconds [148]. *Triplet* states are formed by internal conversion (the excited electron spin flips from up to down, or vice versa), and are long lived because they cannot recombine directly (forbidden by the Pauli exclusion principle). The T1 triplet state is usually energetically lower than the S1 first excited singlet state, and can act as a loss mechanism in OPVs by trapping excitons that might otherwise have separated and generated charge. Small hydrocarbon molecules (such as PTCDI) have negligible spin-orbit coupling from singlet to triplet states, but systems with heavy atoms (such as metals, for example those in metal phthalocyanines) can have efficient intersystem crossing [141]. Illumination has been observed to induce LCPD changes on PTCDA due to the presence of excited states that lower the effective work function by KPFM [98].The lifetimes of trap states suggest that we may be able image an ensemble average of excited states as well as spatially delocalized polarons created under sample illumination with KPFM and high-resolution NC-AFM.

Exciton Diffusion

The *exciton diffusion length* describes how far a typical exciton diffuses through a material before recombination. This value determines the active layer thickness of OPV material surrounding the donor-acceptor heterojunction, and is therefore an important value for engineering efficient solar cells. Excitons generated more than a diffusion length from a heterojunction will usually recombine before dissociating and are therefore wasted. The characteristic exciton diffusion length, L_D, is defined as [149]:

$$L_D = \sqrt{D\tau_0}, \tag{4.1}$$

where D is the exciton diffusion coefficient and τ_0 is the decay time constant.

Exciton diffusion lengths in materials are determined by a variety of ensemble measurements such as time-resolved photoluminescence measurements of luminescence quenching, device photocurrent/photovoltaic response measurements as a function of layer thickness [137,149], and flash-photolysis time-resolved microwave conductivity measurements of incident photon charge separation efficiency fit with analytical expressions [150]. Such measurements are typically performed on spin-coated films of "known" thickness (usually calibrated with a step-profiler and adjusted by varying solution concentration, not necessarily verified for each film produced [150]). These measurements always assume isotropy and generally ignore crystalline structure altogether, which is probably a poor assumption given the anisotropic nature of most molecular structures. The anisotropic energy transport of Frenkel excitonic polarons (multi-particle systems of an exciton surrounded by vibronic excitations) in polymer H- and J- aggregates has received some recent theoretical attention [142], but currently lacks experimental support.

Exciton diffusion lengths of OPV materials reported in the literature are widely varying, anywhere from a few to several tens of nanometres (but may often be overestimated due to interpenetration of materials [149]), and are generally expected to be on the order of 10-20 nm [59, 130, 137, 150]. Molecules relevant to this thesis exemplify the typical variation in reported values. The exciton diffusion length of CuPc was measured to be 68 ± 20 nm from photocurrent spectra by fitting external quantum efficiency versus wavelength of a test device by Stubinger *et al.* [151], while Peumans *et al.* estimated it to be 10 ± 3 nm [137] and Terao *et al.* estimated it to be 15.4 nm [56], all by the same method. Yang *et al.* give a range of CuPc exciton diffusion length values: ∼10-50 nm [59], and it was modelled by Xue *et al.* as 8 nm [152]. Similarly, although the exciton diffusion length of PTCDI is not well studied (at least not in the absence of large side chains), the exciton diffusion length of PTCBI (perylene-3,4,9,10-tetracarboxyl-bis-benzimidazole, a perylene derivative similar to PTCDI) was modelled by Xue *et al.* as 3 nm [152] and measured to be 3.0 ± 0.3 nm by photoluminescence quenching by Peumans *et al.* [137]. However, Peumans *et al.* also determined the exciton diffusion length of PTCDA (previously discussed as very similar to PTCDI) to be 88.0 ± 6.0 nm by fitting external quantum efficiency of a device versus wavelength (the same method as for CuPc) [137]. Clearly the exciton diffusion lengths of CuPc and PTCDI are not known precisely, and the literature values provide a rough estimation.

Exciton Dissociation

Exciton dissociation into free charge carriers is known to occur across the donor-acceptor interface, and is thought to be very fast (for example, ∼40-45 fs for a polymer-fullerene device, though there is some debate on the timescale for truly mobile charge creation [153]) and efficient (approaching 100 %) [124,137,154]. However, the detailed mechanism(s) by which excitons dissociate is still unknown. As mentioned above, the topic of hot excitons is still controversial as to whether or not they may aid in charge carrier separation [140,146,147]. The nanoscale molecular structure of the donor-acceptor interface should play an important role, as molecular orbital overlap depends on the proximity and orientation of molecules with respect to one another. Studies of single molecules that incorporate a linked electron donor side and electron acceptor side provide a controlled means of studying very local excitation [155], but functional OPV processes generally extend over larger spatial volumes and depend on the ensemble properties of molecular structures as well as those of the individual component molecules. A high resolution approach to observing heterojunctions between well defined organic crystal thin film structures (such as by combined NC-AFM and KPFM) may prove instrumental in elucidating the details of exciton dissociation.

4.1.4 Charge Carrier Transport and Collection

After exciton dissociation, the resulting charge carriers move in opposite directions (in the presence of an electric field) towards the electrodes. In bilayer devices this process is relatively simple, as holes move through the electron donor material and electrons move through the electron acceptor. This offset in charge may be visible by KPFM (discussed below). In bulk heterojunction devices this process can be more complicated, depending on the degree of mixing and available transport pathways to the charge carriers. It is worth noting that the post-dissociation description of electrons and holes as "free charge carriers" is not strictly accurate, particularly in relatively soft organic materials, where lattice disruption and corresponding quasiparticles should be considered, but we will keep this nomenclature for simplicity.

The current density, J, for both negative and positive charge carriers in a PV device is given by a sum of drift and diffusion components as follows [124]:

$$\vec{J} = q\mu\rho\vec{E} + qD\vec{\nabla}\rho, \tag{4.2}$$

where q is the elementary charge, μ is the charge carrier mobility (of either electrons or holes), ρ is the charge density (of either electrons or holes), $\vec{E}$ is the electric field across the layer, and D is the diffusion coefficient (of either electrons or holes).

Charge carrier mobility is another important parameter for solar cell device engineering, as it also impacts optimal device layer thickness and material choice. It is a difficult quantity to measure directly due to influences from grain boundaries, defects, and electrical contacts (where present). In organic materials, charge carrier mobilities are determined (or estimated) by a wide variety of methods including time-of flight, field-effect transistor, diode configuration, xerographic discharge, surface acousto-electric traveling wave and pulse-radiolysis time-resolved microwave conductivity, among others (see review articles [156, 157] and references therein). Thin film transistor methods are very common but may not be an appropriate approach to studying charge transfer in OPVs due to compounding factors such as the lack of control and wide variety of values typically observed [158]. The electron diffusion length in GaP has been determined by KPFM [159], and this method could be applied to OPV materials if sample quality and measurement resolution allow it. Electron and hole mobilities in organic semiconductors can be strongly temperature dependent (due to the temperature dependence of their masses, which may approach the free electron mass at low temperature) [156, 158]. Hole mobility in electron donor conducting polymers is typically found to be lower than the electron mobility in organic electron acceptors [124]. Again molecular anisotropy should be considered as charge carrier mobility may differ along different crystalline directions, but it is generally ignored.

4.1.5 KPFM for OPVs

KPFM has recently been applied as a characterization technique for OPVs (notably within the last ∼six years [126,127,160–162]), and represents a major topic in the new International Workshop on Scanning Probe Microscopy for Energy Applications started in 2010. KPFM contrast has been observed between organic donor and acceptor regions in what are typically solution cast, partially crystalline, partially amorphous films. This contrast may be used for species and agglomerate identification, and may change under sample illumination [126,127,160–162]. Thin films of CuPc deposited on Si(100) and ITO substrates (prepared *ex-situ*) were explored with KPFM under UHV by Sadewasser *et al.* [49], and demonstrated a change in contrast when illuminated with light below ∼800nm due to hole transfer into the substrates. To date, no high-resolution UHV KPFM studies of OPV donor-acceptor molecules are published (image sizes are typically on the order of $1 \times 1\ \mu$m), and the work presented here is among the highest quality obtained so far.

It is worth noting that the KPFM bias modulation frequency must be kept below the reciprocal of the dielectric relaxation time constants of the tip and sample materials involved in order to avoid transient, frequency dependent internal electric fields to provide an accurate measure of surface contact potential minima. The dielectric relaxation time constant is given by [51,163]:

$$\tau = \frac{\varepsilon}{\sigma}, \tag{4.3}$$

where ε is the dielectric constant (or permittivity) and σ is the material conductivity that may be calculated according to:

$$\sigma = \frac{J}{E}, \tag{4.4}$$

where J is the current density through a material and E is the electric field across it. There are a variety of dielectric relaxation processes that may contribute to the total internal electric field in a material, including (roughly in order of increasing time constant) dipolar (molecular rotation), ionic (or atomic), and electronic polarization [164]. Thus, the polarization response of materials (and subsequently the dielectric constant) may also vary as a function of electric field oscillation frequency to reflect several relaxation time constants, and can be particularly important in optical measurements. It may also depend on geometric properties [165]. In our case, we simply wish to modulate our tip-sample bias below the slowest dielectric relaxation time constant of the materials between them.

The dielectric relaxation time constant of silicon is very fast, on the order of 0.5 ps [51], corresponding to a characteristic frequency of 2 THz. El-Nahass *et al.* found dielectric relaxation times on the order of $\tau \simeq 10$ ps and 1 μs for Si and ZnPc respectively [166], corresponding to frequencies of $f \simeq 100$ GHz and 1 MHz. James *et al.* used spectroscopic measurements of MoOPc (molybdenum phthalocyanine) on ITO glass and the Cole-Cole model to find a mean dielectric relaxation time of 942 μs [167], corresponding to a frequency of 1.06 kHz and Thurzo *et al.* measured a dielectric relaxation time constant that they attribute to the bulk of the CuPc layer in a Ag/CuPc/ITO device of $\tau \simeq 100$ μs [168], corresponding to a frequency of $f \simeq$ 1600 Hz. For a detailed discussion of relaxation processes in polymers, see [169] and for models applied to OPV materials see [165]. Roughly assuming that the slowest dielectric relaxation time constant corresponding frequencies are at least in the kHz range, KPFM performed with an AC bias oscillation frequency of 800 Hz should allow real measurement of the LCPD on thin films of CuPc and PTCDI.

4.2 PTCDI and CuPc for OPVs

4.2.1 Sample Requirements

In order to study the nanoscale morphology of an organic heterojunction, an OPV sample must:

1. Form heterojunctions between regions of donor and acceptor molecules
2. Have relatively flat morphology accessible for imaging by NC-AFM (or other imaging techniques)
3. Have well defined film structure and be isolated electronically to avoid complications from other structures such as defects and traps

We therefore attempt to grow a well defined crystalline thin film of donor and acceptor molecules with isolated heterojunctions on an atomically flat insulating substrate, to be characterized by NC-AFM and KPFM.

4.2.2 Energy Level Considerations

The growth of PTCDI on alkali halides is now well characterized and controllable [82, 91]. As luck would have it, PTCDI is an electron acceptor molecule (though generally PTCDI derivatives with long functional groups are used in OPVs [170]), with an electron affinity of $\sim$3.9 eV (LUMO energy) and an ionization potential of $\sim$5.9 eV (HOMO energy) [171]. CuPc was selected as an accompanying donor molecule because it is a well studied small molecule widely used as an electron donor in OPV cells (as well as a hole-injection material in OLEDs) due to its efficient light absorption and high hole mobility [54, 172]. It has an electron affinity (LUMO energy) of $\sim$3.5 eV and an ionization potential (HOMO energy)

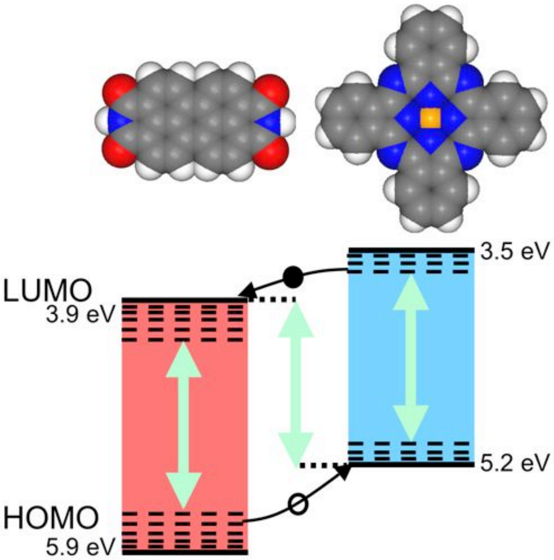

Figure 4.4: Energy level diagram for PTCDI (electron acceptor) and CuPc (electron donor) OPV heterojunction. Dashed lines indicate range of excitons with energies greater than the difference between CuPc HOMO and PTCDI LUMO (∼1.3 eV, indicated by green arrows), for which efficient charge separation is expected

of ∼5.2 eV [49, 173]. It also has high thermal and chemical stability, and can be thermally evaporated under UHV. The schematic energy level diagram for the resulting heterojunction illustrated in Fig.4.4 shows that PTCDI and CuPc are a reasonable donor-acceptor combination for OPV behaviour.

Efficient exciton dissociation is expected if the excitation energy is larger than the difference between the ionization potential of the donor and the electron affinity of the acceptor [137]. Thus, electrons from excitons produced in the CuPc will transfer to the PTCDI, and holes from excitons produced in the PTCDI will efficiently transfer to the CuPc if the exciton excitation energies exceed the difference between the CuPc ionization potential and the PTCDI electron affinity. The difference between the donor ionization potential (CuPc HOMO, ∼5.2 eV) and the acceptor electron affinity (PTCDI LUMO, ∼3.9 eV) is ∼1.3 eV.

Confusingly, HOMO and LUMO values reported in the literature (as well as ionization potential and electron affinity) can refer to both the *transport gap*, E_t (the energy needed to create molecular anions and cations, also the energy needed to produce free charge carriers) and more commonly, the *optical gap*, E_{gap}, which is determined by optical absorption and actually includes excitons and other relaxation energies (and is therefore more narrow) [174]. The excitation energy of an exciton is given by the transport gap minus the exciton binding energy (also called the charge separation energy) and any other relaxation energies. Exciton binding energies are typically 0.1 to 0.2 eV according to Peumans *et al.* [137] or 0.4 to 1.4 eV according to Hill *et al.* [174]. The HOMO-LUMO gaps of CuPc ($\sim$1.7 eV) and PTCDI ($\sim$2.0 eV) given here are optical, and therefore include absorption forming excitons. Thus, although charge transfer should be efficient for any excitons with energies greater than $\sim$1.3 eV (neglecting any band bending effects), dissociation will not necessarily result in the creation of free charge carriers, and lower energy charge transfer trap states may be formed instead.

4.2.3 Absorption

To provide a rough prediction of which wavelengths of light should excite each molecule, the thin film optical absorption spectra were estimated by averaging results from the literature [49, 86, 137, 175, 176], given in Fig.4.5. PTCDI absorbs strongly in the blue and green while CuPc absorbs strongly in the yellow, orange and red, conveniently allowing the two molecules to be probed semi-independently, and the resulting device to absorb across much of the solar spectrum. While photon absorption can result in a rich variety of processes (see Fig.4.3a), for these materials we may expect among them the formation of excitons needed

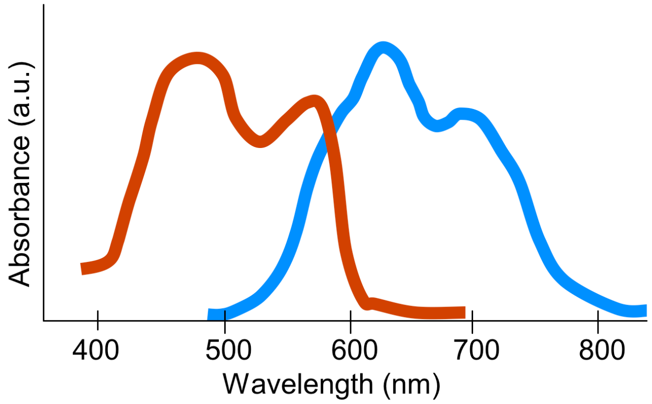

Figure 4.5: Estimated thin film absorbance for PTCDI (red curve) and CuPc (blue curve) (based on averaged literature results [49,86,137,175,176])

for OPV behaviour. For example, vibrationally dressed Frenkel type excitons are expected to form in PTCDI films with decay rates on the order of 3 ns [177].

4.3 Results

4.3.1 Growth

The molecules were thermally deposited, first CuPc (at ~350 °C) and then PTCDI (at 315 °C), onto room temperature KBr under UHV (as detailed in previous chapters). Both undergo Volmer-Weber growth to produce crystalline islands with no wetting layer. CuPc forms tall, mountainous islands along the KBr step edges. Initial depositions of CuPc produced islands so tall that NC-AFM imaging was very challenging (some of the few successful images shown in Fig.4.6). In attempt to reduce the CuPc island height, low coverages and multiple deposition steps were used in subsequent experiments (based on tailoring growth considerations discussed in Chapter 3 and [82]). Simultaneous molecular resolution on

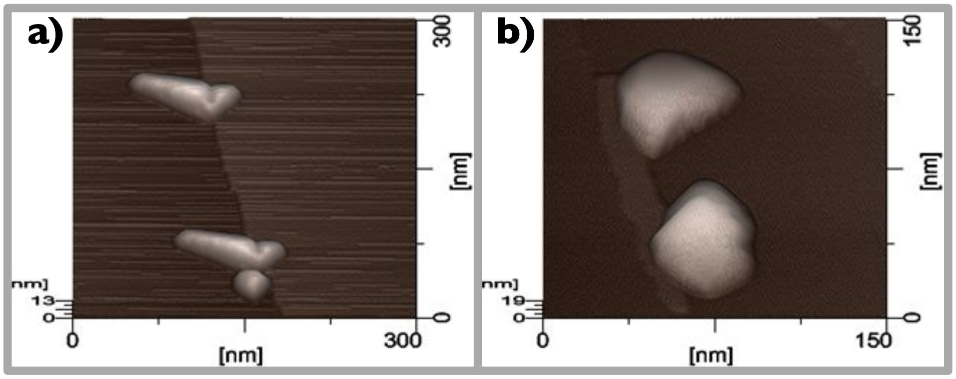

Figure 4.6: 3D rendered NC-AFM images of 0.3 ML CuPc deposited on KBr. Interestingly, the similar island shapes present in (a) are not the result of tip convolution

CuPc and atomic resolution on the underlying KBr is very difficult to achieve due to the height of CuPc islands. Thus, as of yet we are unable to determine the CuPc structure, but it is most likely one of the two well known phases (α-phase or β-phase) comprised of tilted planar stacks or columns of CuPc molecules [54]. PTCDI forms the familiar needle-shaped islands, with the same structure as in previous studies [82, 91], and the combined film of both molecules deposited on KBr is shown in Fig.4.7.

If PTCDI is deposited prior to CuPc, the CuPc appears to grow on top of the PTCDI islands, as shown in Fig.4.8. Although the interface structure cannot be determined by AFM, it appears to be a smooth, well contacted donor-acceptor interface. Efficiency losses are frequently attributed to interfacial defects and grain boundaries. This data, combined with the evidence of π orbital electron interaction between CuPc and the similar molecule PTCDA observed by Gordan *et al.* [178] suggests that these materials form promising extended heterojunctions for OPVs.

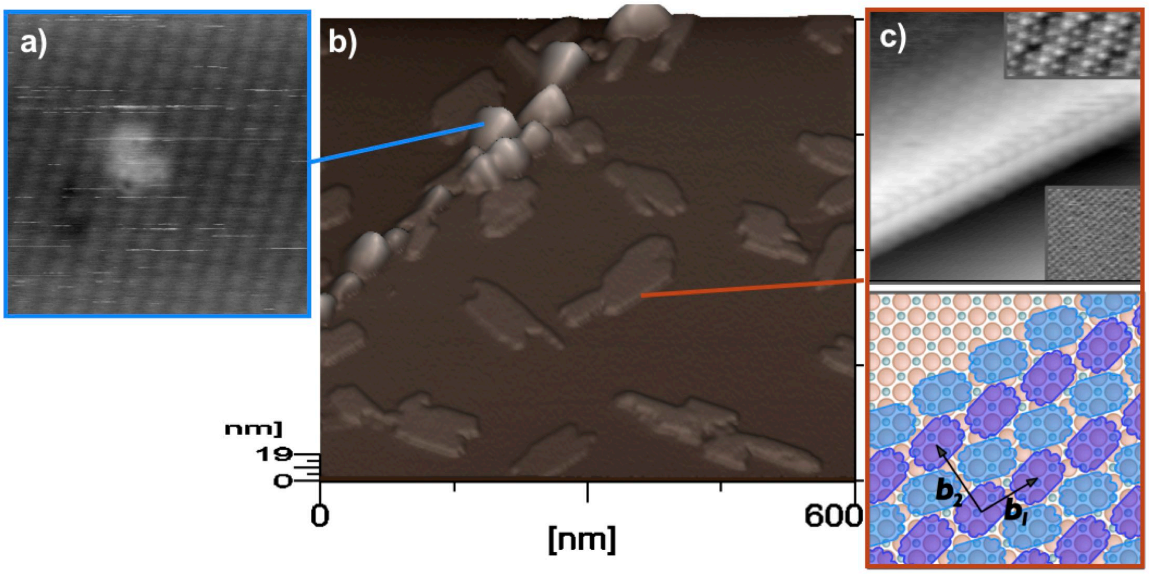

Figure 4.7: Morphology of 0.1 ML CuPc and 0.6 ML PTCDI deposited on KBr. (a) molecular resolution on CuPc, 15 nm×15 nm, Δf = -26 Hz, Γ = -3.8 fN$\sqrt{m}$, *image credit Sarah Burke* (b) film overview, 600 nm×600 nm, Δf = -3.1Hz, Γ =-0.4 fN$\sqrt{m}$, (c) molecular resolution on PTCDI and atomic resolution on KBr substrate, 20 nm×20 nm, Δf = -20.1 Hz, Γ = -3.0fN$\sqrt{m}$.

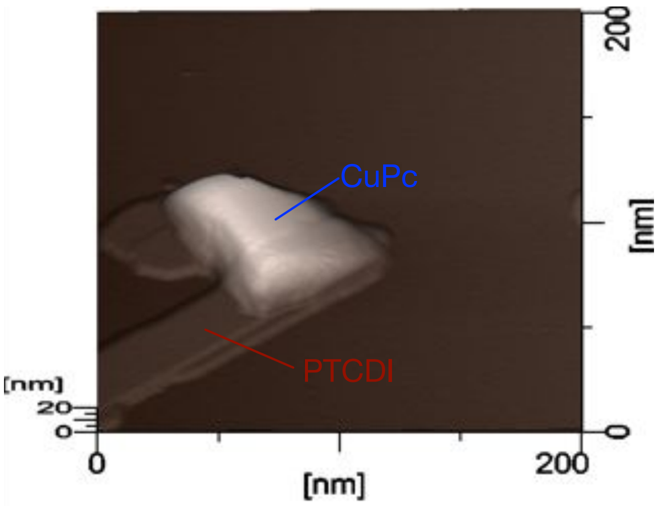

Figure 4.8: 3D rendered NC-AFM image of 0.5 ML PTCDI deposited before 0.1 ML CuPc. CuPc appears to nucleate on top of existing PTCDI islands

4.3.2 KPFM Contrast

Fig.4.9 includes a simultaneous KPFM image acquired during NC-AFM topography imaging, which is then overlayed on the 3D rendered topography to further illustrate the correlation between film morphology and LCPD. The flat PTCDI islands appear red in the KPFM image, corresponding to a high work function (expected for electron acceptors), and the tall CuPc islands appear blue, corresponding to a low work function (expected for electron donors, from which electrons are easily liberated).

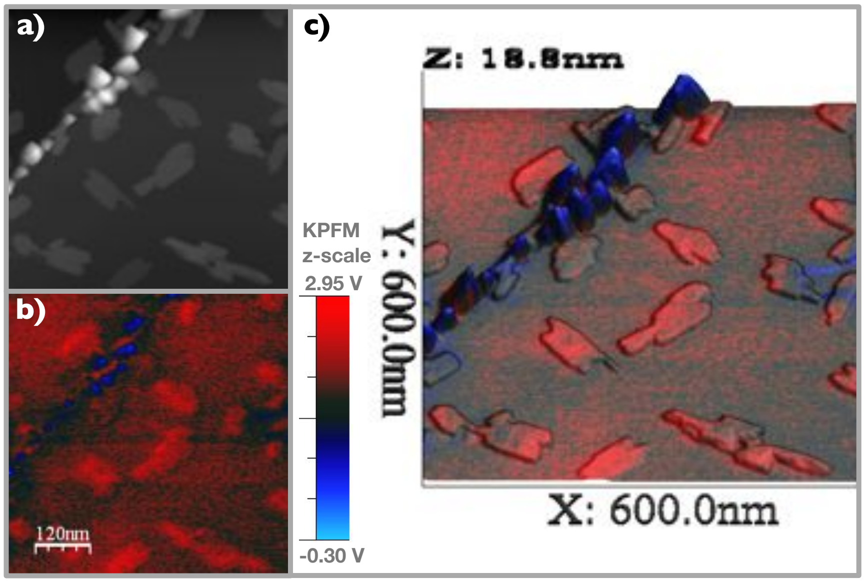

Figure 4.9: (a) NC-AFM topography image from Fig.4.7b with (b) the corresponding KPFM image, (c) 3D rendered and overlayed (colour mapped to avoid confusion from lighting effects) to illustrate the correlation between film morphology and CPD minimum distribution

Depletion Region

The PTCDI islands that formed in contact with the CuPc islands generally appear darker in the KPFM images than those isolated on KBr terraces (though the difference is difficult to quantify because of LCPD variations due to differences in island size, island edge effects, tip convolution and tip changes). This suggests that some charge transfer has taken place across the CuPc-PTCDI heterojunction prior to illumination (similar to the depletion or space charge region that forms around a pn-junction). Related observations have been made for other organic donor-acceptor combinations [162, 179]. Although charge transfer can occur simply due to Fermi energy level matching (the same principle used in KPFM), the measurement chamber is not perfectly dark (despite window coverings used) and a small amount of red light used to detect the cantilever resonance may reach the sample.

Upon closer inspection while imaging, an area between a CuPc island and a PTCDI island appeared with surprising KPFM contrast, indicated with blue arrows in Fig.4.10. It appears to be a thin bridge of molecules spanning between a CuPc island located at a KBr step edge and a PTCDI island on the KBr terrace. The LCPD suggests that the bridge is made of CuPc molecules, but the formation of such a structure is surprising given the tendency of CuPc to form tall islands. Another possibility is that it is PTCDI molecules that exhibit a lower LCPD ($\sim$work function) due to electrons donated from the attached CuPc island.

Molecular Anisotropy

Molecular anisotropy should be considered in OPVs. Different molecular crystallographic directions may conduct charge carriers differently, and organic

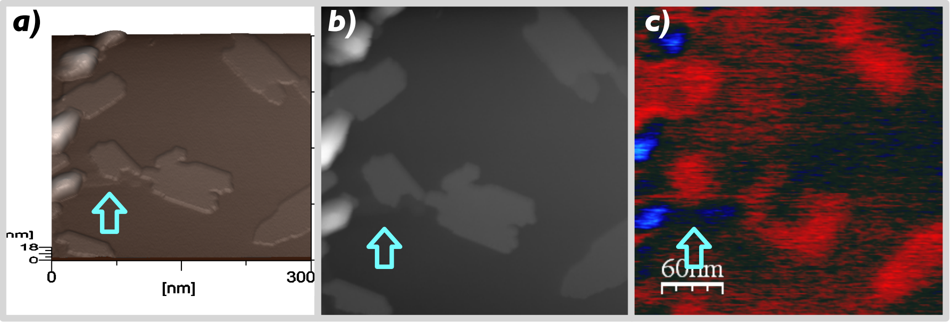

Figure 4.10: 300 nm × 300 nm (a) 3D rendered topography (b) NC-AFM image and (c) KPFM image. A thin bridge of molecules spans between a tall CuPc island and flatter, coalesced PTCDI islands that appears blue in the KPFM contrast

crystal structure and orientation could be an important consideration for device engineering. Perhaps charge carriers may hop more readily between molecular rows than along molecules from end to end, or vice versa. Planar molecules such as CuPc and PTCDA (very similar to PTCDI) have intrinsic optical anisotropy and anisotropic dielectric functions, as characterized by Gordon *et al.* [58, 178]. KPFM could prove a useful means of characterizing electronic transport anisotropy by analyzing the size of the "depletion regions" in different crystalline directions. Although the images achieved here are not high enough quality to perform such analysis (and tip convolution is certainly a compounding factor), Fig.4.11 illustrates possible KPFM characterization of anisotropy in charge carrier mobility. The area of dark KPFM contrast on the PTCDI island appears slightly fan-shaped, but would be round if transport were isotropic. KPFM line profiles taken along different directions (an example shown in Fig.4.11d of three line profiles taken along the dashed line), can be used to analyze LCPD as a function of distance from the heterojunction, similar to analysis performed by Meoded *et al.* on a GaP pn-junction [159]. This may yield better results on larger island sizes, and is an area for future exploration.

Edge Effects

Different crystalline faces can have different work functions and produce different LCPD. This can be caused by ordering of polar materials such as molecules, or surface rearrangements, but even the different faces of uniform perfect crystals can have different work functions (as predicted by Bloch theorem when distortion of the periodic potential near surfaces are considered [50]).

Close up images of some islands such as those in Fig.4.11 appear to reveal interesting LCPD around CuPc island edges. However, more data for rigorous comparison is required to rule out tip convolution. Differing KPFM edge contrast has been observed previously on faceted ZnO thin films, due to the presence of opposite charge domains formed during various surface rearrangements [180, 181]. Thin films of poly(3-octylthiophene) (P3OT) also form domains with varying KPFM contrast, expected to be related to the existence of dipoles due to different molecular arrangements [182]. KPFM measurements on 3″-methyl-4″-hexyl-2,2′:5′,2″:5″,2″′:5″′,2″″-quinquethiophene-1″,1″-dioxide (T5OHM, an electron acceptor) and regioregular poly(3-hexylthiophene) (P3HT, an electron donor) [162] resulted in tall crystalline T5OHM islands that occasionally display different KPFM contrast on the edges than in the middles.

4.3.3 Illumination

The sample was subsequently illuminated during imaging (similar to other OPV KPFM studies [49, 126, 160, 162, 183]), with blue laser light (473 nm, 50 mW max Melles Griot, shown in Fig.1.21.) The laser spot size is ∼1 mm but is incident

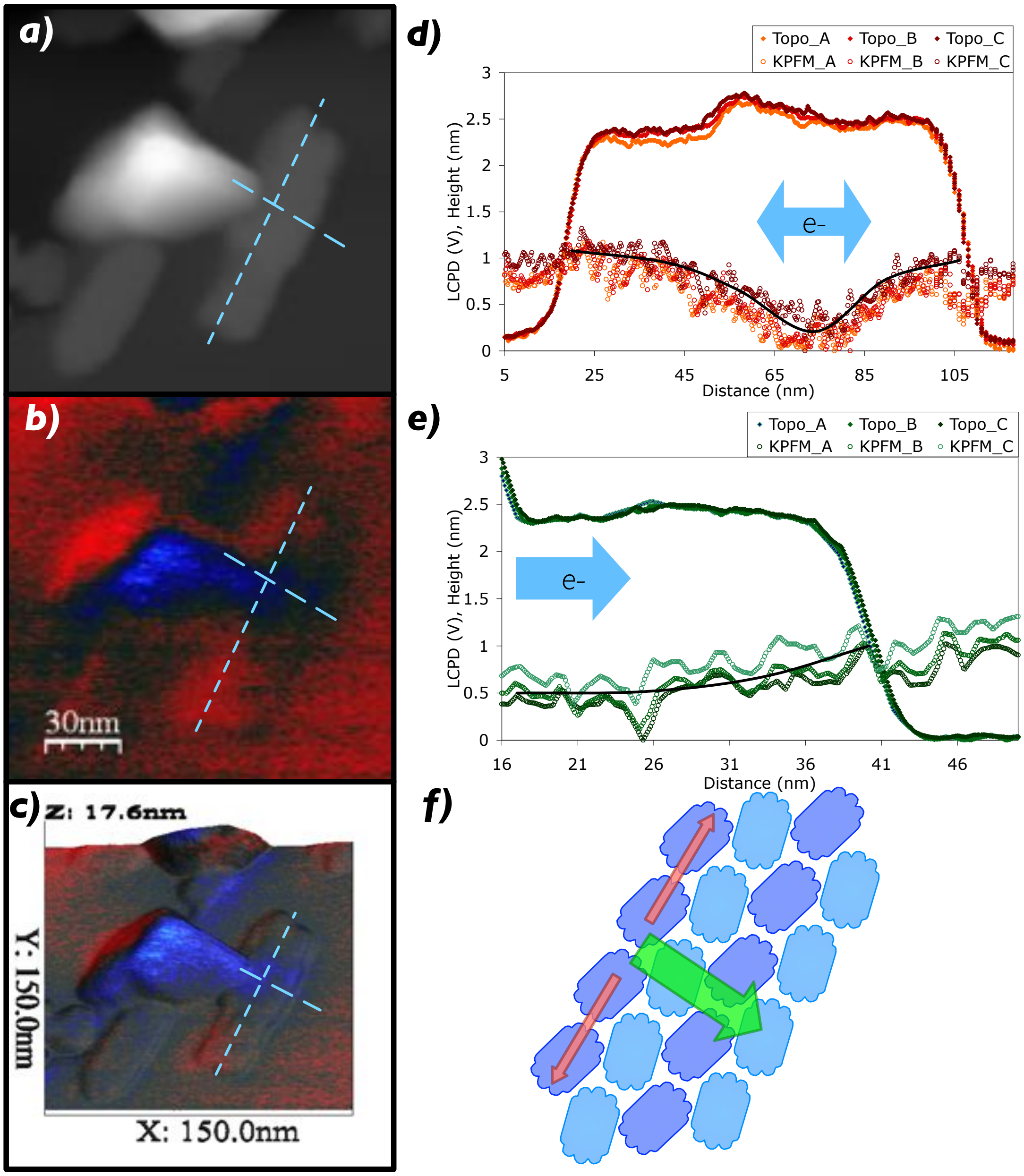

Figure 4.11: Possible anisotropy in charge carrier mobility: 150 nm × 150 nm (a) NC-AFM topography, (b) KPFM and (c) KPFM overlayed on 3D rendered topography images. Blue short-dashed lines indicate line profiles plotted in (d) and long-dashed lines indicate those plotted in (e), showing how the topography and LCPD around the heterojunction, which can be fitted to determine carrier mobility (in the regions indicated by black lines) and may depend on crystal anisotropy as illustrated in (f)

on the sample at a glancing angle. Many reflections occur in the reflective chamber and transparent sample, but a rough estimate of the surface intensity (irradiance) is 10 kW/m^2. The capability for more illumination wavelengths will be incorporated onto the system in the future. Illumination can induce a change in the work function of the tip by exciting a surface photovoltage [98], which must be accounted for. Because KBr is optically transparent, we may assume a constant work function and attribute the observed shift in KBr KPFM contrast under illumination to the Si cantilever. As discussed in Chapter 1, the quantitative LCPD values measured are not easily interpreted due to the complex tip-sample geometry, but serve as a qualitative means of sample characterization.

Upon illumination, some of the heterojunction contacted PTCDI islands appear darker in the KPFM image (an example indicated by the blue arrow in Fig.4.12 with corresponding line profiles given), and may disappear or partially disappear in the KPFM image, while the isolated PTCDI islands undergo very little change in contrast (note that “Light 1” in Fig.4.12c was taken immediately after the illumination laser was turned on. Thermal drift is particularly apparent in the z-topography as the piezo contracts to compensate for heating, making the islands appear taller, while no such artifacts are present in the LCPD as the KPFM feedback continues to perform properly). Unfortunately, significant image drift caused by thermal changes due to the illumination laser prevents image subtraction of the images collected in this experiment from providing a meaningful direct comparison of “before and after”. Also, most LCPD images include several minor tip changes that are invisible in topography, a clear example of which can be observed as a red stripe in the dark KPFM image. This is an unavoidable source of error in the LCPD data collected (and appears to be common in the literature but is of-

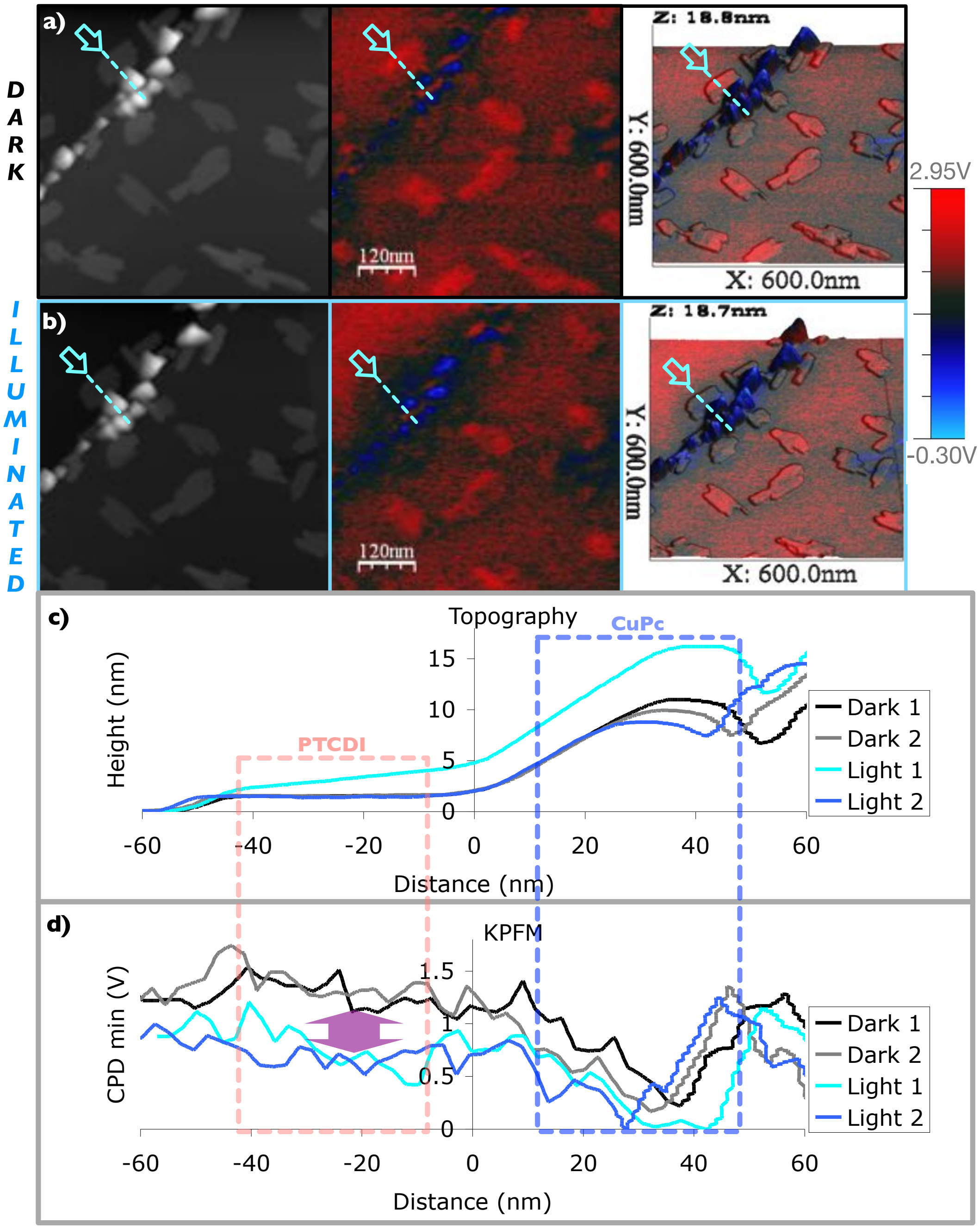

Figure 4.12: 600 nm × 600 nm NC-AFM topography, KPFM and KPFM overlayed on 3D rendered topography images with KPFM z-scale bar. (a) upper row images recorded in dark chamber, (b) lower row recorded under illumination with blue laser. Blue arrows indicate a contacted PTCDI island that displays a noticeable KPFM contrast change under illumination. Line profiles of (c) topography and (d) KPFM along dashed line in 4 consecutive images (2 dark, 2 illuminated), with purple arrow indicating contrast change. "Light 1" was taken immediately after the illumination laser was turned on, and thermal drift is particularly apparent in the z-topography

ten ignored, for example see [184]), but could be averaged out by collecting and analyzing a large amount of data.

We attempted to analyze the LCPD changes induced in a “zoomed in” image with more pixels per unit area. Fig.4.13 presents a group of CuPc and PTCDI islands in which a heterojunction is present. A small change in LCPD upon illumination is observable as the heterojunction contacted PTCDI island appears somewhat more blue (lower apparent work function). Analysis of the areas indicated by numbers in Fig.4.14 are given in Table 4.1 (the LCPD of each box is normally distributed from which the peak and standard deviation are measured) . Unfortunately, the error is still too high to quantify a change in the areas analyzed, despite the KPFM contrast change observed by eye and in the histogram envelope shape shown in green in Fig.4.14. The small scale of contrast change may be a result of charge carrier density saturation. Because charge carriers produced are unable to escape these isolated islands, coulomb repulsion may serve to prevent further charge separation from occurring at the heterojunction. This behaviour may change with island size. The island edges may also play an important role in charge redistribution under illumination that is overlooked by this analysis, but again, the edges are very difficult to compare between images due to drift and noise.

Although a clear difference between KPFM contrast in the dark and under illumination is not measurable everywhere (and more data is needed to verify these observations), the change in contrast observed for some PTCDI islands (indicated in Fig.4.12) in contact with CuPc islands suggests that illumination has enhanced electron or hole transfer across these heterojunctions. We rule out the possibility that the change in contrast is caused by excitons generated in the PTCDI

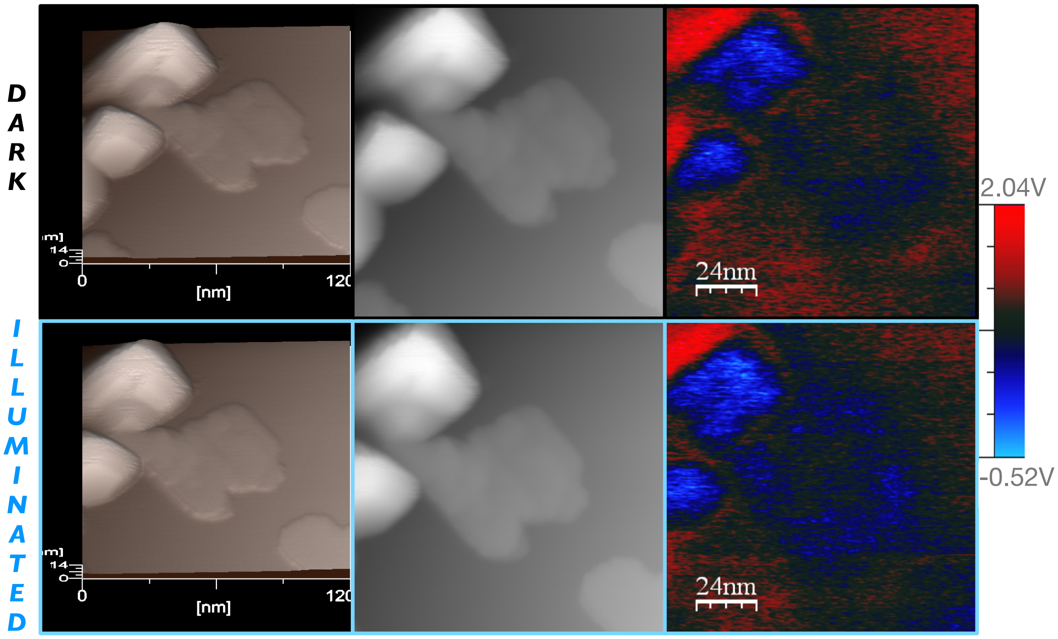

Figure 4.13: A heterojunction close up: 120 nm × 120 nm 3D rendered and standard 2D NC-AFM topography and KPFM images with LCPD z-scale bar. Top row images recorded in dark chamber, bottom row recorded under illumination with blue laser. Topographic details of islands and heterojunction are more visible in 3D rendered images

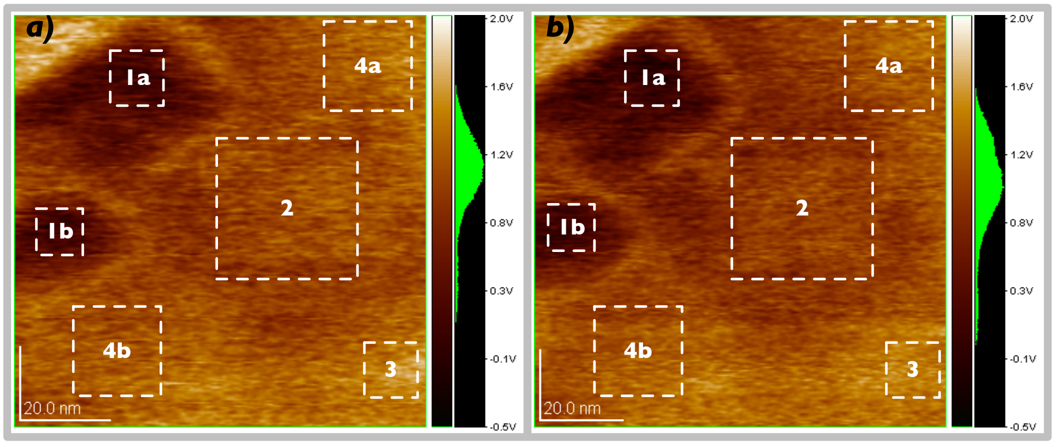

Figure 4.14: Heterojunction areas analyzed on images from Fig.4.13, a) dark and b) illuminated, with corresponding values given in Table 4.1. Green histograms indicate KPFM contrast prevalence over the entire image areas, which were cropped to overlap

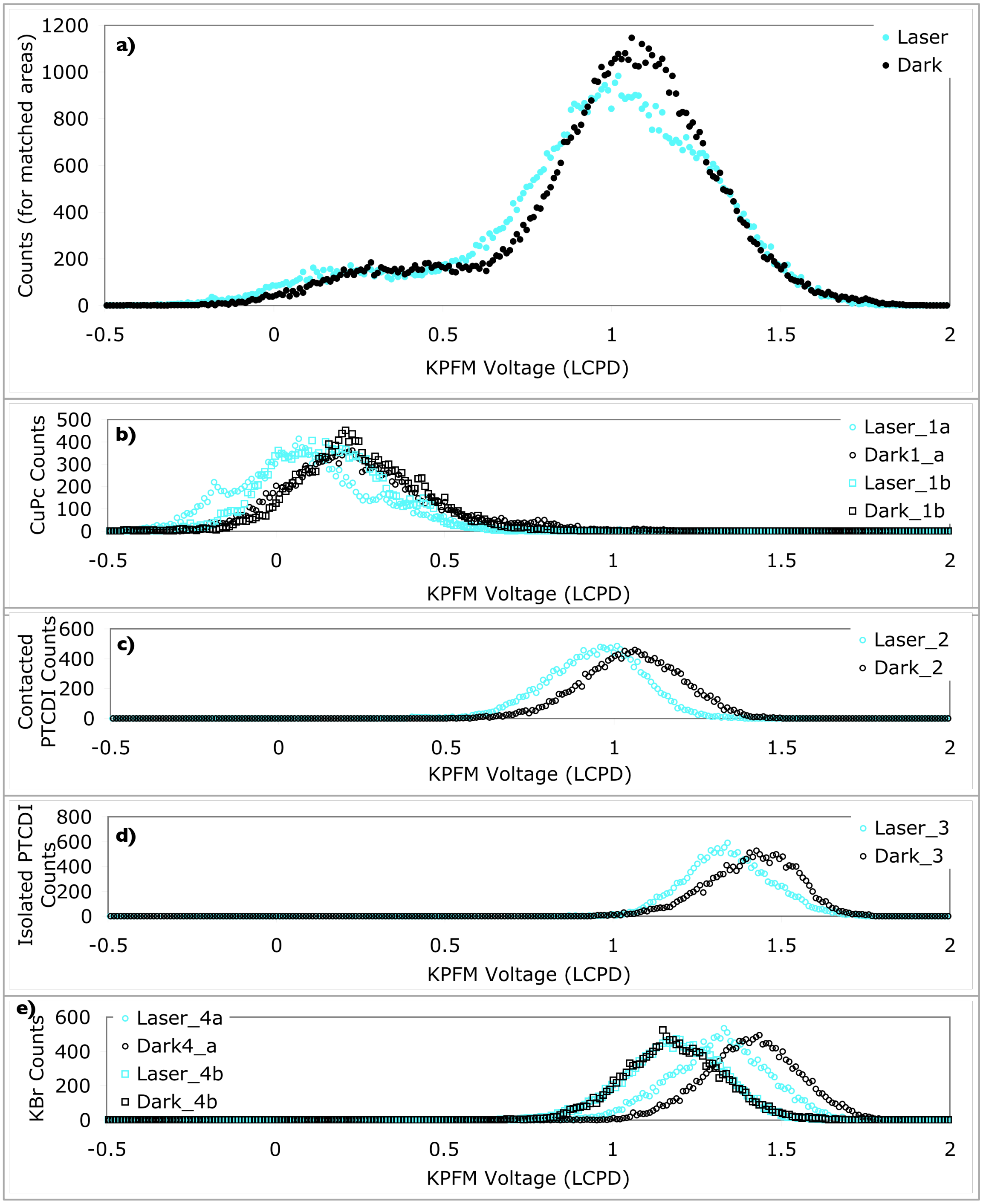

Figure 4.15: Heterojunction analysis of images shown in Fig.4.14, with corresponding values given in Table 4.1. Counts indicate LCPD distribution in specified areas over (a) whole images, (b) CuPc, (c) contacted PTCDI, (d) isolated PTCDI and (e) KBr. Tip changes can play a significant role in the contrast shifts observed

Area	Dark (V)	Illuminated (V)	ΔCPD min (v)
1a	0.1 ± 0.1	0.2 ± 0.2	-0.1 ± 0.2
1b	0.1 ± 0.2	0.2 ± 0.1	-0.1 ± 0.2
2	1.0 ± 0.1	1.0 ± 0.1	-0.1 ± 0.2
3	1.3 ± 0.3	1.4 ± 0.1	-0.1 ± 0.3
4a	1.3 ± 0.1	1.4 ± 0.1	-0.1 ± 0.2
4b	1.2 ± 0.1	1.2 ± 0.2	0.0 ± 0.2

Table 4.1: Comparison of KPFM values in the dark and under illumination, areas indicated in Fig.4.14

that are unable to separate (illumination has been observed to cause changes in KPFM contrast on PTCDA due to the presence of excited states that lower the effective work function [98]), because if the change in contrast were purely due to excitons generated in the PTCDI, then the PTCDI islands isolated on terraces should display the same change in contrast. Instead, we presume additional electrons in the PTCDI resulting from charge separation across the heterojunction decrease the apparent PTCDI work function and shift the corresponding CPD minimum value closer to that of the CuPc. If the change in contrast is purely due to charge separation across the heterojunction, both molecular species should undergo the same net change in charge. However, this is difficult to verify this experimentally, as charge may not be distributed heterogeneously throughout an island volume and the island geometry may serve to hide the population of charge offset in each island. NC-AFM and KPFM characterization of a range of island shapes and sizes could prove useful in elucidating these effects.

4.4 Summary

KPFM contrast on organic donor-acceptor thin films of CuPc and PTCDI was observed. CuPc had the lowest LCPD, corresponding to the smallest work function consistent with being an electron donor. Isolated islands of PTCDI on KBr terraces had high LCPD, corresponding to a high work function consistent with being an electron acceptor. However, PTCDI islands in contact with CuPc islands often appeared to have intermediate LCPD, suggesting that some transfer of electrons occurs from the CuPc across the heterojunction to the PTCDI even in the absence of illumination (neglecting a small amount of light from the cantilever deflection laser and around window coverings). This is similar to the space-charge or depletion region that forms around a pn-junction. Upon laser illumination, some further change in heterojunction-contacted PTCDI island KPFM contrast was observed, suggesting that charge transfer is enhanced as expected in OPV behaviour, but more data is required to verify these findings.

This data is among the first examples of KPFM performed on clean crystalline organic solar cell donor-acceptor materials under UHV. Molecular resolution was not achieved in this experiment, but the resolution demonstrated here suggests that high resolution simultaneous NC-AFM and KPFM imaging with a doped Si cantilever is possible. Although these early results may provide more questions than answers (about charge transfer, molecular anisotropy, edge effects, enhanced transfer under illumination, and heterojunction structure-function), a substantial amount of multidisciplinary research is needed to better understand OPV behaviour and apply it to device optimization. Structure-function relationships in donor-acceptor materials can be explored with simultaneous NC-AFM and KPFM on clean, crystalline samples grown under UHV. Understanding the fundamental physical processes of solar energy harvesting will light the way for future OPV devices.

5

Conclusions and Outlook

5.1 Conclusions

Organic thin films are technologically relevant due to their optoelectronic properties and huge advantages over silicon based materials in materials costs and manufacturing processes [1–3]. The device relevant properties of organic films are dependent on film structure. Molecular growth differs from that of inorganic materials due to influences from internal degrees of freedom, van der Waals force interactions and large area interaction potentials [74]. As such, molecular thin films may be more prone to post-deposition ripening processes such as the dewetting of PTCDI on NaCl (see Fig.5.1) characterized in Chapter 2. The ability to anticip-

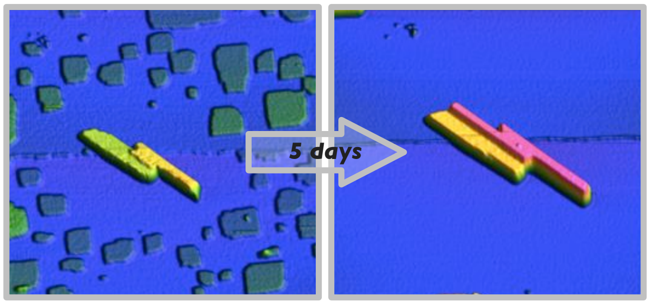

Figure 5.1: Dewetting of PTCDI deposited on NaCl. 400 nm × 400 nm NC-AFM images 3D rendered

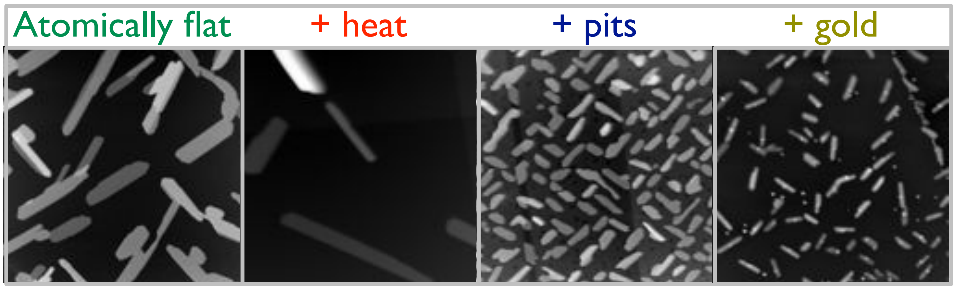

Figure 5.2: Tailoring the morphology of PTCDI on alkali-halides with growth conditions and surface restructuring. All images 600 nm × 600 nm NC-AFM

ate and selectively trigger changes in morphology marks an important step in the engineering of future organic devices [91].

Roughening and loss of film continuity are generally detrimental to organic electronic and optoelectronic device operation. However, heterojunctions are necessary for exciton dissociation in OPVs, so producing and maintaining a heterojunction-dense morphology for photovoltaics is crucial. The influence of growth conditions and surface structuring were investigated in terms of controlling the resulting film morphology (see Fig.5.2) in Chapter 3, with the ultimate goal of controlling the functional properties of optoelectronic devices [82]. The work presented here on PTCDI should translate to other molecular systems and may prove useful in designing and tailoring active layers of future organic thin film devices.

Organic photovoltaics represents an exciting technological application for molecular thin films with huge potential for growth in green energy. Morphology is known to play a crucial role in OPV device operation, but the specific mechanisms by which film structure influences performance are unknown [121, 122, 124, 126–129, 183, 185]. Preliminary studies of UHV deposited thin films of PTCDI and

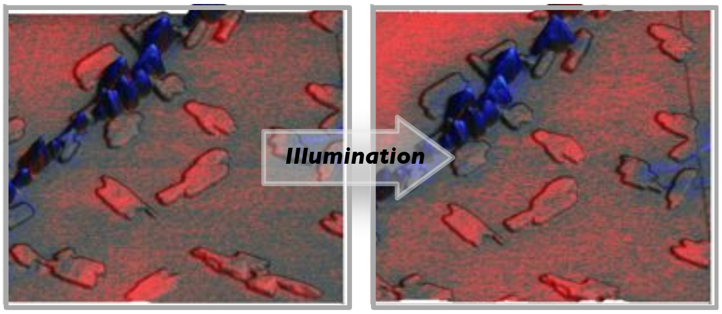

Figure 5.3: Organic photovoltaic behaviour of CuPc and PTCDI deposited on KBr. 600 nm × 600 nm NC-AFM images 3D rendered with KPFM overlay

CuPc performed with NC-AFM and KPFM (see Fig.5.3) were presented in Chapter 4. Although significant future research is required to fully understand and exploit the fundamental processes of organic energy harvesting, simultaneous NC-AFM and KPFM have been demonstrated as a promising approach to characterizing the structure-function relationship in molecular photovoltaic films.

5.2 Future Experiments

5.2.1 OPVs in an Electric Field

An external electric field applied across an organic electron donor and electron acceptor thin film should allow the manipulation of charge carriers, and perhaps enhance exciton dissociation [186]. An experiment of this nature has already been attempted in the JEOL system but has yet to meet full success. The experimental procedure (developed with the help of Shawn Fostner) takes place entirely under UHV as follows:

1. KBr samples are cleaved and masked with a Cu TEM grid on a retractable

mount (made by Shawn Fostner [187]) which is cut such that a single, 80 nm thick TEM beam covers a line across the centre of the sample. The beam can be oriented approximately along the [110] direction to produce a difference between PTCDI islands oriented along the [110] and $[1\bar{1}0]$ directions under applied bias

2. $\sim$30 nm of Au is subsequently deposited to produce two Au contact pads separated by $\sim$80 μm. The mask is removed and examples of the resulting film are shown in Fig.5.4 and Fig.5.5
3. A sub-monolayer film of molecules is thermally deposited (across the entire sample surface)
4. Contact foils are pressed on using a magnetic tool mounted on a transfer rod (also made by Shawn Fostner [187])
5. The completed assembly is then transferred from the preparation chamber to the imaging chamber
6. Electronic feedthroughs connected to the AFM sample stage allow the application of a bias across the contacts to produce an electric field. The applied bias causes a visible change in SEM contrast, as shown in Fig.5.5b

While each individual step is certainly feasible, experimental success requires the success of every consecutive step, which at this point has not been achieved despite several attempts. Typically, many (5 to 12) *in situ* cleave attempts are needed to produce a KBr sample that appears flat across the entire (001) surface (see Fig.5.4a), with no visible steps that could result in Au contact pad discontinuity. Once an ideal surface has been prepared, the masking and deposition processes are generally highly successful, but pressing on the contact clips and

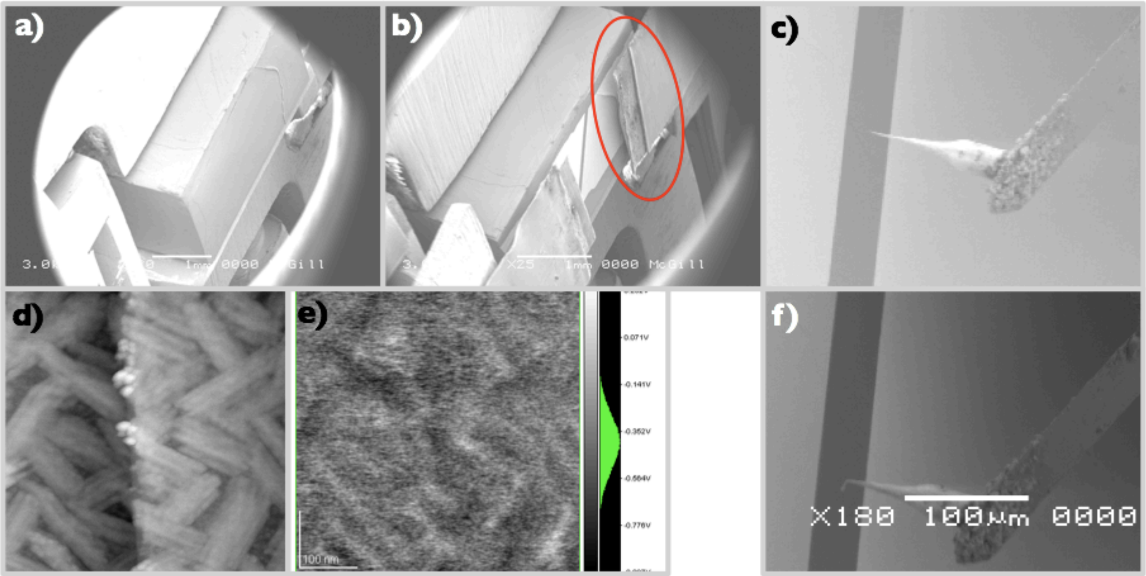

Figure 5.4: An attempt to observe the OPV behaviour of CuPc and PTCDI deposited on KBr in the presence of an electric field. (a) Freshly cleaved KBr (001). (b) Au pads and molecules were deposited on the KBr, and contact foils pressed into place. The red oval indicates the contact clip protruding from the sample that came into conflict with the cantilever chip on approach. (c) In attempt to reach the sample surface without touching the contact foil, an etched gold wire tip (made by Shawn Fostner [187]) was used instead of using a regular Si Nanosensors cantilever. Although imaging became possible, the Au wire ended in a multi-tip, as seen in the 500 nm × 500 nm NC-AFM (d) and KPFM (e) images. (f) An attempt to gently alter the tip termination through gentle contact with the sample ended in disappointment

transferring the assembly to the imaging chamber are opportunities for the Au pads to crack or de-adhere resulting in contact failure. Even successful assemblies have potential for other, more subtle means of failure. Two of the best experimental attempts made thus far are described as a proof of concept.

In the experimental attempt shown in Fig.5.4, the sample was assembled successfully but the contact foils protruded too far for a typical cantilever to approach the surface without the cantilever chip coming into contact (see Fig.5.4b). A longer etched gold wire tip (fabricated by Shawn Fostner [187]) was substi-

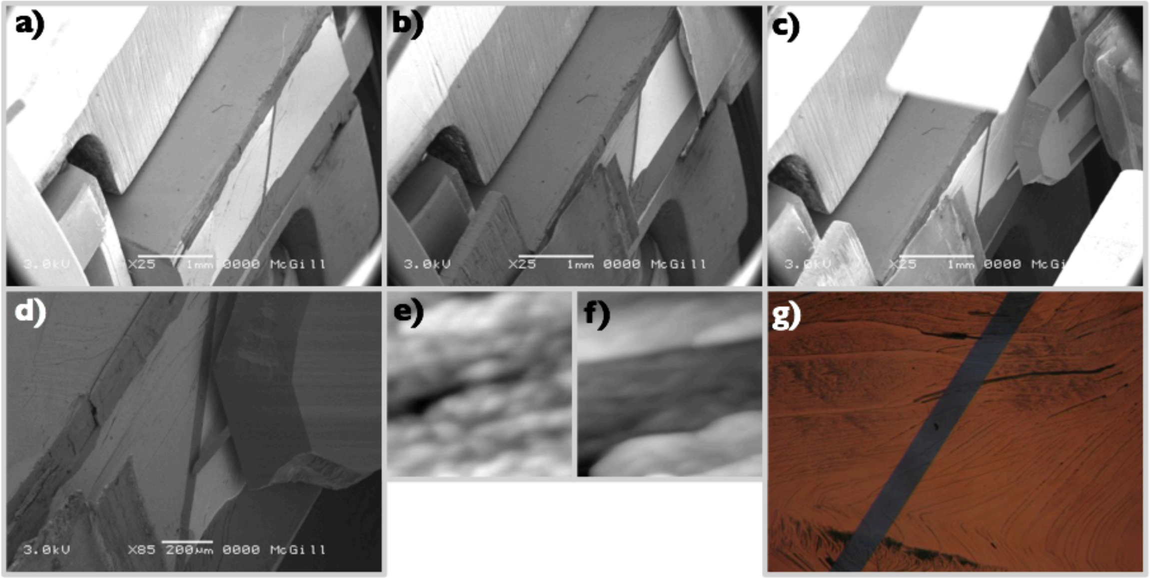

Figure 5.5: A second attempt to observe the OPV behaviour of CuPc and PTCDI deposited on KBr in the presence of an electric field. (a) Au pads deposited on KBr. (b) Contact foils pressed on, and a voltage of -10 V is applied to the right contact pad to verify connection. (c) The cantilever is approached to the surface and the SEM is used to occasionally check position relative to the gap. (d) Imaging is possible under an applied electric field, which induces only minimal drift (tip-sample position changes on the order of 50 nm within moments of applying -5 V to the right contact as shown). Unfortunately, the sample surface was nanoscopically very jagged with a high density of steps along the entire gap between Au pads, as verified by (e and f) typical 300 nm × 300 nm NC-AFM images with a z-height on the order of 20 nm, unsuitable for experiment. (g) An optical microscope image taken *ex-situ* showing the high density of steps around the 80 μm gap, belied by the macroscopic appearance of smoothness

tuted (see Fig.5.4b), and reached the sample successfully. Unfortunately, it did not provide high image quality due to the presence of a multi-tip, as seen in the NC-AFM image in Fig.5.4d. A controlled indentation was attempted in the hopes of altering the tip termination for the better, but instead it was destroyed, as seen in Fig.5.4f.

Another experimental attempt is depicted in Fig.5.5. In this case, each step in the assembly was successful, but upon imaging the KBr substrate was found to be extremely jagged despite appearing macroscopically flat. Vain imaging attempts were made along the entire length of the gap between gold electrodes, but in many places imaging was not possible and otherwise the surface was simply too jagged to be of use. Typical NC-AFM images obtained are shown in Fig.5.5e and Fig.5.5f, with small terraces and large z-heights on the order of 20 nm that make characterization of CuPc and PTCDI thin films impossible. The high step density was later confirmed by *ex situ* optical microscopy, an image of which is shown in Fig.5.5g.

This sample did however succeed in verifying that simultaneous NC-AFM and KPFM imaging in the presence of an applied electric field is possible with manageable drift. Fig.5.5d shows the tip approached to the gap with a bias of -5 V applied to the right hand side contact pad, which (when applied across an $\sim$80 μm gap) corresponds to an electric field of $\sim$ 60 kV/m. This is well below the dielectric breakdown field of KBr of 70 MV/m [188]. NC-AFM images taken before and during the applied bias showed a change in tip-sample position of $\sim$50 nm, and ceased to drift noticeably within moments. Future experimental attempts will hope to combine the success of all consecutive sample preparation steps with useful NC-AFM and KPFM OPV sample characterization.

5.2.2 Instrumentation

Additional illumination wavelengths will be incorporated onto the system for future experiments in order to probe a larger spectrum of organic photovoltaic behaviour. For example, red light can be used to selectively excite the electron donor, CuPc, for comparison with blue light experiments exciting the electron acceptor, PTCDI. This can be accomplished through the use of multiple lasers (possibly with tuneable wavelengths), or by combining a broad spectrum lamp (such as a Xe-arc lamp) with a monochromator for wavelength selection.

An external vacuum deposition chamber will allow the deposition of thicker samples on the order of 100 nm (such a large organic deposition would be detrimental to the clean UHV environment) for use in collaboration with Dr. Carlos Silva's group at Université de Montreal. The Silva group will perform time-resolved optical spectroscopy characterization of electronic processes through temperature dependent photoluminescence measurements. This will compliment the spatially-resolved scanning probe microscopy characterization techniques presented here.

5.2.3 Sample Improvements

Producing grain boundaries between connecting PTCDI islands should allow for the study of exciton and charge carrier transport across barriers, and such a film could be created with a multiple stepped deposition. Larger PTCDI islands will allow better characterization of KPFM contrast as a function of distance from heterojunctions, and could possibly reveal anisotropic charge carrier conduction due to the anisotropic nature of the molecular island crystals. The molecular thin film morphology can be tailored by growth parameters and substrate structure, as discussed in Chapter 3.

The height of CuPc islands is a barrier to NC-AFM imaging resolution, so a change in electron donor material is in order. For *in situ* preparation in the JEOL system, we require small molecules that are possible to thermally evaporate. Several small molecule electron donor candidates exist, among which pentacene appears quite promising [137, 148, 157, 189]. Pentacene thin film growth is well studied on a variety of surfaces [84, 85, 190–192] (including the alkali-halide KCl [193, 194]). It has been imaged with high resolution STM [195] and recently AFM [196], and is generally used for applications such as thin film transistors [2, 197] and organic photovoltaics [198–201].

Additional electron acceptor materials are also of interest. Fullerene derivatives (such as [6,6]-phenyl-C61-butyric acid methyl ester) are generally the electron acceptor materials of choice, given their high electron affinity and mobility [124, 130]. C_{60} has previously been well studied on alkali-halides [66, 90], but has relatively low photon absorption in the visible range (due to symmetry low energy transitions formally dipole forbidden [202]). Therefore a larger, less symmetric fullerene such as C_{70} with higher absorption may prove a better alternative electron acceptor choice [124, 202].

5.2.4 Ambient Contaminants

Organic photovoltaics layers feasible for use in real world devices are necessarily grown in ambient conditions to allow economic, scalable manufacturing. Solution processing is by far the most popular means of deposition [131–133], and such environments generally facilitate the incorporation of contaminants. Operation under ambient conditions (where the active layers are exposed to air) typically proves catastrophic [124, 125]. The influence of adsorbates on crystal growth in general has long been studied [203], but the specific mechanisms by which adsorbates induce traps and degrade OPV device performance are not known. Studies of organic thin films exposed to and deposited in air (or oxygen or water-rich environments) could be performed with NC-AFM and KPFM. Some solution based crystal growth modes tend to push impurities present to grain boundaries (for example, impurity rejection is known to occur in ice formation [204–206]). It may also be possible to design solution based organic film growth processes such that contaminants present are not incorporated in crystals in attempt to minimize negative impact on device performance.

5.3 On the Horizon

5.3.1 A Call for Modeling

Modeling, such as with density functional theory and kinetic Monte Carlo [83–85,207,208], could play a huge role in discerning the influence of kinetic factors and individual molecular scale dynamic processes on organic thin film growth. A predictions-based approach to active layer design could improve systems choices to complimentary molecule - substrate combinations and suggest a range of organic growth and device operation conditions. Many molecular processes contributing to dewetting and ripening phenomena are of interest, including interlayer mass transport, kinetic energy loss mechanisms, and molecular rotation and translation across various substrates and crystal faces. The anisotropic nature of molecular growth and mechanisms of nucleation at defect sites are of particular interest in terms of tailoring film morphology. The ability of gold nanoclusters to modulate the growth of needle shaped PTCDI islands is not currently understood.

In addition to crystal growth and structure, a better understanding of the electronic and optoelectronic properties of molecular assemblies would prove instrumental to device development (perhaps especially in systems where multiple growth modes exist). For example, multi-exciton generation [209] via singlet fission is a hotly debated phenomenon that is currently poorly understood, but may prove instrumental in energy harvesting [210–212]. An accurate model could help to predict and explain this processes. The ultimate goal is to fully understand and control molecular thin film growth, ripening behaviour, and functional properties as well as to provide a range of operating conditions (ie. temperature, environment and lifetime) for organic thin film devices.

5.3.2 Integration Challenges

The work presented here has focused entirely on characterizing the behaviour of isolated organic thin films. However, the ultimate goal is the integration of thin films into working devices for technological applications from organic photovoltaics to light emitting diodes to transistors. A conceptual drawing illustrating the key physical processes in a CuPc and PTCDI planar device in which the electrodes are used for charge collection is shown in Fig.5.6. Many additional challenges arise upon incorporation into devices. For example, contact electrode interfaces can act as barriers to energy harvesting with OPVs. Exciton blocking layers are commonly used to prevent exciton quenching at the active layer - cathode interface, significantly increasing device efficiency [59, 173, 213]. The performance of a solar device depends on incident light reaching the active layer, and photonic nanostructures can be used to increase light capture efficiencies by acting as waveguides and light injection devices [214]. Many such advances have been made and many future challenges await as development continues towards the bright future of functional organic thin films.

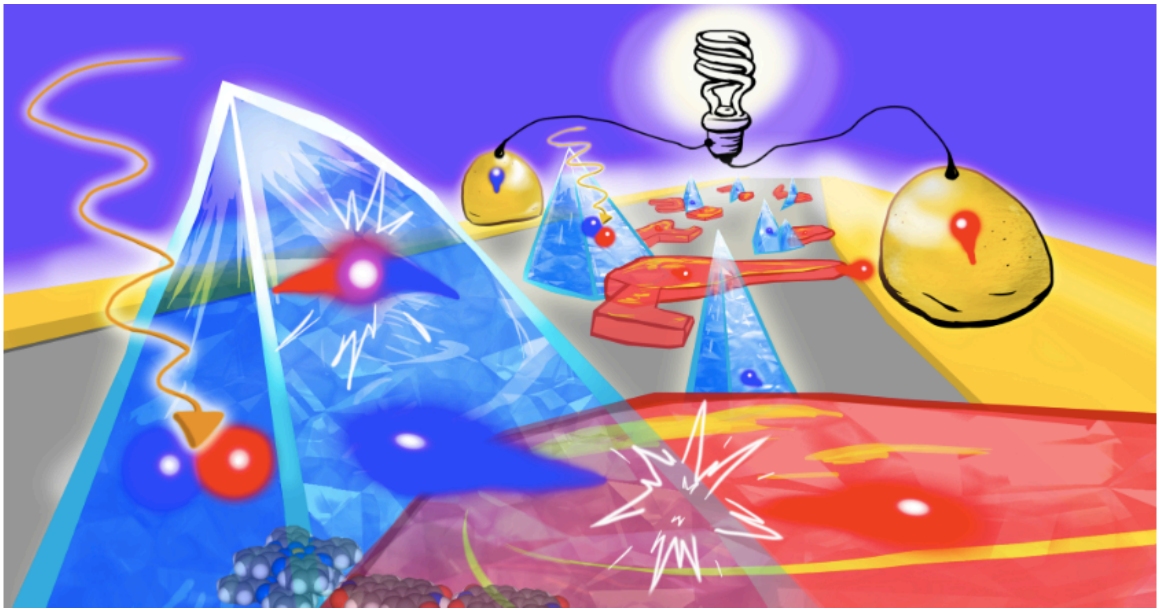

Figure 5.6: An artist's interpretation depicting key physical processes in a CuPc/PTCDI planar photovoltaic device *illustrated by Ben Topple*

A

Video Flip Books

The flip books on the following page depict the dewetting of PTCDI deposited on NaCl at room temperature:

1. Overview. Stable islands grow at the expense of metastable islands through mass transport. Needle islands grow in both height and area, and tend to elongate rather than widen. Substrate areas with high step density tend to contain many small needle islands and dewet quickly, while areas with low step density tend to slowly form fewer, larger islands as dewetting is limited by diffusion and nucleation site density.

2. Layer-by-Layer. Layer-by-layer growth of the lightning bolt shaped (bulk-like needle structure) island in the middle is visible, as well as mass transport and Ostwald ripening of the surrounding square shaped islands.

3. Nucleation. Needle island growth is nucleated between images at a position where the AFM tip interacted with the surface, producing a small local rearrangement or indentation. Coalesce and suppression are visible in the resulting needle island growth.

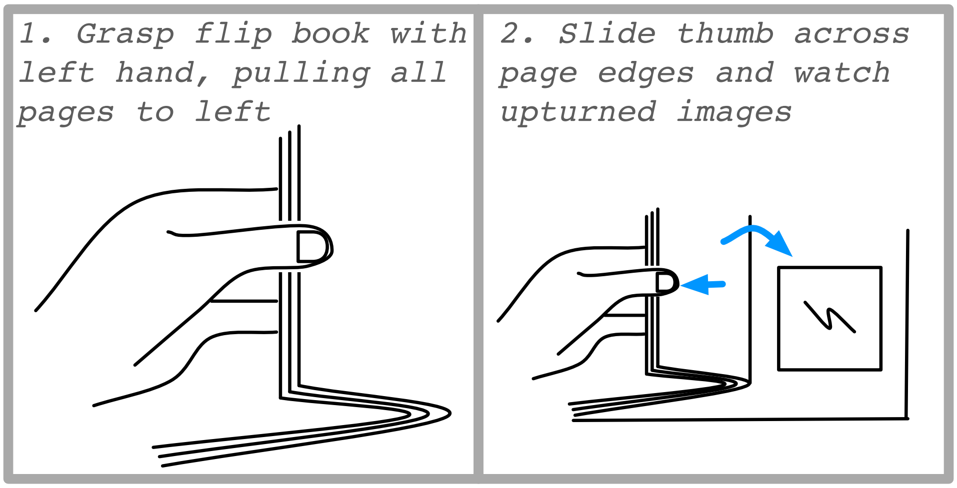

Figure A.1: How to use video flip books. Note that time increases from back to front

Overview
770 x 770 nm
elapsed time ~18h
September 2007
0.3 ML PTCDI
on NaCl at RT

t = 1208 min

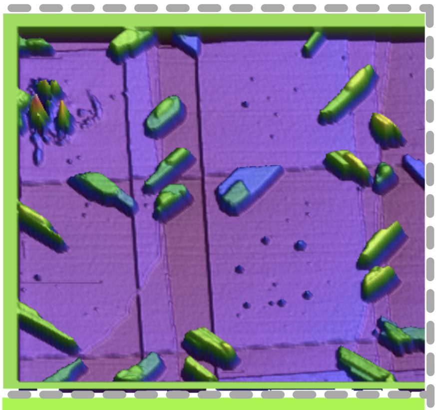

Layer-by-Layer
400 x 400 nm
elapsed time ~5days
May 2008
0.2 ML PTCDI
on NaCl at RT

t = 7113 min

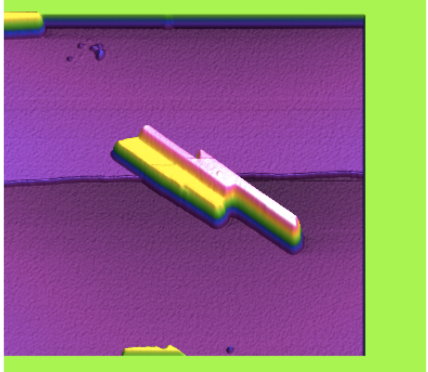

Nucleation
500 x 500 nm
elapsed time ~37h
May 2008
0.2 ML PTCDI
on NaCl at RT

t = 2227 min

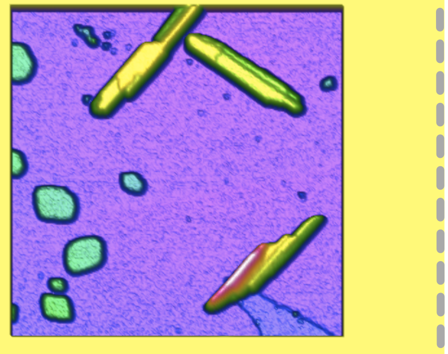

Overview
770 x 770 nm
elapsed time ~18h
September 2007
0.3 ML PTCDI
on NaCl at RT

t = 770 min

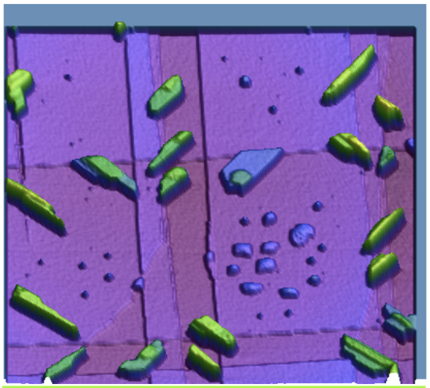

Layer-by-Layer
400 x 400 nm
elapsed time ~5days
May 2008
0.2 ML PTCDI
on NaCl at RT

t = 4279 min

Nucleation
500 x 500 nm
elapsed time ~37h
May 2008
0.2 ML PTCDI
on NaCl at RT

t = 1614 min

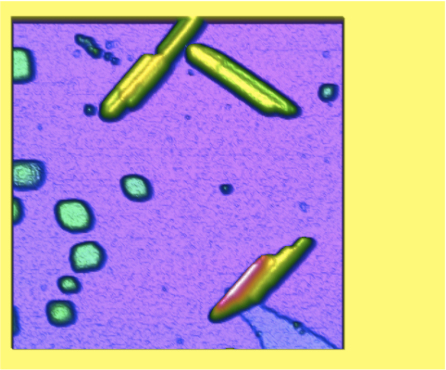

Overview
770 x 770 nm
elapsed time ~18h
September 2007
0.3 ML PTCDI
on NaCl at RT

t = 700 min

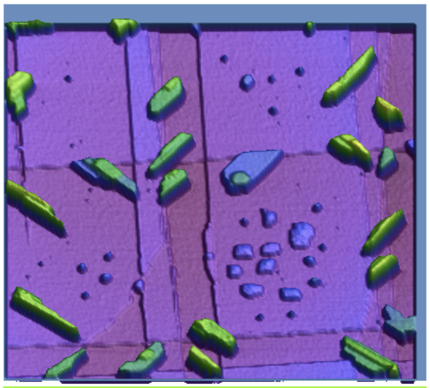

Layer-by-Layer
400 x 400 nm
elapsed time ~5days
May 2008
0.2 ML PTCDI
on NaCl at RT

t = 2689 min

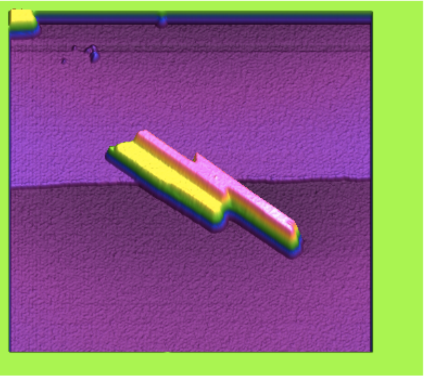

Nucleation
500 x 500 nm
elapsed time ~37h
May 2008
0.2 ML PTCDI
on NaCl at RT

t = 1470 min

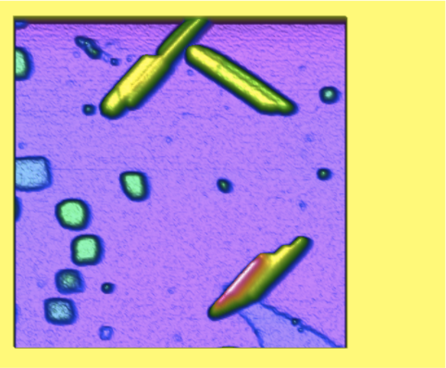

Overview
770 x 770 nm
elapsed time ~18h
September 2007
0.3 ML PTCDI
on NaCl at RT

t = 655 min

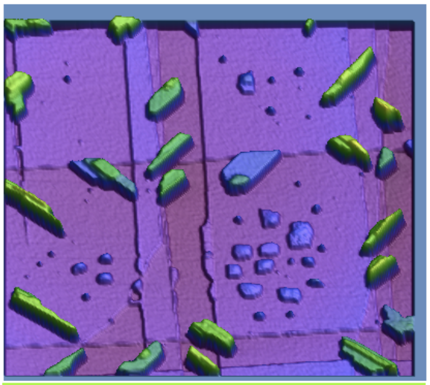

Layer-by-Layer
400 x 400 nm
elapsed time ~5days
May 2008
0.2 ML PTCDI
on NaCl at RT

t = 1694 min

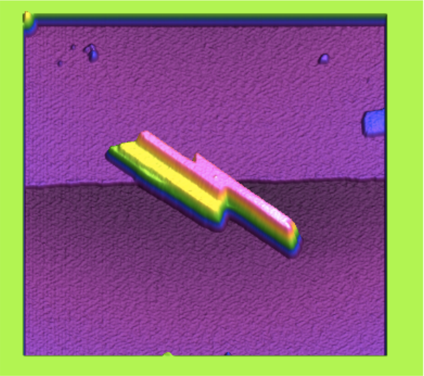

Nucleation
500 x 500 nm
elapsed time ~37h
May 2008
0.2 ML PTCDI
on NaCl at RT

t = 1253 min

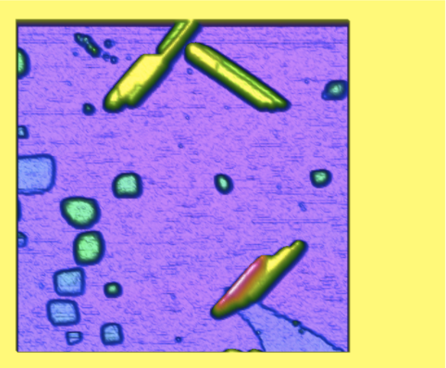

Overview
770 x 770 nm
elapsed time ~18h
September 2007
0.3 ML PTCDI
on NaCl at RT

t = 617 min

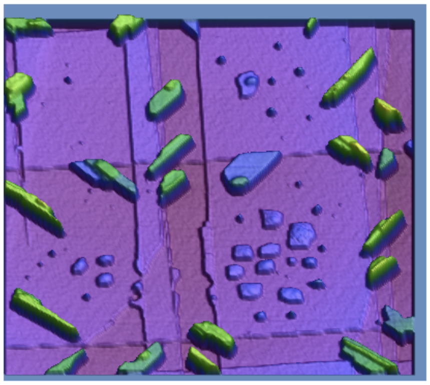

Layer-by-Layer
400 x 400 nm
elapsed time ~5days
May 2008
0.2 ML PTCDI
on NaCl at RT

t = 1522 min

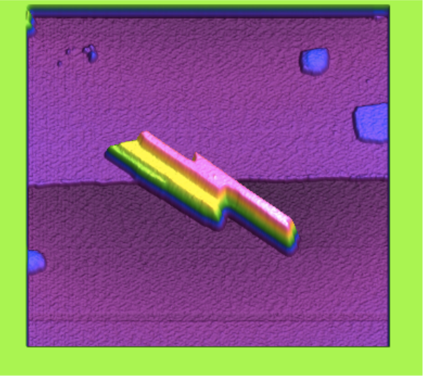

Nucleation
500 x 500 nm
elapsed time ~37h
May 2008
0.2 ML PTCDI
on NaCl at RT

t = 1197 min

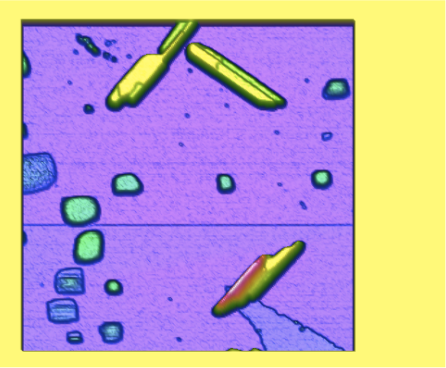

Overview
770 x 770 nm
elapsed time ~18h
September 2007
0.3 ML PTCDI
on NaCl at RT

t = 586 min

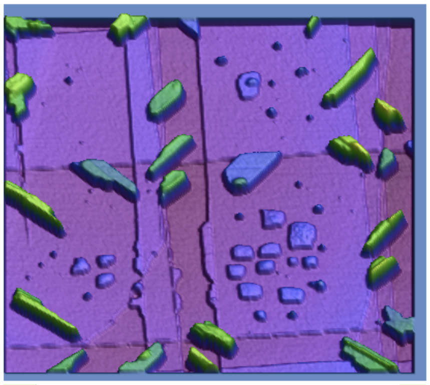

Layer-by-Layer
400 x 400 nm
elapsed time ~5days
May 2008
0.2 ML PTCDI
on NaCl at RT

t = 1424 min

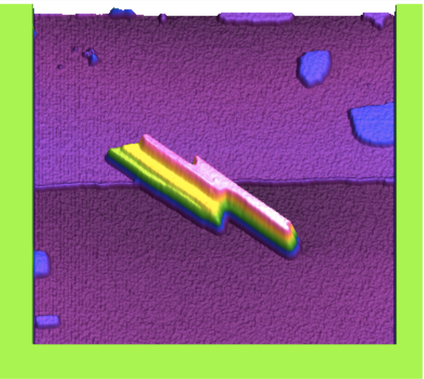

Nucleation
500 x 500 nm
elapsed time ~37h
May 2008
0.2 ML PTCDI
on NaCl at RT

t = 916 min

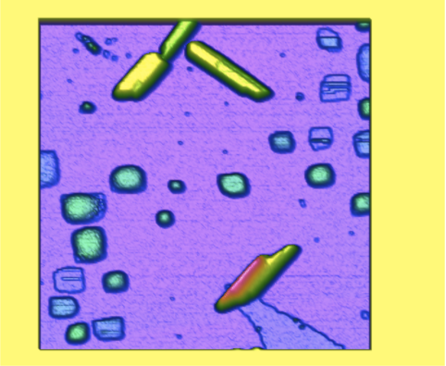

Overview
770 x 770 nm
elapsed time ~18h
September 2007
0.3 ML PTCDI
on NaCl at RT

t = 555 min

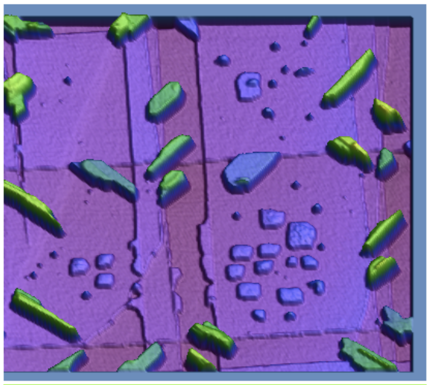

Layer-by-Layer
400 x 400 nm
elapsed time ~5days
May 2008
0.2 ML PTCDI
on NaCl at RT

t = 1324 min

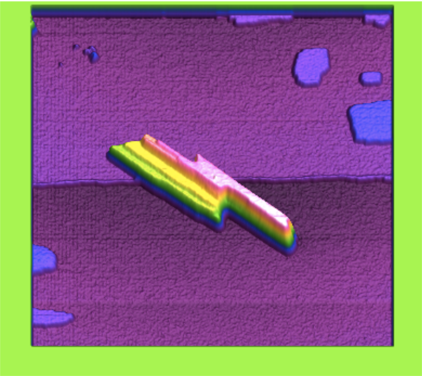

Nucleation
500 x 500 nm
elapsed time ~37h
May 2008
0.2 ML PTCDI
on NaCl at RT

t = 868 min

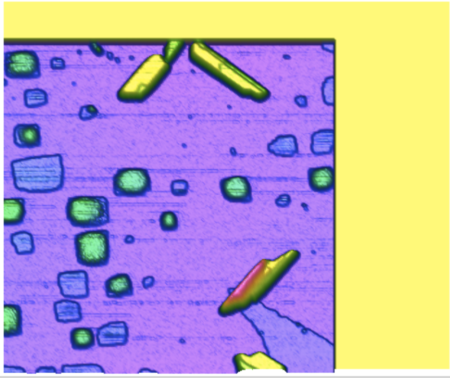

Overview
770 x 770 nm
elapsed time ~18h
September 2007
0.3 ML PTCDI
on NaCl at RT

t = 502 min

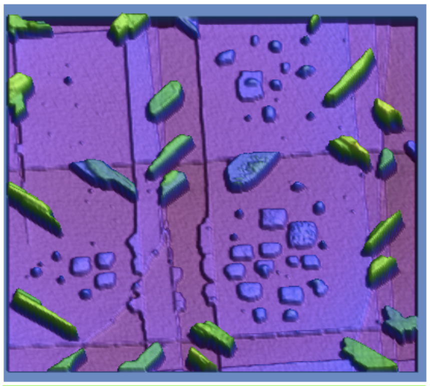

Layer-by-Layer
400 x 400 nm
elapsed time ~5days
May 2008
0.2 ML PTCDI
on NaCl at RT

t = 1250 min

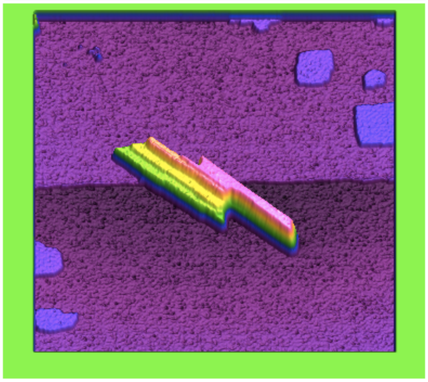

Nucleation
500 x 500 nm
elapsed time ~37h
May 2008
0.2 ML PTCDI
on NaCl at RT

t = 754 min

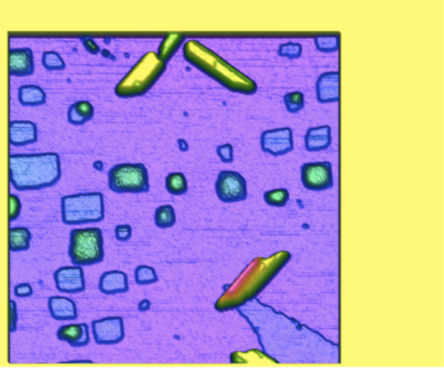

Overview
770 x 770 nm
elapsed time ~18h
September 2007
0.3 ML PTCDI
on NaCl at RT

t = 463 min

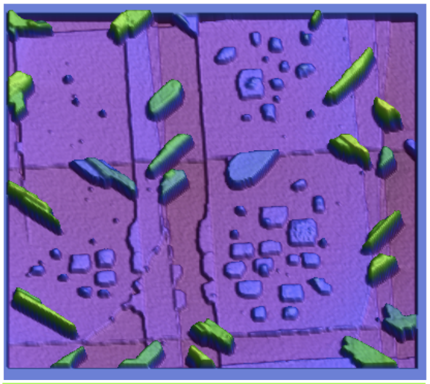

Layer-by-Layer
400 x 400 nm
elapsed time ~5days
May 2008
0.2 ML PTCDI
on NaCl at RT

t = 1131 min

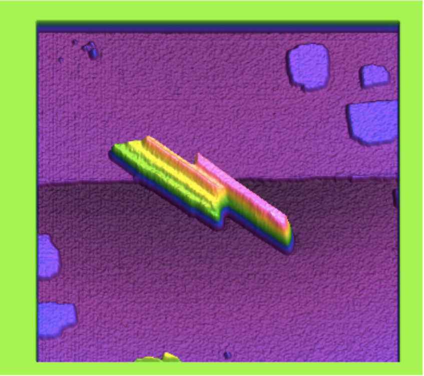

Nucleation
500 x 500 nm
elapsed time ~37h
May 2008
0.2 ML PTCDI
on NaCl at RT

t = 586 min

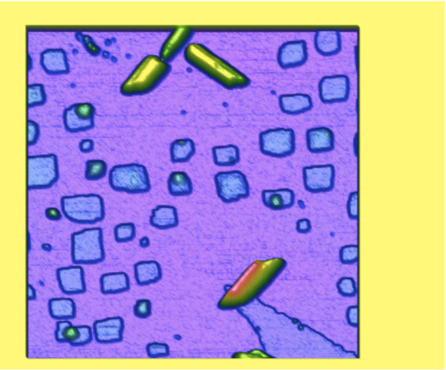

Overview
770 x 770 nm
elapsed time ~18h
September 2007
0.3 ML PTCDI
on NaCl at RT

t = 425 min

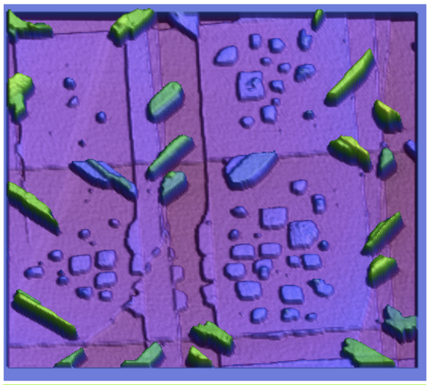

Layer-by-Layer
400 x 400 nm
elapsed time ~5days
May 2008
0.2 ML PTCDI
on NaCl at RT

t = 977 min

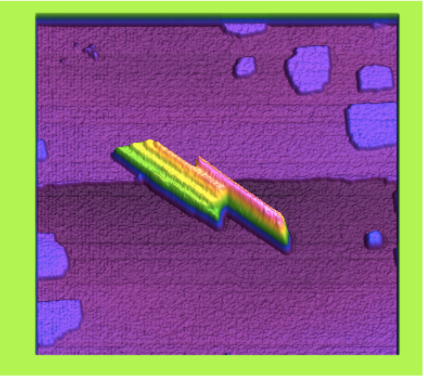

Nucleation
500 x 500 nm
elapsed time ~37h
May 2008
0.2 ML PTCDI
on NaCl at RT

t = 538 min

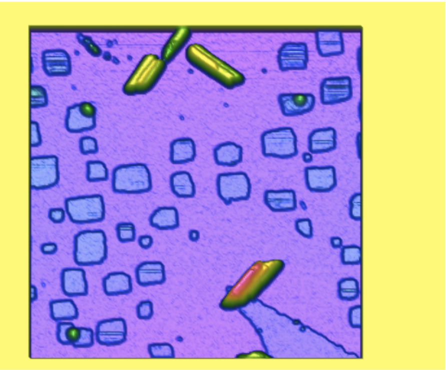

Overview
770 x 770 nm
elapsed time ~18h
September 2007
0.3 ML PTCDI
on NaCl at RT

t = 387 min

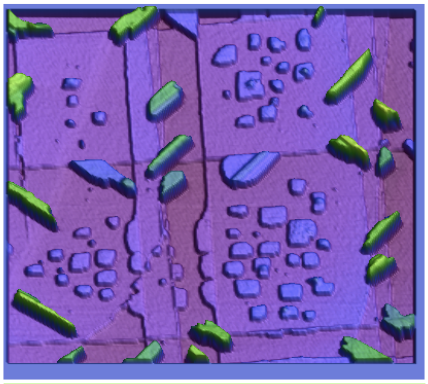

Layer-by-Layer
400 x 400 nm
elapsed time ~5days
May 2008
0.2 ML PTCDI
on NaCl at RT

t = 836 min

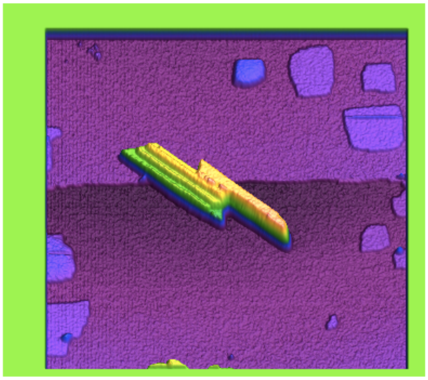

Nucleation
500 x 500 nm
elapsed time ~37h
May 2008
0.2 ML PTCDI
on NaCl at RT

t = 408 min

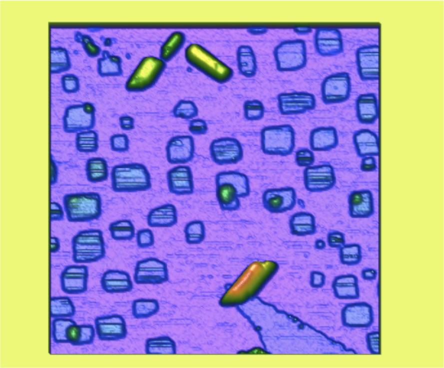

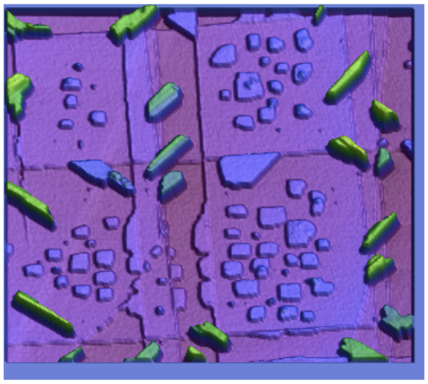

Overview
770 x 770 nm
elapsed time ~18h
September 2007
0.3 ML PTCDI
on NaCl at RT

t = 356 min

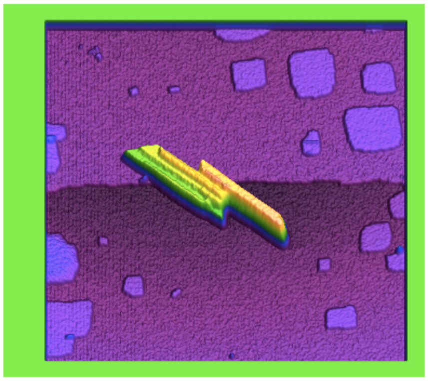

Layer-by-Layer
400 x 400 nm
elapsed time ~5days
May 2008
0.2 ML PTCDI
on NaCl at RT

t = 727 min

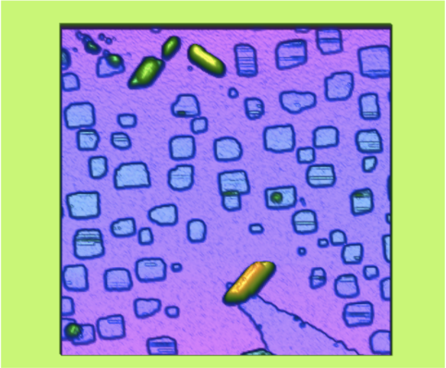

Nucleation
500 x 500 nm
elapsed time ~37h
May 2008
0.2 ML PTCDI
on NaCl at RT

t = 360 min

Overview
770 x 770 nm
elapsed time ~18h
September 2007
0.3 ML PTCDI
on NaCl at RT

t = 326 min

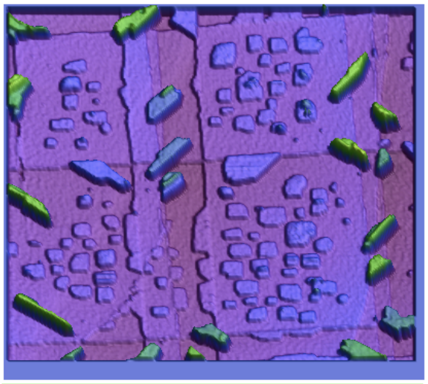

Layer-by-Layer
400 x 400 nm
elapsed time ~5days
May 2008
0.2 ML PTCDI
on NaCl at RT

t = 619 min

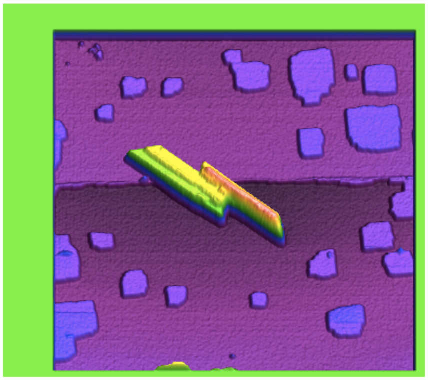

Nucleation
500 x 500 nm
elapsed time ~37h
May 2008
0.2 ML PTCDI
on NaCl at RT

t = 322 min

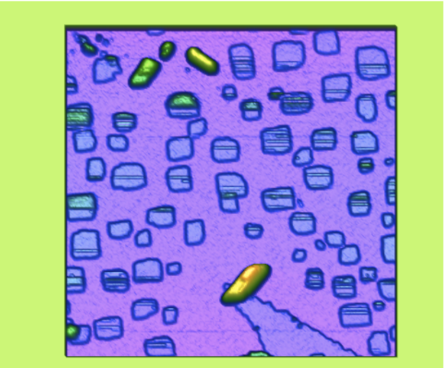

Overview
770 x 770 nm
elapsed time ~18h
September 2007
0.3 ML PTCDI
on NaCl at RT

t = 295 min

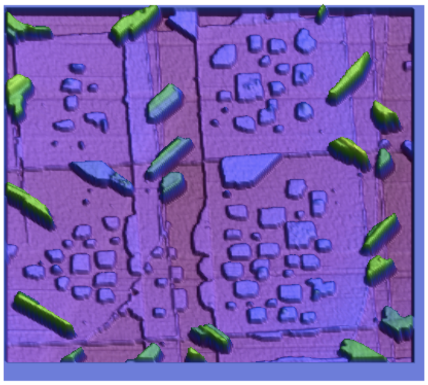

Layer-by-Layer
400 x 400 nm
elapsed time ~5days
May 2008
0.2 ML PTCDI
on NaCl at RT

t = 519 min

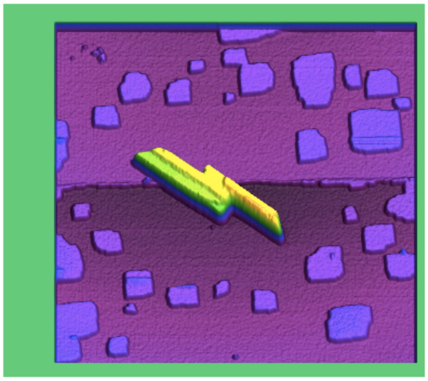

Nucleation
500 x 500 nm
elapsed time ~37h
May 2008
0.2 ML PTCDI
on NaCl at RT

t = 254 min

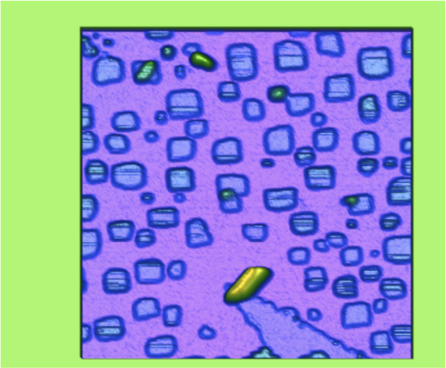

Overview
770 x 770 nm
elapsed time ~18h
September 2007
0.3 ML PTCDI
on NaCl at RT

t = 264 min

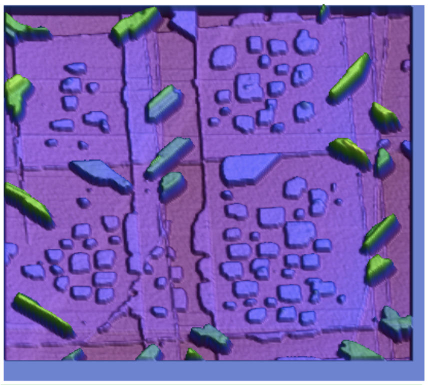

Layer-by-Layer
400 x 400 nm
elapsed time ~5days
May 2008
0.2 ML PTCDI
on NaCl at RT

t = 456 min

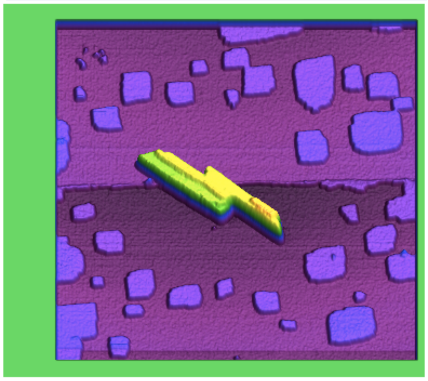

Nucleation
500 x 500 nm
elapsed time ~37h
May 2008
0.2 ML PTCDI
on NaCl at RT

t = 227 min

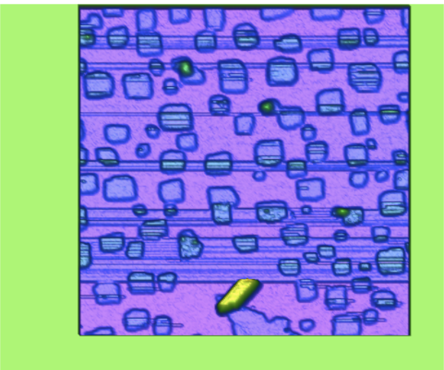

Overview
770 x 770 nm
elapsed time ~18h
September 2007
0.3 ML PTCDI
on NaCl at RT

t = 242 min

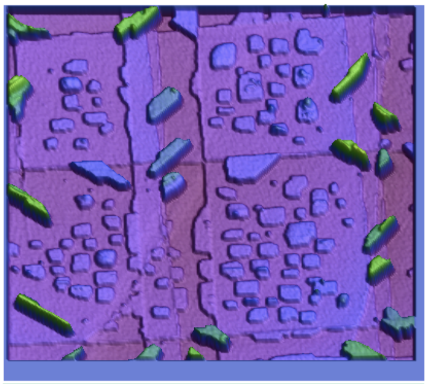

Layer-by-Layer
400 x 400 nm
elapsed time ~5days
May 2008
0.2 ML PTCDI
on NaCl at RT

t = 420 min

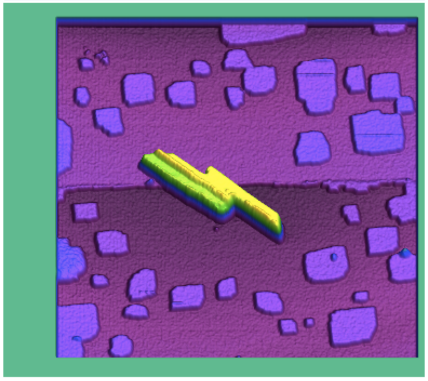

Nucleation
500 x 500 nm
elapsed time ~37h
May 2008
0.2 ML PTCDI
on NaCl at RT

t = 219 min

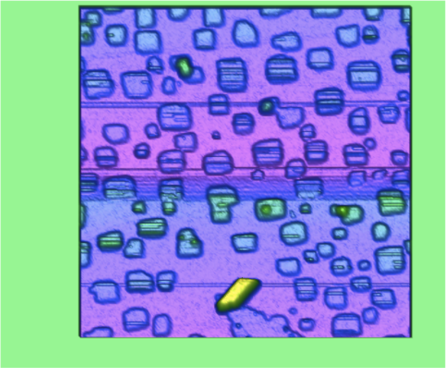

Overview
770 x 770 nm
elapsed time ~18h
September 2007
0.3 ML PTCDI
on NaCl at RT

t = 219 min

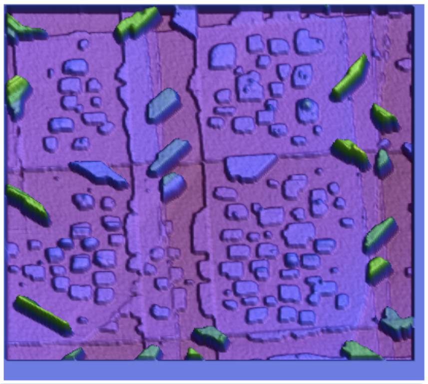

Layer-by-Layer
400 x 400 nm
elapsed time ~5days
May 2008
0.2 ML PTCDI
on NaCl at RT

t = 401 min

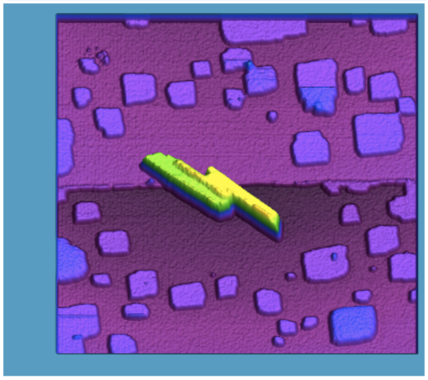

Nucleation
500 x 500 nm
elapsed time ~37h
May 2008
0.2 ML PTCDI
on NaCl at RT

t = 211 min

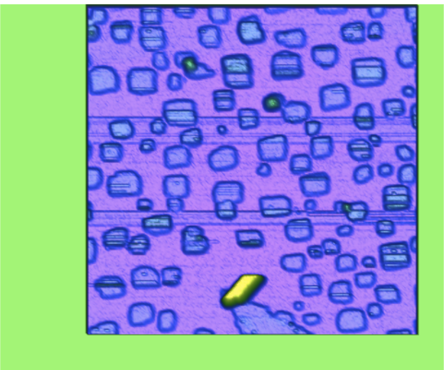

Overview
770 x 770 nm
elapsed time ~18h
September 2007
0.3 ML PTCDI
on NaCl at RT

t = 196 min

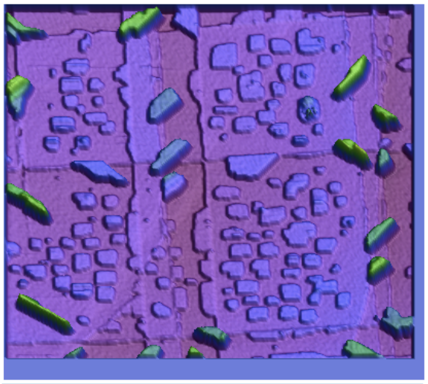

Layer-by-Layer
400 x 400 nm
elapsed time ~5days
May 2008
0.2 ML PTCDI
on NaCl at RT

t = 152 min

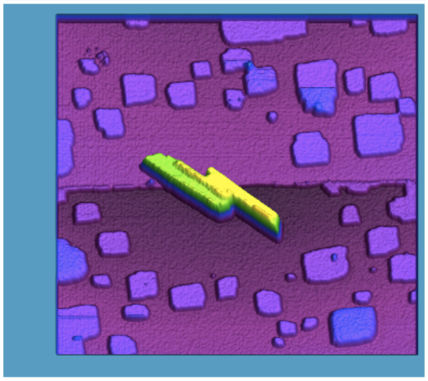

Nucleation
500 x 500 nm
elapsed time ~37h
May 2008
0.2 ML PTCDI
on NaCl at RT

t = 203 min

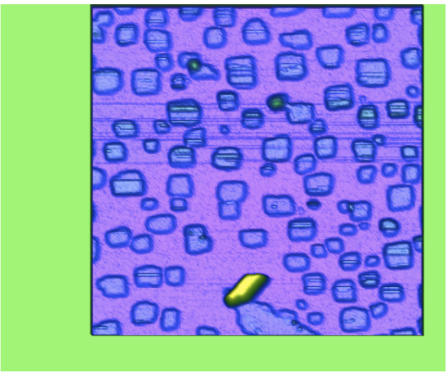

Overview
770 x 770 nm
elapsed time ~18h
September 2007
0.3 ML PTCDI
on NaCl at RT

t = 173 min

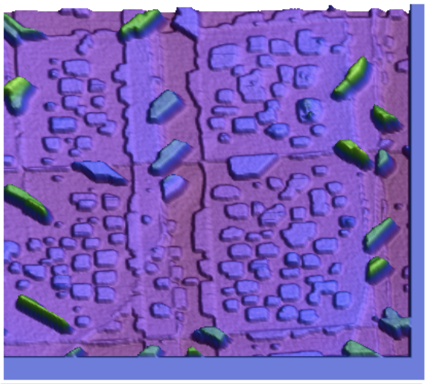

Layer-by-Layer
400 x 400 nm
elapsed time ~5days
May 2008
0.2 ML PTCDI
on NaCl at RT

t = 136 min

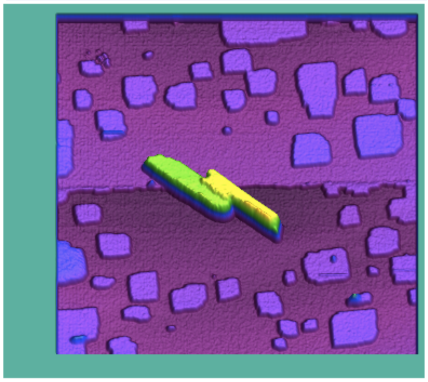

Nucleation
500 x 500 nm
elapsed time ~37h
May 2008
0.2 ML PTCDI
on NaCl at RT

t = 192 min

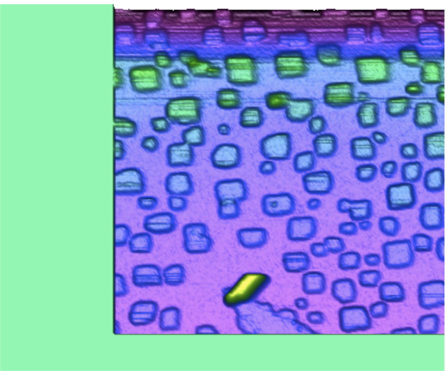

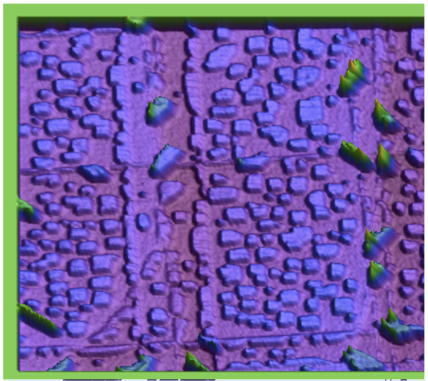

Overview
770 x 770 nm
elapsed time ~18h
September 2007
0.3 ML PTCDI
on NaCl at RT

t = 85 min

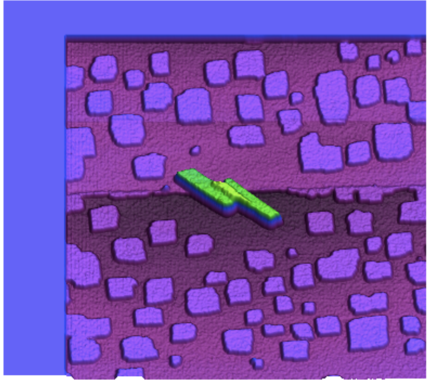

Layer-by-Layer
400 x 400 nm
elapsed time ~5days
May 2008
0.2 ML PTCDI
on NaCl at RT

t = 131 min

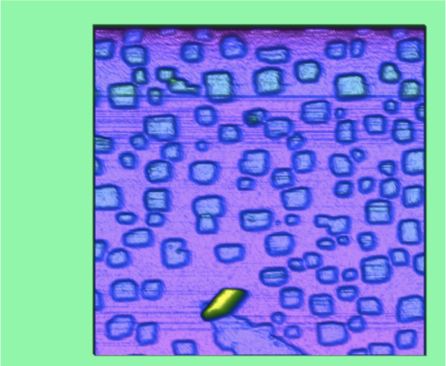

Nucleation
500 x 500 nm
elapsed time ~37h
May 2008
0.2 ML PTCDI
on NaCl at RT

t = 184 min

B

Low Temperature Experiments

Cooling PTCDI on alkali-halide samples *in situ* was attempted in the hopes of slowing thermally driven kinetic processes. As a first approach, samples were prepared by thermal evaporation in the preparation chamber and then quickly transferred into the measurement chamber sample stage. The stage was pre-cooled by the liquid nitrogen filled cryostat to ∼80 K. The AFM tip was approached and thermal changes slowed enough to allow imaging within a few hours. Upon imaging, the low temperature islands appeared rounded as illustrated in Fig.B.1. The rounded shape affords the possibility that the 2D gas phase freezes out upon cooling and joins the existing square shaped islands in at sites that with lower coordination than are favourable at room temperature. However, the islands roughen significantly with successive imaging as illustrated in Fig.B.2, eventually becoming unrecognizable. This puzzling behaviour was repeated in three separate experiments, and it was thought that perhaps the tip interaction induced local heating of the surface to produce this change in morphology.

A Kurt J. Lesker Mini-EVP Flange Mounted Thermal Evaporator was purchased and modified (machining by Pascal Bourseguin) to allow evaporation of molecules directly onto cooled samples in the measurement chamber. By mounting the evaporator on a measurement chamber flange (as illustrated in Fig. B.4)

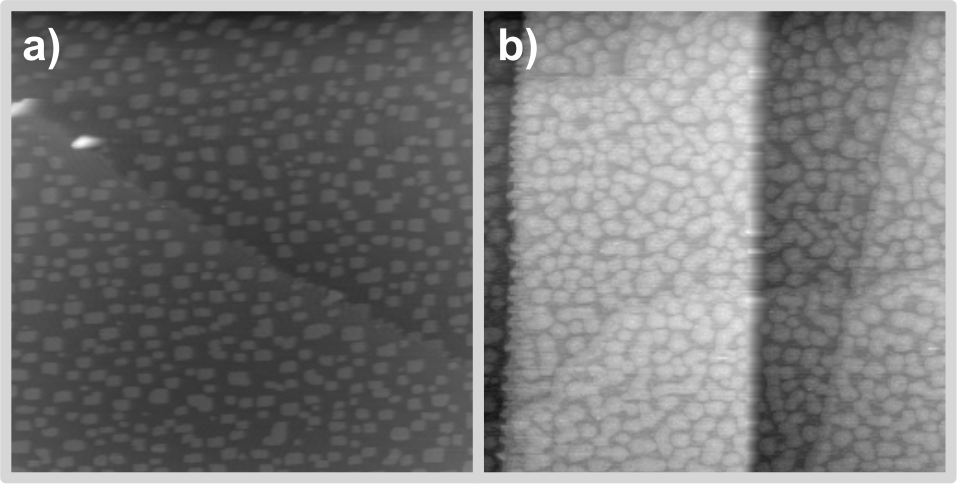

Figure B.1: Comparison of samples of 0.2 ML of PTCDI deposited on NaCl, quickly transferred to (a) room temperature and (b) liquid nitrogen cooled AFM sample stage. Both NC-AFM images 1 $\mu m \times$ 1 μm, with elapsed times of (a) 143 min and (b) 270 min since deposition onto room temperature substrates in preparation chamber

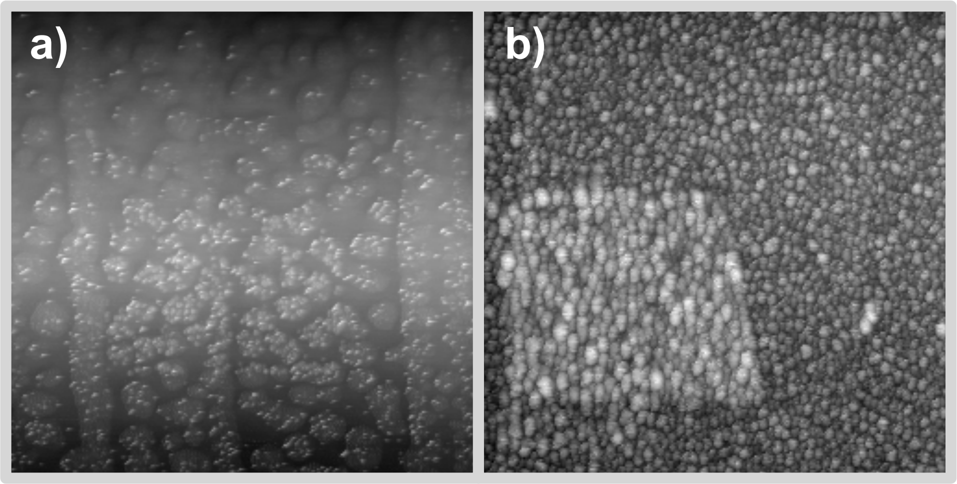

Figure B.2: 600 nm $\times$ 600 nm NC-AFM images of 0.2 ML of PTCDI on NaCl and transferred to liquid nitrogen cooled AFM sample stage at (a) 163 min, (b) 1305 min elapsed time since deposition onto room temperature substrates in preparation chamber. The effect of previous smaller sized imaging is apparent in (b)

and manually retracting the tip, it is possible to evaporate through a hole in the middle of the sample stage. Coarse manual tip retraction serves to shutter the deposition, as well as allowing a quick approach when ready to image. (The

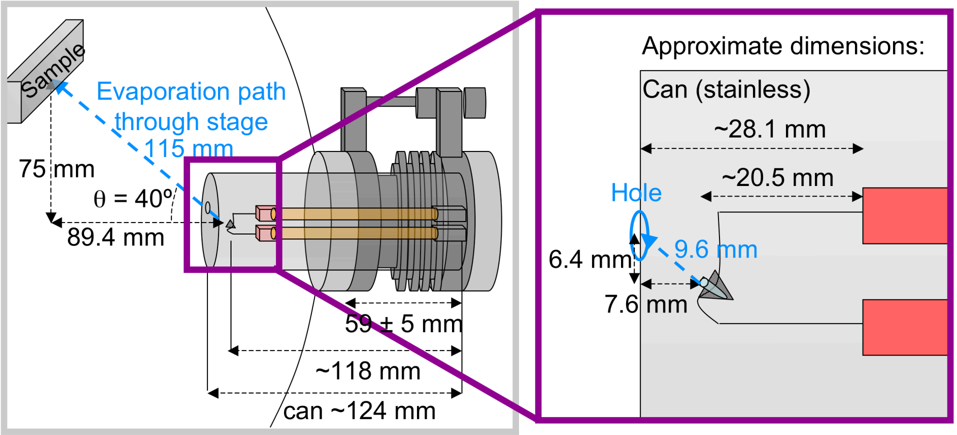

Figure B.3: Evaporator design featuring quartz crucible of molecules sitting in tungsten basket filament mounted on long copper electrode "legs". Assembly housed in can with hole for evaporation, flange mounted with Lesker Position Adjuster for alignment

deposition-to-imaging turnaround time can be as fast as ∼8 minutes in this configuration). A schematic of the evaporator design is illustrated in B.3 and the installation process is documented in Fig.B.4.

Room temperature testing of the evaporator was successful, however complications arose during low temperature experiments. Fig.B.5 shows successive images of a freshly cleaved clean NaCl surface with elapsed time since placing it in the cold stage. The growth observed is not that of PTCDI molecules, but rather of adsorbates from the vacuum. Indeed, the sample (and surrounding cold stage assembly) cryo-pumps the main chamber. The rule of thumb for estimating monolayer formation time is that it takes ∼1 s to form 1 ML at a pressure of 1 $\times 10^{-6}$ torr at room temperature with typical vacuum gas partial pressures and 100% sticking probability (based on the Hertz-Knudsen equation). This scales with 1/pressure, and therefore a back of the envelope calculation for our vacuum pressure of 2.7 $\times 10^{-8}$ Pa (or 3 $\times 10^{-10}$ torr) places the monolayer formation time for 100% sticking probability at ∼180 minutes. The observed growth is within a factor of 2 or 3 of

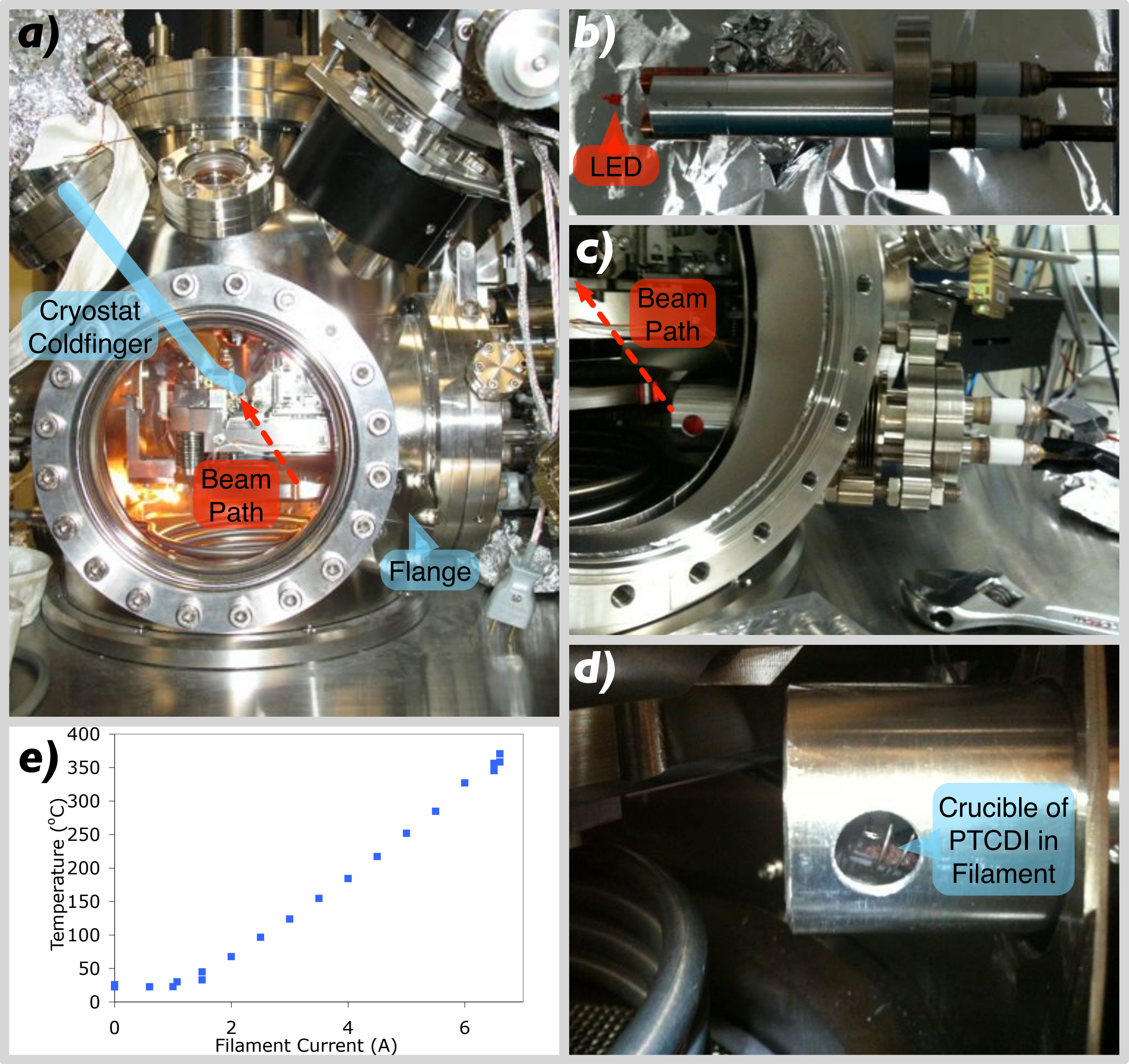

Figure B.4: Installation of measurement chamber evaporator. (a) Measurement chamber front view showing planned positioning of evaporator. (b) Modified Lesker Mini-EVP fitted with a red LED to test alignment through SPM stage (can removed). (c) LED test of alignment. (d) Final installation with quartz crucible of PTCDI molecules in W filament. (d) Temperature calibration curve from thermocouple testing in a small vacuum chamber this (imprecise due to tip-induced growth and difficulty in judging when a complete monolayer has formed). Therefore there is a high sticking probability (∼30%) on NaCl (001) at ∼80 K. At room temperature NaCl samples are kept on the order of 8 days before noticeable adsorbates are observed, generally only at step edges and kink sites.

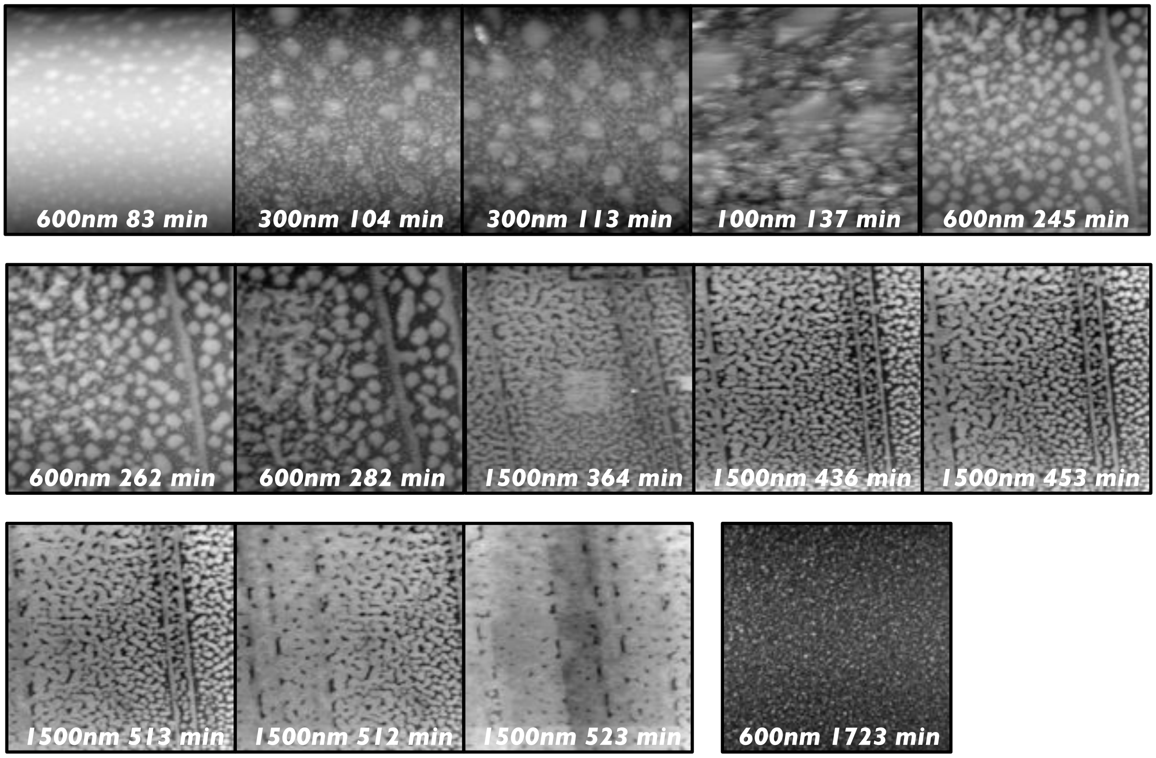

Figure B.5: Adsorbates apparently encouraged by scanning to create "burn box"-like areas on the previously clean NaCl surface as it cools. Text indicates scan size and time elapsed since placing the sample in the cold stage

Means of working around this problem were considered. A reduction in base pressure is infeasible (2.7 $\times 10^{-8}$ Pa is already quite good). Use the variable temperature (VT) heater mounted on the cryostat was attempted for the first time on this system, after a spike in chamber pressure was noticed upon warming up at a cryostat temperature of about 120 K. Unfortunately, the heater burned out almost immediately (the resistance across it changed from 8 Ω to 12 kΩ) despite careful control with a Lakeshore Model 331 Cryogenic Temperature Controller. JEOL has discontinued production and all technical support for this product.

The use of a cold finger to cool a sample stage in a large, predominantly room-temperature vacuum chamber appears questionable as a viable means of performing surface characterization at low temperature given the propensity of cold surfaces to cryopump the system, and therefore we draw no conclusions as to the effect of deposition on a cold substrate.

C

Graphene building blocks

A recent publication by Cai *et al.* explored the bottom - up assembly of graphene nanoribbons by surface assembly [215]. 10,10′-dibromo-9,9′-bianthryl (DBBA) molecules were deposited on Ag(111) and Au(111) surfaces, upon which the molecules lose their halogen substituents (the Br atoms disappear, leaving only C and H behind). The sample is then heated, and the biradical molecules diffuse across the surface to form linear polymers by radical addition. The system is further heated and a second thermally activated process takes place, surface-assisted cyclodehydrogenation to produce an extended, fully aromatic system: a graphene nanoribbon.

It seems possible for DBBA molecules to also lose their Br substituents when deposited on KBr, and thus we attempted a similar experiment. Discussions with chemistry colleagues revealed that strong molecule - substrate interactions are crucial in stabilizing the radicals [216]. To test the interactions on KBr, 0.3 ML of DBBA molecules (St-Jean Photochemicals) were thermally evaporated at a temperature of 140 °C onto room temperature KBr. The resulting growth is shown in Fig.C.1.

From the images presented, it is clear that molecule - molecule interactions dominated during growth to produce tall, compact islands of DBBA on KBr, and that molecule - substrate interactions are too weak to form the desired wetting

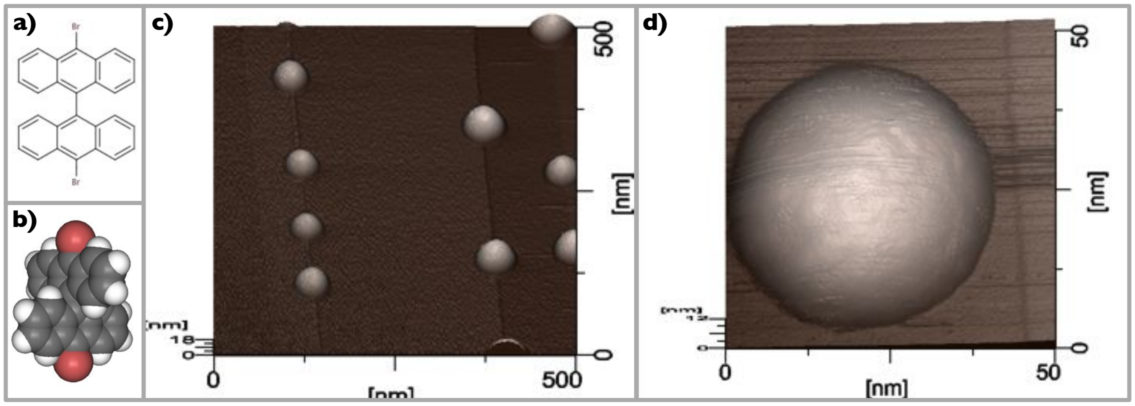

Figure C.1: DBBA molecules (a) structure and (b) space fill (both rendered using Marvin by Chem Axon), (c and d) 3D rendered NC-AFM images of 0.3 ML DBBA deposited on KBr

layer (on room temperature substrates). Our chemistry colleagues also suggested that deposition onto salt surfaces may lead to halogen exchange rather than radical formation [216]. Given that the growth mode observed was not ideal (flat) and the biradical precursors necessary for graphene nanoribbon assembly may not have formed, DBBA deposited on room temperature KBr appears to be a poor system candidate for producing surface assembled graphene.

Kittelmann *et al.* very recently achieved covalent linking of several halide - substituted benzoic acids on a different insulating surface, calcite [217]. In this case, surface calcium cations strongly interact electrostatically with molecular carboxylate groups, effectively tethering the molecules to the surface and preventing desorption such that homolytic cleaving temperatures can be reached to link the molecules. This seems unlikely to occur on alkali halide surfaces given their typical weak interaction with deposited molecules. However, bianthryls with iodine substituents may react more readily than those with bromine substituents [216], and for the right combination of molecule, substrate and experimental conditions, surface assembly of graphene on alkali halides may yet be possible.

D

The Bling Ring

A ring of LED lights was created to mount on a 2-3/4 inch window flange to illuminate the sample stage while allowing simultaneous optical access for a camera (see Fig.D.1 and Fig.D.2). The body was machined out of acrylic with the assistance of Shawn Fostner and Pascal Bourseguin. This design has proved popular and has been reproduced by admirers for other UHV systems around the world.

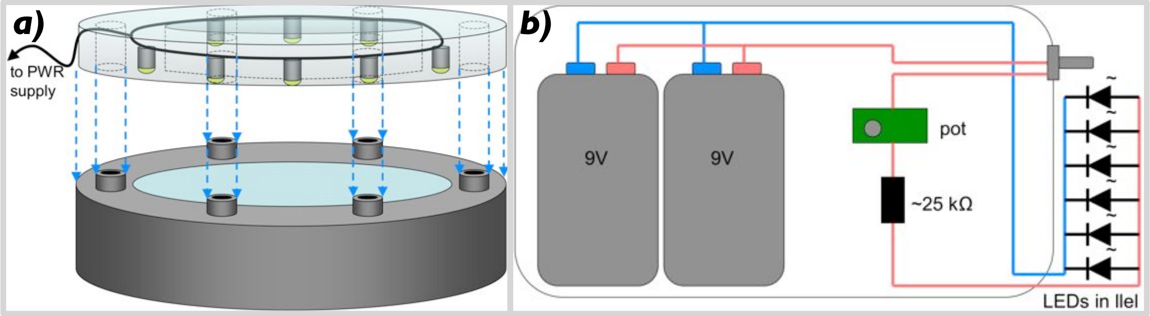

Figure D.1: The Bling Ring (a) illustration and (b) circuit diagram. Resistor values should be chosen for appropriate current limitations to the LEDs used

Figure D.2: The Bling Ring in operation

E

Connections

The schematic setup for frequency modulation using the nanoSurf PLL Sensor amplitude controller and FM detector (hardware modified from original configuration by Yoichi Miyahara) are given in Fig.E.1. The detection signal from the photodetector, *(A-B)*, corresponds to cantilever oscillation in the normal mode (causing a change in voltage detected between the two quadrants) and is input to the Sensor amplitude controller box. Software is used to set a variety of parameters such as the reference cantilever resonance frequency, f_0, frequency shift setpoint used for imaging, δf, the lock range, and gains. Other parameters such as the oscillation amplitude setpoint and constant phase difference are set directly on the hardware. The automatic gain controller (AGC) is used to maintain a constant cantilever oscillation amplitude by controlling the amplitude and phase of the excitation signal. The phase locked loop (PLL) is used to find the frequency shift, Δf, between the free oscillation resonance frequency, f_0, and the observed oscillation resonance frequency, $f_{oscillation}$, is output and used for distance control and KPFM as discussed in Chapter 1. The detailed connections and settings used for performing simultaneous NC-AFM and KPFM on the JEOL system in our laboratory are shown in Fig.E.2.

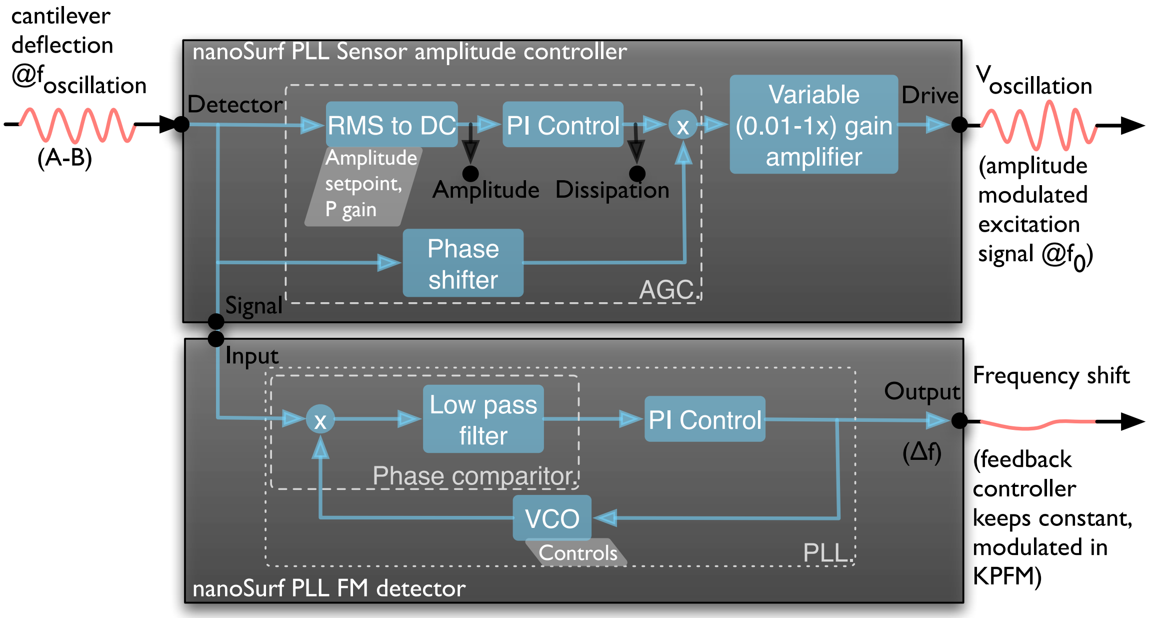

Figure E.1: Schematic setup for frequency modulation using nanoSurf PLL hardware

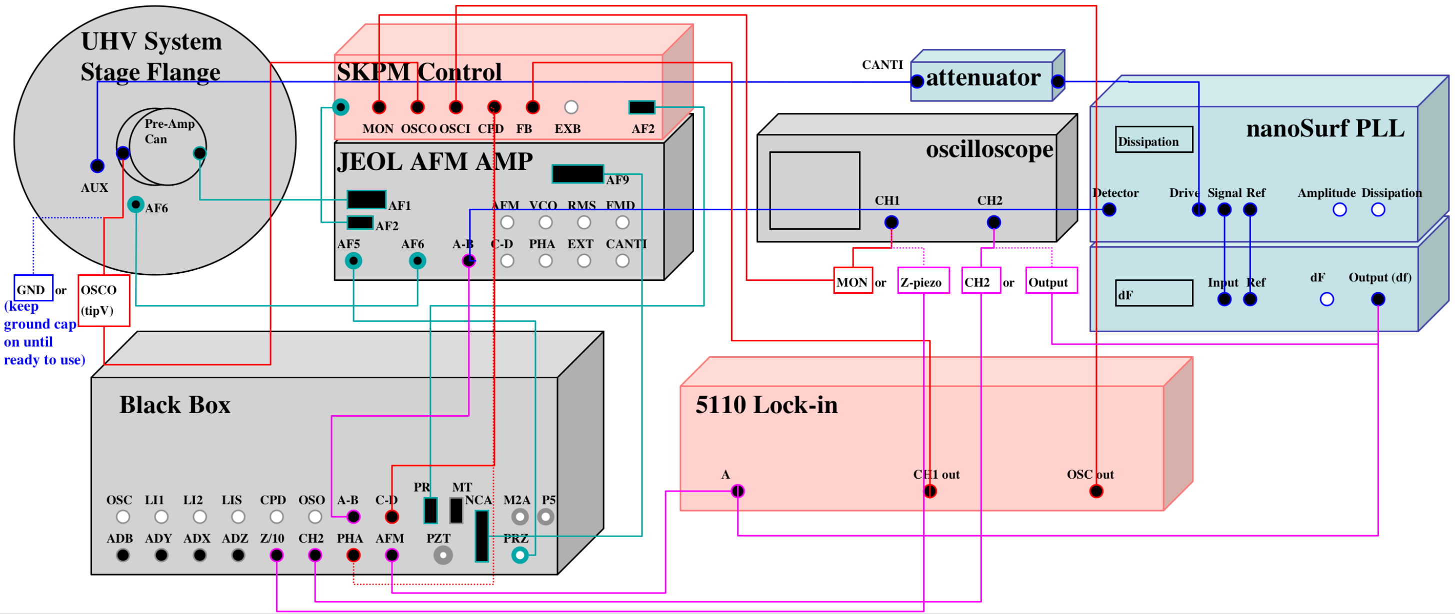

SKPM Control box:

- **SMM** means KPFM fback is **ON**
- **DS** means KPFM fback is **OFF**
- **SPC switch** is normally always **INT**
- **Gain= 5** (can change), analogous to fback gain in z-loop
- **Filter= 5** (can change), analogous to fback filter in z-loop (filter setting of 1 = very slow)

On the 5110 Lock-in:

- **Time constant** = 300ms to set phase, and 3 or 1 ms to image
- Make sure **%FS** and **XY** are lit
- **Sensitivity** = 50mV (adjust lower)
- **OSC F** = 700-992 Hz, >1KHz
- **BP** filter ON
- **Track** light ON
- **Line reject** light OFF
- **Reference** (INT) internal
- **Offset** OFF
- **Expand** OFF
- **Slope** = 6DB(book) or 12DB(Mr. Kitamura)
- **DYN reserve:** normal

To find the phase:

You want to match up the phase of the signals into and out of the lock in from the frequency shift (at that frequency component) and the AC voltage that will be applied to the tip

- Approach your tip normally (tip V grounded) and then back it off a little bit
- Change the tip V to OSCO
- Set the SKPM Control box mode to DS
- Set the time constant to about 300
- Use display 1 to set the frequency OSC F to ~992 Hz and voltage oscillations OSC LVL to ~0.7V (~2vpp)
- Use display 1 Auto-phase:
    - Go to Ref PH for phase
    - Press the red auto button and then press display 1, and a number will pop up
    - Repeat this. May need to change z-approach distance using the JEOL software or sensitivity
- Can test autophase by +90 (sig=0), +90 again (sig=-ve)

To image:

- Make sure JEOL software Bias/V Sample = 0
- **Acquisition:** 2 Inputs
- **Available:** Aux 3 or 2 (whichever CPD goes to on black box, C-D=Aux2 and PHA=Aux3)
- **Display Source:** Topography and Aux 3 or 2
- Change **time constant** back down to 3 or 1 ms
- Retract tip a bit, switch back to **SMM Mode**, then re-approach
- Set **Clock/ms** > Lock-in Time Constant, eg 6.667ms

Alternatively, to bias sample instead of tip:

- Ground the tip
- Attach bias (black box, ADB=add bias) to OSCO oscillator out of the KPFM unit
- In the scan advanced mode click "add external bias"
- Note: image reversed, bright=-, tip bias bright=+

Figure E.2: JEOL system setup for force gradient mode FM-KPFM

Bibliography

[1] C. D. Dimitrakopoulos and P. R. L. Malenfant. Organic thin film transistors for large area electronics. *Advanced Materials*, 14(2):99, 2002.

[2] G. Horowitz. Organic field-effect transistors. *Advanced Materials*, 10(5):365–377, 1998.

[3] Stephen R Forrest. The path to ubiquitous and low-cost organic electronic appliances on plastic. *Nature*, 428(6986):911–8, April 2004.

[4] G. Witte and C. Wöll. Growth of aromatic molecules on solid substrates for applications in organic electronics. *Journal of Materials Research*, 19(7):1889–1916, 2004.

[5] D. E. Hooks, T. Fritz, and M. D. Ward. Epitaxy and molecular organization on solid substrates. *Advanced Materials*, 13(4):227, 2001.

[6] C. Ludwig, B. Gompf, J. Petersen, R. Strohmaier, and W. Eisenmenger. STM investigations of PTCDA and PTCDI on graphite and MoS2 - a systematic study of epitaxy and STM image-contrast. *Zeitschrift Fur Physik B-Condensed Matter*, 93(3):365–373, 1994.

[7] P. M. Kazmaier and R. Hoffmann. A theoretical-study of crystallochromy - quantum interference effects in the spectra of perylene pigments. *Journal of the American Chemical Society*, 116(21):9684–9691, 1994.

[8] G. Klebe, 1994. data deposited at the Cambridge Crystallographic Data Center (CCDC), File CIF_LENPEZ, CSD N°55462.

[9] B. Uder, C. Ludwig, J. Petersen, B. Gompf, and W. Eisenmenger. STM characterization of organic-molecules on H-terminated Si(111). *Zeitschrift Fur Physik B-Condensed Matter*, 97(3):389–390, 1995.

[10] K. Tojo and J. Mizuguchi. Crystal structure of n,n ′-bis(2-phenylpropyl)perylene-3,4 : 9,10-bis(dicarboximide), C42H30N2O4. *Zeitschrift Fur Kristallographie-New Crystal Structures*, 217(4):517–518, 2002.

[11] O. Guillermet, A. Glachant, J. Y. Hoarau, J. C. Mossoyan, and M. Mossoyan. Perylene tetracarboxylic diimide ultrathin film deposition on Pt(100): a LEED, AES, REELS and STM study. *Surface Science*, 548(1-3):129–137, 2004.

[12] J. C. Swarbrick, J. Ma, J. A. Theobald, N. S. Oxtoby, J. N. O'Shea, N. R. Champness, and P. H. Beton. Square, hexagonal, and row phases of PTCDA and PTCDI on Ag-Si(111) $\sqrt{3}$ x $\sqrt{3}$R30°. *Journal of Physical Chemistry B*, 109(24):12167–12174, 2005.

[13] T. Kunstmann, A. Schlarb, M. Fendrich, Th. Wagner, R. Möller, and R. Hoffmann. Dynamic force microscopy study of 3,4,9,10-perylenetetracarboxylic dianhydride on KBr(001). *Phys. Rev. B*, 71(12):121403, Mar 2005.

[14] O. Guillermet, A. Glachant, M. Mossoyan, and J. C. Mossoyan. Near monolayer deposition of palladium phthalocyanine and perylene tetracarboxylic diimide on Au(001): A STM study. *Journal De Physique Iv*, 132:77–81, 2006.

[15] Markus Fendrich, Manfred Lange, Christian Weiss, Tobias Kunstmann, and Rolf Möller. N,N′-dimethylperylene-3,4,9,10-bis(dicarboximide) on alkali halide (001) surfaces. *Journal of Applied Physics*, 105(9):094311, 2009.

[16] S. A. Burke, W. Ji, J. M. Mativetsky, J. M. Topple, S. Fostner, H.-J. Gao, H. Guo, and P. Grütter. Strain induced dewetting of a molecular system: Bimodal growth of PTCDA on NaCl. *Phys. Rev. Lett.*, 100(18):186104, May 2008.

[17] B. R. Weinberger, M. Akhtar, and S. C. Gau. Polyacetylene photovoltaic devices. *Synthetic Metals*, 4(3):187 – 197, 1982.

[18] K. E. Trenberth, J. T. Fasullo, and J. Kiehl. Earth's global energy budget. *Bulletin of the American Meteorological Society*, 90:311–323, 2009.

[19] Linda E. Doman. *International Energy Outlook 2010*. U.S. Energy Information Administration, Office of Integrated Analysis and Forecasting. U.S. Department of Energy Washington, DC 20585, 2010.

[20] Michele Simmons and Peter Wong. *Solar Photovoltaic Cell/Module Manufacturing Activities 2009*. U.S. Energy Information Administration, Assistant Administrator for Energy Statistics. Office of Electricity, Renewables, and Uranium Statistics. U.S. Department of Energy Washington, D.C. 20585, 2011.

[21] Robert T. Eynon, Louise Guey-Lee, and Fred Mayes. *Renewable Energy Consumption and Electricity Preliminary Statistics 2010*. U.S. Energy Information Administration, Assistant Administrator for Energy Analysis. Office of Electricity, Coal, Nuclear, and Renewables. Renewable Analysis Team. U.S. Department of Energy Washington, DC 20585, 2011.

[22] Lawrence Kazmerski. Nrel best research-cell efficiencies, 2011.

[23] Ajay A. Virkar, Stefan Mannsfeld, Zhenan Bao, and Natalie Stingelin. Organic semiconductor growth and morphology considerations for organic thin-film transistors. *Advanced Materials*, 22(34):3857–3875, 2010.

[24] W. K. Burton, N. Cabrera, and F. C. Frank. The growth of crystals and the equilibrium structure of their surfaces. *Philosophical Transactions of the Royal Society of London Series a-Mathematical and Physical Sciences*, 243(866):299–358, 1951.

[25] John A. Venables. *Introduction to Surface and Thin Film Processes*. Cambridge University Press, Cambridge, 2000.

[26] Z. Y. Zhang and M. G. Lagally. Atomistic processes in the early stages of thin-film growth. *Science*, 276(5311):377–383, 1997.

[27] G. Binnig, C. F. Quate, and Ch. Gerber. Atomic force microscope. *Phys. Rev. Lett.*, 56(9):930–933, Mar 1986.

[28] Gerhard Meyer and Nabil M. Amer. Novel optical approach to atomic force microscopy. *Applied Physics Letters*, 53(12):1045–1047, 1988.

[29] L. Y. Beaulieu, Michel Godin, Olivier Laroche, Vincent Tabard-Cossa, and Peter Grütter. Calibrating laser beam deflection systems for use in atomic force microscopes and cantilever sensors. *Applied Physics Letters*, 88(8):083108, 2006.

[30] R. Erlandsson, G. M. McClelland, C. M. Mate, and S. Chiang. Atomic force microscopy using optical interferometry. *Journal of Vacuum Science Technology A: Vacuum, Surfaces, and Films*, 6(2):266 –270, mar 1988.

[31] M. Tortonese, H. Yamada, R.C. Barrett, and C.F. Quate. Atomic force microscopy using a piezoresistive cantilever. In *Solid-State Sensors and Actuators,*

1991. Digest of Technical Papers, TRANSDUCERS '91., 1991 International Conference on, pages 448 –451, jun 1991.

[32] J Brugger, R A Buser, and N F de Rooij. Micromachined atomic force microprobe with integrated capacitive read-out. *J. Micromech. Microeng*, 2:218–220, 1992.

[33] Franz J. Giessibl. Advances in atomic force microscopy. *Rev. Mod. Phys.*, 75(3):949–983, Jul 2003.

[34] Q. Zhong, D. Inniss, K. Kjoller, and V.B. Elings. Fractured polymer/silica fiber surface studied by tapping mode atomic force microscopy. *Surface Science Letters*, 290(1-2):L688 – L692, 1993.

[35] T. R. Albrecht, P. Grutter, D. Horne, and D. Rugar. Frequency-modulation detection using high-Q cantilevers for enhanced force microscope sensitivity. *Journal of Applied Physics*, 69(2):668–673, 1991.

[36] Seizo Morita, R. Wiesendanger, and E. Meyer. *Noncontact atomic force microscopy*. Nanoscience and technology. Springer, Berlin ; New York, 2002. 2002021665 S. Morita, R. Wiesendanger, E. Meyer, (eds.). ill. ; 25 cm. Includes bibliographical references and index.

[37] C.J. Chen. *Introduction to scanning tunneling microscopy*. Oxford series in optical and imaging sciences. Oxford University Press, 1993.

[38] S. Rast, C. Wattinger, U. Gysin, and E. Meyer. Dynamics of damped cantilevers. *Review of Scientific Instruments*, 71(7):2772–2775, 2000.

[39] Franz J. Giessibl. Forces and frequency shifts in atomic-resolution dynamic-force microscopy. *Phys. Rev. B*, 56(24):16010–16015, Dec 1997.

[40] M. Nonnenmacher, M. P. O'Boyle, and H. K. Wickramasinghe. Kelvin probe force microscopy. *Applied Physics Letters*, 58(25):2921–2923, 1991.

[41] W. A. Zisman. A new method of measuring contact potential differences in metals. *Review of Scientific Instruments*, 3(7):367 –370, jul 1932.

[42] Sir William Thomson. *Reprint of Papers on Electrostatics and Magnetism by Sir William Thomson, D.C.L., LL.D. F.R.S.E., Fellow of St. Peter's College, Cambridge, and Professor of Natural Philosophy in The University of Glasgow.* Printed by C. J. Clay and M. A. Sox, at the University Press, Cambridge, 1884.

[43] Wilhelm Melitz, Jian Shen, Andrew C. Kummel, and Sangyeob Lee. Kelvin probe force microscopy and its application. *Surface Science Reports*, 66(1):1 – 27, 2011.

[44] Y. Miyahara, L. Cockins and P. Grutter, "Electrostatic force microscopy characterization of low dimensional systems", In Kelving Probe Force Microscopy, S. Sadewasser and T. Glatzel (eds.), Springer-Verlag, Chap. 9, (2011).

[45] Dominik Ziegler and Andreas Stemmer. Force gradient sensitive detection in lift-mode Kelvin probe force microscopy. *Nanotechnology*, 22(7):075501, 2011.

[46] S. A. Burke, J. M. LeDue, Y. Miyahara, J. M. Topple, S. Fostner, and P. Grutter. Determination of the local contact potential difference of PTCDA on NaCl: a comparison of techniques. *Nanotechnology*, 20(26):264012, 2009.

[47] Ioan Notingher and Alistair Elfick. Effect of sample and substrate electric properties on the electric field enhancement at the apex of spm nanotips. *The Journal of Physical Chemistry B*, 109(33):15699–15706, 2005.

[48] S Fostner, A Tekiel, J M Topple, Y Miyahara, and P Grtter. Field deposition from metallic tips onto insulating substrates. *Nanotechnology*, 22(46):465301, 2011.

[49] S. Sadewasser and M. Ch. Lux-Steiner. Local surface photovoltage spectroscopy of Cu-phthalocyanine clusters on different substrates. *Journal of Vacuum Science & Technology B: Microelectronics and Nanometer Structures*, 28(3):C4D29, 2010.

[50] C. Kittel. *Introduction to solid state physics*. Wiley, 2005.

[51] D.A. Neamen. *Semiconductor Physics and Devices: Basic Principles*. Irwin, 1992. Third Edition.

[52] C Barth, T Hynninen, M Bieletzki, C R Henry, A S Foster, F Esch, and U Heiz. AFM tip characterization by Kelvin probe force microscopy. *New Journal of Physics*, 12(9):093024, 2010.

[53] Ingo Kröger, Benjamin Stadtmüller, Christoph Stadler, Johannes Ziroff, Mario Kochler, Andreas Stahl, Florian Pollinger, Tien-Lin Lee, Jörg Zegenhagen, Friedrich Reinert, and Christian Kumpf. Submonolayer growth of copper-phthalocyanine on Ag(111). *New Journal of Physics*, 12(8):083038, August 2010.

[54] M Della Pirriera, J Puigdollers, C Voz, M Stella, and J Bertomeu. Optoelectronic properties of CuPc thin films deposited at different substrate temperatures. *J. Phys. D: Appl. Phys.*, 42(14):145102, 2009.

[55] S. R. Forrest, L. Y. Leu, F. F. So, and W. Y. Yoon. Optical and electrical properties of isotype crystalline molecular organic heterojunctions. *Journal of Applied Physics*, 66(12):5908, 1989.

[56] Yuhki Terao, Hiroyuki Sasabe, and Chihaya Adachi. Correlation of hole mobility, exciton diffusion length, and solar cell characteristics in phthalocyanine/fullerene organic solar cells. *Applied Physics Letters*, 90(10):103515, 2007.

[57] V Singh, B Parsarathy, R Singh, a Aguilera, J Anthony, and M Payne. Characterization of high-photovoltage CuPc-based solar cell structures. *Solar Energy Materials and Solar Cells*, 90(6):798–812, April 2006.

[58] O Gordan, M Friedrich, and D Zahn. The anisotropic dielectric function for copper phthalocyanine thin films. *Organic Electronics*, 5(6):291–297, December 2004.

[59] Fan Yang, Max Shtein, and Stephen R. Forrest. Controlled growth of a molecular bulk heterojunction photovoltaic cell. *Nature Materials*, 4:37–41, 2005.

[60] J J Cox and T S Jones. The structure of copper phthalocyanine and the (111) a surfaces of InAs and InSb. *Surface Science*, 457:311–318, 2000.

[61] W. Ji, S.A. Burke, H.-J. Gao, P. Grutter, and H. Guo, 2008. (unpublished).

[62] R. T. Poole, J. G. Jenkin, J. Liesegang, and R. C. G. Leckey. Electronic band structure of the alkali halides. i. experimental parameters. *Phys. Rev. B*, 11:5179–5189, Jun 1975.

[63] R. T. Poole, J. Liesegang, R. C. G. Leckey, and J. G. Jenkin. Electronic band structure of the alkali halides. ii. critical survey of theoretical calculations. *Phys. Rev. B*, 11:5190–5196, Jun 1975.

[64] M. Mobus, N. Karl, and T. Kobayashi. Structure of perylene-tetracarboxylic-dianhydride thin-films on alkali-halide crystal substrates. *Journal of Crystal Growth*, 116(3-4):495–504, 1992.

[65] T. Fukuma, K. Kobayashi, K. Noda, K. Ishida, T. Horiuchi, H. Yamada, and K. Matsushige. Molecular-scale non-contact AFM studies of ferroelectric organic thin films epitaxially grown on alkali halides. *Surface Science*, 516(1-2):103–108, 2002.

[66] S. A. Burke, J. M. Mativetsky, R. Hoffmann, and P. Grütter. Nucleation and submonolayer growth of $C60$ on KBr. *Phys. Rev. Lett.*, 94(9):096102, Mar 2005.

[67] J. M. Mativetsky, S. A. Burke, S. Fostner, and P. Grutter. Templated growth of 3,4,9,10-perylenetetracarboxylic dianhydride molecules on a nanostructured insulator. *Nanotechnology*, 18(10):–, 2007.

[68] Jeffrey Mativetsky, PhD Thesis, Understanding and Controlling the Growth of Metals and Molecules on an Insulating Surface, McGill University 2010.

[69] K. J. Wan, X. F. Lin, and J. Nogami. Surface reconstructions in the Ag/Si(111) system. *Physical Review B*, 47(20):13700–13712, 1993.

[70] K. Thürmer, E. D. Williams, and J. E. Reutt-Robey. Dewetting dynamics of ultrathin silver films on Si(111). *Phys. Rev. B*, 68(15):155423, Oct 2003.

[71] B. Krause, A. C. Dürr, F. Schreiber, H. Dosch, and O. H. Seeck. Thermal stability and partial dewetting of crystalline organic thin films: 3,4,9,10-perylenetetracarboxylic dianhydride on Ag(111). *The Journal of Chemical Physics*, 119(6):3429–3435, 2003.

[72] Fabien Silly and Martin R. Castell. Bimodal growth of Au on SrTiO3(001). *Phys. Rev. Lett.*, 96(8):086104, Mar 2006.

[73] T. Dienel, C. Loppacher, S. C. B. Mannsfeld, R. Forker, and T. Fritz. Growth-mode-induced narrowing of optical spectra of an organic adlayer. *Advanced Materials*, 20(5):959, 2008.

[74] S. Kowarik, A. Gerlach, and F. Schreiber. Organic molecular beam deposition: fundamentals, growth dynamics, and in situ studies. *Journal of Physics-Condensed Matter*, 20(18):–, 2008.

[75] Y. Hirose, A. Kahn, V. Aristov, P. Soukiassian, V. Bulovic, and S. R. Forrest. Chemistry and electronic properties of metal-organic semiconductor interfaces: Al, Ti, In, Sn, Ag, and Au on PTCDA. *Physical Review B*, 54(19):13748–13758, 1996.

[76] S. Antohe, N. Tomozeiu, and S. Gogonea. Properties of the organic-on-inorganic semiconductor barrier contact diodes in PTCDI/P-Si and Ag/CuPc/P-Si. *Physica Status Solidi a-Applied Research*, 125(1):397–408, 1991.

[77] I. Horcas, R. Fernandez, J. M. Gomez-Rodriguez, J. Colchero, J. Gomez-Herrero, and A. M. Baro. WSXM: A software for scanning probe microscopy and a tool for nanotechnology. *Review of Scientific Instruments*, 78(1):–, 2007.

[78] A. S. Karkach. Trajectories and models of individual growth. *Demographic Research*, 15:348, 2006.

[79] D. Käfer, C. Wöll, and G. Witte. Thermally activated dewetting of organic thin films: the case of pentacene on SiO2 and gold. *Applied Physics A: Materials Science amp; Processing*, 95:273–284, 2009. 10.1007/s00339-008-5011-3.

[80] S. Berner, M. Brunner, L. Ramoino, H. Suzuki, H. J. Guntherodt, and T. A. Jung. Time evolution analysis of a 2D solid-gas equilibrium: a model system for molecular adsorption and diffusion. *Chemical Physics Letters*, 348(3-4):175–181, 2001.

[81] V.P. Zhdanov. Arrhenius parameters for rate processes on solid surfaces. *Surface Science Reports*, 12(5):185 – 242, 1991.

[82] J. M. Topple, S. A. Burke, W. Ji, S. Fostner, A. Tekiel, and P. Grütter. Tailoring the morphology and dewetting of an organic thin film. *The Journal of Physical Chemistry C*, 115(1):217–224, 2011.

[83] D. Y. Zhong, M. Hirtz, W. C. Wang, R. F. Dou, L. F. Chi, and H. Fuchs. Kinetics of island formation in organic film growth. *Phys. Rev. B*, 77(11):113404, Mar 2008.

[84] D. Choudhary, P. Clancy, R. Shetty, and F. Escobedo. A computational study of the sub-monolayer growth of pentacene. *Advanced Functional Materials*, 16(13):1768–1775, 2006.

[85] Ricardo Ruiz, Devashish Choudhary, Bert Nickel, Tullio Toccoli, Kee-Chul Chang, Alex C. Mayer, Paulette Clancy, Jack M. Blakely, Randall L. Headrick, Salvatore Iannotta, and George G. Malliaras. Pentacene thin film growth. *Chemistry of Materials*, 16(23):4497–4508, 2004.

[86] P. Schouwink, A. H. Schafer, C. Seidel, and H. Fuchs. The influence of molecular aggregation on the device properties of organic light emitting diodes. *Thin Solid Films*, 372(1-2):163 – 168, 2000.

[87] K. Tanaka and S. Fujita. Preparation and electrical characteristics of organic electroluminescent devices. *Proceedings of the 7th International Conference on Properties and Applications of Dielectric Materials (Cat. No.03CH37417)*, pages 45–48, 2003.

[88] Johannes V. Barth, Giovanni Costantini, and Klaus Kern. Engineering atomic and molecular nanostructures at surfaces. *Nature*, 437(7059):671–679, 2005.

[89] Ellen D. Williams. Nanoscale structures: Lability, length scales, and fluctuations. *MRS bulletin*, 29(9):621–629, 2004.

[90] S. A. Burke, J. M. Mativetsky, S. Fostner, and P. Grütter. $C60$ on alkali halides: Epitaxy and morphology studied by noncontact AFM. *Phys. Rev. B*, 76(3):035419, Jul 2007.

[91] J. M. Topple, S. A. Burke, S. Fostner, and P. Grütter. Thin film evolution: Dewetting dynamics of a bimodal molecular system. *Physical Review B*, 79(20):205414, May 2009.

[92] S. Fremy, A. Schwarz, K. Lammle, M. Prosenc, and R. Wiesendanger. The monomer-to-dimer transition and bimodal growth of Co-salen on NaCl(001): a high resolution atomic force microscopy study. *Nanotechnology*, 20(40):405608–405617, 2009.

[93] Akira Sasahara, Hiroshi Uetsuka, Taka aki Ishibashi, and Hiroshi Onishi. A needle-like organic molecule imaged by noncontact atomic force microscopy. *Applied Surface Science*, 188(3-4):265 – 271, 2002.

[94] L. Nony, R. Bennewitz, O. Pfeiffer, E. Gnecco, A. Baratoff, E. Meyer, T. Eguchi, A. Gourdon, and C. Joachim. Cu-TBPP and PTCDA molecules on insulating surfaces studied by ultra-high-vacuum non-contact AFM. *Nanotechnology*, 15:S91S96, 2004.

[95] O. H. Pakarinen, J. M. Mativetsky, A. Gulans, M. J. Puska, A. S. Foster, and P. Grutter. Role of van der waals forces in the adsorption and diffusion of organic molecules on an insulating surface. *Phys. Rev. B*, 80(8):085401, Aug 2009.

[96] Philipp Rahe, Markus Nimmrich, Andreas Greuling, Jens Schütte, Irena G. Stará, Jiří Rybáček, Gloria Huerta-Angeles, Ivo Starý, Michael Rohlfing, and Angelika Kühnle. Toward molecular nanowires self-assembled on an in-

sulating substrate: Heptahelicene-2-carboxylic acid on calcite (101?4). *The Journal of Physical Chemistry C*, 114(3):1547–1552, 2009.

[97] L. Nony, E. Gnecco, a. Baratoff, a. Alkauskas, R. Bennewitz, O. Pfeiffer, S. Maier, a. Wetzel, E. Meyer, and Ch. Gerber. Observation of Individual Molecules Trapped on a Nanostructured Insulator. *Nano Letters*, 4(11):2185–2189, November 2004.

[98] Sarah A. Burke, Jeffrey M. LeDue, Jessica M. Topple, Shawn Fostner, and Peter Grütter. Relating the functional properties of an organic semiconductor to molecular structure by nc-AFM. *Advanced Materials*, 21(20):2029–2033, 2009.

[99] M. Goryl, F. Buatier de Mongeot, F. Krok, A. Vevecka-Priftaj, and M. Szymonski. Leaky atomic traps: Upward diffusion of Au from nanoscale pits on ionic-crystal surfaces. *Phys. Rev. B*, 76(7):075423, Aug 2007.

[100] Jeffrey M. Mativetsky, Shawn Fostner, Sarah A. Burke, and Peter Grutter. The role of charge-induced defects in the growth of gold on an alkali halide surface. *Surface Science*, 602(4):L21–L24, 2008.

[101] Jeffrey M. Mativetsky, Shawn Fostner, Sarah A. Burke, and Peter Grutter. High-resolution investigation of metal nanoparticle growth on an insulating surface. *Phys. Rev. B*, 80(4):045430, Jul 2009.

[102] Jeffrey M Mativetsky, Sarah A Burke, Shawn Fostner, and Peter Grutter. Nanoscale pits as templates for building a molecular device. *Small (Weinheim an der Bergstrasse, Germany)*, 3(5):818–21, 2007.

[103] Th. Glatzel, L. Zimmerli, S. Koch, S. Kawai, and E. Meyer. Molecular assemblies grown between metallic contacts on insulating surfaces. *Applied Physics*

Letters, 94(6):063303, 2009.

[104] C Joachim, J K Gimzewski, and a Aviram. Electronics using hybrid-molecular and mono-molecular devices. *Nature*, 408(6812):541–8, November 2000.

[105] L. Venkataraman, J.E. Klare, C. Nuckolls, M.S. Hybertsen, and M.L. Steigerwald. Dependence of single molecule junction conductance on molecular conformation. *Arxiv preprint cond-mat/0607836*, 442(August):1–4, 2006.

[106] Kasper Moth-Poulsen and Thomas Bjø rnholm. Molecular electronics with single molecules in solid-state devices. *Nature nanotechnology*, 4(9):551–6, 2009.

[107] M. Fendrich and T. Kunstmann. Organic molecular nanowires: N,N′-dimethylperylene-3,4,9,10-bis(dicarboximide) on kbr(001). *Applied Physics Letters*, 91(2):023101, 2007.

[108] P W Tasker. The stability of ionic crystal surfaces. *Journal of Physics C: Solid State Physics*, 12(22):4977, 1979.

[109] An-Chang Shi and Michael Wortis. Relaxation of surface atoms in NaCl: Influence on the equilibrium crystal shape. *Phys. Rev. B*, 47(15):9804–9815, Apr 1993.

[110] Roland Bennewitz. Structured surfaces of wide band gap insulators as templates for overgrowth of adsorbates. *Journal of Physics: Condensed Matter*, 18(26):R417, 2006.

[111] Akira Sugawara, G. G. Hembree, and M. R. Scheinfein. Self-organized mesoscopic magnetic structures. *Journal of Applied Physics*, 82(11):5662–5669, 1997.

[112] Akira Sugawara and K. Mae. Nanoscale faceting of a NaCl(110) homoepitaxial layer. *Journal of Crystal Growth*, 237-239(Part 1):201 – 205, 2002.

[113] Jascha Repp, Gerhard Meyer, and Karl-Heinz Rieder. Snell's law for surface electrons: Refraction of an electron gas imaged in real space. *Phys. Rev. Lett.*, 92(3):036803, Jan 2004.

[114] Discussion with Roland Bennewitz (Leibniz Institute for New Materials) which took place during manuscript preparation in 2010 via email.

[115] Discussion with Paul Patrone (University of Maryland) which took place at Thin Films and Crystal Growth Mechanisms Gordon Research Conference, Thursday, July 21, 2011 in Biddeford, MA, USA.

[116] G. Benedek, S. Boffi, G. Caglioti, and J.C. Bilello. Surface energy for brittle fracture of alkali halides from lattice dynamics. *Surface Science*, 48(2):561 – 576, 1975.

[117] A.S. Krausz. The random walk theory of crack propagation. *Engineering Fracture Mechanics*, 12(4):499 – 504, 1979.

[118] Jeffrey M. Mativetsky, Yoichi Miyahara, Shawn Fostner, Sarah A. Burke, and Peter Grutter. Use of an electron-beam evaporator for the creation of nanostructured pits in an insulating surface. *Applied Physics Letters*, 88(23):233121, 2006.

[119] S Kawai, S Maier, S Koch, B Such, L Zimmerli, F Diederich, and E Meyer. Cutting and self-healing molecular wires studied by dynamic force microscopy. *Applied Physics Letters*, pages 93–95, 2009.

[120] G.A Bassett. A new technique for decoration of cleavage and slip steps on ionic crystal surfaces. *Philosophical Magazine*, 3(33):1042–1045, September 1958.

[121] Harald Hoppe and Niyazi Serdar Sariciftci. Morphology of polymer/fullerene bulk heterojunction solar cells. *J. Mater. Chem.*, 16:45–61, 2006.

[122] Zach M. Beiley, Eric T. Hoke, Rodrigo Noriega, Javier Dacua, George F. Burkhard, Jonathan A. Bartelt, Alberto Salleo, Michael F. Toney, and Michael D. McGehee. Morphology-dependent trap formation in high performance polymer bulk heterojunction solar cells. *Advanced Energy Materials*, 2011.

[123] Sarah R. Cowan, Wei Lin Leong, Natalie Banerji, Gilles Dennler, and Alan J. Heeger. Identifying a threshold impurity level for organic solar cells: Enhanced first-order recombination via well-defined PC84BM traps in organic bulk heterojunction solar cells. *Advanced Functional Materials*, 21(16):3083–3092, 2011.

[124] Patrick G Nicholson and Fernando A Castro. Organic photovoltaics: principles and techniques for nanometre scale characterization. *Nanotechnology*, 21(49):492001, 2010.

[125] Craig H. Peters, I. T. Sachs-Quintana, John P. Kastrop, Serge Beaupr, Mario Leclerc, and Michael D. McGehee. High efficiency polymer solar cells with long operating lifetimes. *Advanced Energy Materials*, 1(4):491–494, 2011.

[126] Andrea Liscio, Vincenzo Palermo, and Paolo Samori. Nanoscale quantitative measurement of the potential of charged nanostructures by electrostatic and

Kelvin probe force microscopy: Unraveling electronic processes in complex materials. *Accounts of Chemical Research*, 43(4):541–550, 2010.

[127] David C. Coffey and David S. Ginger. Time-resolved electrostatic force microscopy of polymer solar cells. *Nat Mater*, 5(9):735–740, 2006.

[128] Xiaoniu Yang, Joachim Loos, Sjoerd C. Veenstra, Wiljan J. H. Verhees, Martijn M. Wienk, Jan M. Kroon, Matthias A. J. Michels, and René A. J. Janssen. Nanoscale morphology of high-performance polymer solar cells. *Nano Letters*, 5(4):579–583, 2005.

[129] Mariano Campoy-Quiles, Toby Ferenczi, Tiziano Agostinelli, Pablo G. Etchegoin, Youngkyoo Kim, Thomas D. Anthopoulos, Paul N. Stavrinou, Donal D. C. Bradley, and Jenny Nelson. Morphology evolution via self-organization and lateral and vertical diffusion in polymer:fullerene solar cell blends. *Nat Mater*, 7(2):158–164, 2008.

[130] Jean Roncali. Molecular bulk heterojunctions: An emerging approach to organic solar cells. *Accounts of Chemical Research*, 42(11):1719–1730, 2009.

[131] Jose L. Segura, Nazario Martin, and Dirk M. Guldi. Materials for organic solar cells: the C60/π-conjugated oligomer approach. *Chem. Soc. Rev.*, 34:31–47, 2005.

[132] Serap Günes, Helmut Neugebauer, and Niyazi Serdar Sariciftci. Conjugated polymer-based organic solar cells. *Chemical Reviews*, 107(4):1324–1338, 2007.

[133] Frederik C. Krebs. Fabrication and processing of polymer solar cells: A review of printing and coating techniques. *Solar Energy Materials and Solar Cells*, 93(4):394 – 412, 2009. Processing and Preparation of Polymer and Organic Solar Cells.

[134] Markus Hallermann, Enrico Da Como, Jochen Feldmann, Marta Izquierdo, Salvatore Filippone, Nazario Martn, Sabrina Jčhter, and Elizabeth von Hauff. Correlation between charge transfer exciton recombination and photocurrent in polymer/fullerene solar cells. *Applied Physics Letters*, 97(2):023301, 2010.

[135] Bernard Kippelen and Jean-Luc Bredas. Organic photovoltaics. *Energy Environ. Sci.*, 2:251–261, 2009.

[136] Holger Spanggaard and Frederik C. Krebs. A brief history of the development of organic and polymeric photovoltaics. *Solar Energy Materials and Solar Cells*, 83(2-3):125 – 146, 2004. The development of organic and polymer photovoltaics.

[137] Peter Peumans, Aharon Yakimov, and Stephen R. Forrest. Small molecular weight organic thin-film photodetectors and solar cells. *J. Appl. Phys.*, 93(7):3693–3723, 2003.

[138] Michael Gratzel. Photoelectrochemical cells. *Nature*, 414(6861):338–344, Nov 2001.

[139] Takuya Matsui, Riza Muhida, Tomohiro Kawamura, Toshihiko Toyama, Hiroaki Okamoto, Tsutomu Yamazaki, Shinya Honda, Hideyuki Takakura, and Yoshihiro Hamakawa. Microstructural dependence of electron and hole transport in low-temperature-grown polycrystalline-silicon thin-film solar cells. *App. Phys. Lett.*, 81(25):4751–4753, 2002.

[140] X.-Y. Zhu, Q. Yang, and M. Muntwiler. Charge-transfer excitons at organic semiconductor surfaces and interfaces. *Accounts of Chemical Research*, 42(11):1779–1787, 2009.

[141] Jablonski Energy Diagram invented by Professor Alexander Jablonski in 1935, illustration modeled after Olympus Microscopy Resource Centre entry by Ian D. Johnson and Michael W. Davidson - National High Magnetic Field Laboratory, 1800 East Paul Dirac Dr., The Florida State University, Tallahassee, Florida, 32310.

[142] Frank C. Spano. The spectral signatures of frenkel polarons in H- and J-aggregates. *Accounts of Chemical Research*, 43(3):429–439, 2010.

[143] Francis Paquin, Gianluca Latini, Maciej Sakowicz, Paul-Ludovic Karsenti, Linjun Wang, David Beljonne, Natalie Stingelin, and Carlos Silva. Charge separation in semicrystalline polymeric semiconductors by photoexcitation: Is the mechanism intrinsic or extrinsic? *Phys. Rev. Lett.*, 106:197401, May 2011.

[144] J. Frenkel. On the transformation of light into heat in solids. I. *Phys. Rev.*, 37(1):17–44, Jan 1931.

[145] Gregory H. Wannier. The structure of electronic excitation levels in insulating crystals. *Phys. Rev.*, 52(3):191–197, Aug 1937.

[146] Jiye Lee, Koen Vandewal, Shane R. Yost, Matthias E. Bahlke, Ludwig Goris, Marc A. Baldo, Jean V. Manca, and Troy Van Voorhis. Charge transfer state versus hot exciton dissociation in polymer-fullerene blended solar cells. *Journal of the American Chemical Society*, 132(34):11878–11880, 2010.

[147] Discussion with Françoise Provencher (Université de Montreal) which took place at the 9th International Conference on Optical Probes of Conjugated Polymers and Organic Nanostructures and 5th International Conference on

Excited State Processes in Electronic and Bio Nanomaterials, June 19-24, 2011 in Santa Fe, NM, USA.

[148] Jean-Luc Brédas, Joseph E. Norton, Jérm̂e Cornil, and Veaceslav Coropceanu. Molecular understanding of organic solar cells: The challenges. *Accounts of Chemical Research*, 42(11):1691–1699, 2009.

[149] Denis E. Markov, Emiel Amsterdam, Paul W. M. Blom, Alexander B. Sieval, and Jan C. Hummelen. Accurate measurement of the exciton diffusion length in a conjugated polymer using a heterostructure with a side-chain cross-linked fullerene layer. *The Journal of Physical Chemistry A*, 109(24):5266–5274, 2005.

[150] Jessica E. Kroeze, Tom J. Savenije, Martien J. W. Vermeulen, and John M. Warman. Contactless determination of the photoconductivity action spectrum, exciton diffusion length, and charge separation efficiency in polythiophene-sensitized TiO2 bilayers. *The Journal of Physical Chemistry B*, 107(31):7696–7705, 2003.

[151] Thomas Stübinger and Wolfgang Brütting. Exciton diffusion and optical interference in organic donor-acceptor photovoltaic cells. *Applied Physics Letters*, 90(7):3632–3641, 2001.

[152] Jiangeng Xue, Soichi Uchida, Barry P. Rand, and Stephen R. Forrest. Asymmetric tandem organic photovoltaic cells with hybrid planar-mixed molecular heterojunctions. *Applied Physics Letters*, 85(23):5757–5759, 2004.

[153] O. Ostroverkhova, D. G. Cooke, F. A. Hegmann, J. E. Anthony, V. Podzorov, M. E. Gershenson, O. D. Jurchescu, and T. T. M. Palstra. Ultrafast carrier

dynamics in pentacene, functionalized pentacene, tetracene, and rubrene single crystals. *Applied Physics Letters*, 88(16):162101, 2006.

[154] S.H. Park, Anshuman Roy, S. Beaupré, Shinuk Cho, Nelson Coates, J.S. Moon, Daniel Moses, Mario Leclerc, Kwanghee Lee, and A.J. Heeger. Bulk heterojunction solar cells with internal quantum efficiency approaching 100%. *Nature Photonics*, 3(5):297–302, 2009.

[155] Chenggang Tao, Jibin Sun, Xiaowei Zhang, Ryan Yamachika, Daniel Wegner, Yasaman Bahri, Georgy Samsonidze, Marvin L. Cohen, Steven G. Louie, T. Don Tilley, Rachel A. Segalman, and Michael F. Crommie. Spatial resolution of a type II heterojunction in a single bipolar molecule. *Nano Letters*, 9(12):3963–3967, 2009.

[156] N. Karl. Charge carrier transport in organic semiconductors. *Synthetic Metals*, 133-134:649 – 657, 2003. Proceedings of the Yamada Conference LVI. The Fourth International.

[157] Veaceslav Coropceanu, Jérôme Cornil, Demetrio A. da Silva Filho, Yoann Olivier, Robert Silbey, and Jean-Luc Brédas. Charge transport in organic semiconductors. *Chemical Reviews*, 107(4):926–952, 2007.

[158] S. F. Nelson, Y.-Y. Lin, D. J. Gundlach, and T. N. Jackson. Temperature-independent transport in high-mobility pentacene transistors. *Appl. Phys. Lett.*, 72(15):1854–1856, 1998.

[159] T. Meoded, R. Shikler, N. Fried, and Y. Rosenwaks. Direct measurement of minority carriers diffusion length using Kelvin probe force microscopy. *Appl. Phys. Lett.*, 75(16):2435–2437, 1999.

[160] H. Hoppe, T. Glatzel, M. Niggemann, A. Hinsch, M. Ch. Lux-Steiner, and N. S. Sariciftci. Kelvin probe force microscopy study on conjugated polymer/fullerene bulk heterojunction organic solar cells. *Nano Letters*, 5(2):269–274, 2005.

[161] David C. Coffey, Obadiah G. Reid, Deanna B. Rodovsky, Glenn P. Bartholomew, and David S. Ginger. Mapping local photocurrents in polymer/fullerene solar cells with photoconductive atomic force microscopy. *Nano Letters*, 7(3):738–744, 2007.

[162] V. Palermo, G. Ridolfi, A.M. Talarico, L. Favaretto, G. Barbarella, N. Camaioni, and P. Samor. A Kelvin probe force microscopy study of the photogeneration of surface charges in all-thiophene photovoltaic blends. *Advanced Functional Materials*, 17(3):472–478, 2007.

[163] Tatsuo Mori, Takuya Ogawa, Don-Chan Cho, and Teruyoshi Mizutani. A discussion of conduction in organic light-emitting diodes. *Applied Surface Science*, 212-213:458 – 463, 2003. 11th International Conference on Solid Films and Surfaces.

[164] Basics of measuring the dielectric properties of materials, 1992. Application note 1217-1, Literature number 5091-3300E.

[165] Oskar Armbruster, Christoph Lungenschmied, and Siegfried Bauer. Dielectric response of doped organic semiconductor devices: P3HT:PCBM solar cells. *Phys. Rev. B*, 84:085208, Aug 2011.

[166] M.M. El-Nahass, H.M. Zeyada, M.S. Aziz, and N.A. El-Ghamaz. Carrier transport mechanisms and photovoltaic properties of Au/p-ZnPc/p-Si solar cell. *Solid-State Electronics*, 49(8):1314 – 1319, 2005.

[167] S. a. James, a. K. Ray, and J. Silver. Dielectric and Optical Studies of Sublimed MoOPc Films. *Physica Status Solidi (a)*, 129(2):435–441, February 1992.

[168] I. Thurzo, G. Pham, T. U. Kampen, and D. R. T. Zahn. Transient charging of copper phthalocyanine: model and experiment. *Thin Solid Films*, 433(1-2):292 – 297, 2003. Proceedings from the 12th International Conference on Thin Films.

[169] S. Havriliak. and S. Negami. A complex plane representation of dielectric and mechanical relaxation processes in some polymers. *J. Polym. Sci. Part D*, 99(14):161–210, 1966.

[170] Inho Kim, Hanna M. Haverinen, Zixing Wang, Sijesh Madakuni, Jian Li, and Ghassan E. Jabbour. Effect of molecular packing on interfacial recombination of organic solar cells based on palladium phthalocyanine and perylene derivatives. *Applied Physics Letters*, 95(2):023305, 2009.

[171] Jianfeng Pan, Weihong Zhu, Shangfeng Li, Wenjin Zeng, Yong Cao, and He Tian. Dendron-functionalized perylene diimides with carrier-transporting ability for red luminescent materials. *Polymer*, 46(18):7658 – 7669, 2005. Stimuli Responsive Polymers, IUPAC MACRO 2004.

[172] Jiun-Haw Lee, Chi-Chih Liao, Pier-Jy Hu, and Yih Chang. High contrast ratio organic light-emitting devices based on CuPC as electron transport material. *Synthetic Metals*, 144(3):279 – 283, 2004.

[173] P. Peumans and S. R. Forrest. Very-high-efficiency double-heterostructure copper phthalocyanine/C60 photovoltaic cells. *Appl. Phys. Lett.*, 79(1):126–128, 2001.

[174] I.G. Hill, A. Kahn, Z.G. Soos, R.A. Pascal, and Jr. Charge-separation energy in films of -conjugated organic molecules. *Chemical Physics Letters*, 327(3-4):181 – 188, 2000.

[175] J. Mizuguchi and K. Tojo. Electronic structure of perylene pigments as viewed from the crystal structure and excitonic interactions. *The Journal of Physical Chemistry B*, 106(4):767–772, 2002.

[176] A. J. Ferguson and T. S. Jones. Photophysics of PTCDA and Me-PTCDI thin films: Effects of growth temperature. *The Journal of Physical Chemistry B*, 110(13):6891–6898, 2006.

[177] Françoise Provencher, Jean-Frédéric Laprade, Michel Côté, and Carlos Silva. Excitons in perylene tetracarboxdiimide crystals for optoelectronics. *physica status solidi (c)*, 6(1):93–96, 2009.

[178] O. D. Gordan, S. Hermann, M. Friedrich, and D. R. T. Zahn. Optical properties of 3,4,9,10-perylenetetracarboxylic dianhydride/copper phthalocyanine superlattices. *J. Appl. Phys.*, 97(6):063518, 2005.

[179] L. Smilowitz, N. S. Sariciftci, R. Wu, C. Gettinger, A. J. Heeger, and F. Wudl. Photoexcitation spectroscopy of conducting-polymer C_{60} composites: Photoinduced electron transfer. *Phys. Rev. B*, 47:13835–13842, May 1993.

[180] Jesús Zúñiga Pérez, Vicente Muñoz Sanjosé, Elisa Palacios-Lidón, and Jaime Colchero. Polarity effects on ZnO films grown along the nonpolar $[11\overline{2}0]$ direction. *Phys. Rev. Lett.*, 95:226105, Nov 2005.

[181] J Zúñiga Pérez, V Muñoz Sanjosé, E Palacios-Lidón, and J Colchero. Facets evolution and surface electrical properties of nonpolar m-plane ZnO thin films. *Appl. Phys. Lett.*, 88(26):261912, 2006.

[182] B Pérez-García, J Abad, A Urbina, J Colchero, and E Palacios-Lidón. Surface potential domains on lamellar P3OT structures. *Nanotechnology*, 19(6):065709, 2008.

[183] Marco Chiesa, Lukas Bürgi, Ji-Seon Kim, Rafi Shikler, Richard H. Friend, and Henning Sirringhaus. Correlation between surface photovoltage and blend morphology in polyfluorene-based photodiodes. *Nano Letters*, 5(4):559–563, 2005.

[184] Obadiah G. Reid, Glennis E. Rayermann, David C. Coffey, and David S. Ginger. Imaging local trap formation in conjugated polymer solar cells: A comparison of time-resolved electrostatic force microscopy and scanning Kelvin probe imaging. *The Journal of Physical Chemistry C*, 114(48):20672–20677, 2010.

[185] Markus Hallermann, Ilka Kriegel, Enrico Da Como, Josef M. Berger, Elizabeth von Hauff, and Jochen Feldmann. Charge transfer excitons in polymer/fullerene blends: The role of morphology and polymer chain conformation. *Advanced Functional Materials*, 19(22):3662–3668, 2009.

[186] R. Alex Marsh, Justin M. Hodgkiss, and Richard H. Friend. Direct measurement of electric field-assisted charge separation in polymer:fullerene photovoltaic diodes. *Advanced Materials*, 22(33):3672–3676, 2010.

[187] Shawn Fostner, PhD Thesis, Ultra high vacuum fabrication of metallic contacts for molecular devices on an insulating surface, McGill University 2010.

[188] Ashok K. Vijh. A correlation between the magnitudes of dielectric breakdown fields in alkali halides and their lattice constants. *Journal of Materials Science*, 9:2052–2053, 1974. 10.1007/BF00540554.

[189] Mohammed A. Baklar, Felix Koch, Avinesh Kumar, Ester Buchaca Domingo, Mariano Campoy-Quiles, Kirill Feldman, Liyang Yu, Paul Wobkenberg, James Ball, Rory M. Wilson, Iain McCulloch, Theo Kreouzis, Martin Heeney, Thomas Anthopoulos, Paul Smith, and Natalie Stingelin. Solid-state processing of organic semiconductors. *Advanced Materials*, 22(35):3942–3947, 2010.

[190] G. Beernink, T. Strunskus, G. Witte, and Ch. Woll. Importance of dewetting in organic molecular-beam deposition: Pentacene on gold. *Applied Physics Letters*, 85(3):398 –400, jul 2004.

[191] G. Witte, K. Hänel, S. Söhnchen, and Ch. Wöll. Growth and morphology of thin films of aromatic molecules on metals: the case of perylene. *Applied Physics A: Materials Science and Processing*, 82:447–455, 2006. 10.1007/s00339-005-3367-1.

[192] Daniel Käfer, Lars Ruppel, and Gregor Witte. Growth of pentacene on clean and modified gold surfaces. *Phys. Rev. B*, 75(8):085309, Feb 2007.

[193] Toshiyuki Kakudate, Noriyuki Yoshimoto, Koji Kawamura, and Yoshio Saito. Observation of epitaxial growth of pentacene thin films on KCl substrate by x-ray diffractometry. *Journal of Crystal Growth*, 306(1):27 – 32, 2007.

[194] Noriyuki Yoshimoto, Koji Kawamura, Toshiyuki Kakudate, Yasukiyo Ueda, and Yoshio Saito. Epitaxial relationships of pentacene polymorphs on KCI (001). *Molecular Crystals and Liquid Crystals*, 462(1):21 – 27, 2007.

[195] Jascha Repp, Gerhard Meyer, Sladjana M. Stojković, André Gourdon, and Christian Joachim. Molecules on insulating films: Scanning-tunneling

microscopy imaging of individual molecular orbitals. *Phys. Rev. Lett.*, 94:026803, Jan 2005.

[196] Leo Gross, Fabian Mohn, Nikolaj Moll, Peter Liljeroth, and Gerhard Meyer. The chemical structure of a molecule resolved by atomic force microscopy. *Science*, 325(5944):1110–1114, 2009.

[197] Kung-Ching Liao, Ahmad G. Ismail, Laurent Kreplak, Jeffrey Schwartz, and Ian G. Hill. Designed organophosphonate self-assembled monolayers enhance device performance of pentacene-based organic thin-film transistors. *Advanced Materials*, 22(28):3081–3085, 2010.

[198] S. Yoo, B. Domercq, and B. Kippelen. Efficient thin-film organic solar cells based on pentacene/C60 heterojunctions. *Appl. Phys. Lett.*, 85(22):5427–5429, 2004.

[199] Ajay K. Pandey and Jean-Michel Nunzi. Efficient flexible and thermally stable pentacene/C60 small molecule based organic solar cells. *Appl. Phys. Lett.*, 89(21):213506, 2006.

[200] Ajay K. Pandey, Sylvie Dabos-Seignon, and Jean-Michel Nunzi. Pentacene: PTCDI-C13H27 molecular blends efficiently harvest light for solar cell applications. *Appl. Phys. Lett.*, 89(11):113506, 2006.

[201] David Cheyns, Hans Gommans, Mathieu Odijk, Jef Poortmans, and Paul Heremans. Stacked organic solar cells based on pentacene and. *Solar Energy Materials and Solar Cells*, 91(5):399 – 404, 2007. Selected Papers from the European Conference on Hybrid and Organic Solar Cells -ECHOS '06 - European Conference on Hybrid and Organic Solar Cells.

[202] Martijn M. Wienk, Jan M. Kroon, Wiljan J. H. Verhees, Joop Knol, Jan C. Hummelen, Paul A. van Hal, and René A. J. Janssen. Efficient methano[70]fullerene/MDMO-PPV bulk heterojunction photovoltaic cells. *Angewandte Chemie International Edition*, 42(29):3371–3375, 2003.

[203] N. Vandewalle, M. Ausloos, and R. Cloots. Formation of nick instabilities due to particle clustering along crystal interfaces. *Phys. Rev. E*, 56:4042–4047, Oct 1997.

[204] F. G. J. Perey and E. R. Pounder. Crystal orientation in ice sheets. *Canadian Journal of Physics*, 36(4):494–502, 1958.

[205] D. Cullen and I. Baker. Observation of impurities in ice. *Microscopy Research and Technique*, 55(3):198–207, 2001.

[206] I Baker, D Cullen, and D Iliescu. The microstructural location of impurities in ice. *Canadian Journal of Physics*, 81(1-2):1–9, 2003.

[207] Francesco Buatier de Mongeot, Wenguang Zhu, A. Molle, R. Buzio, C. Boragno, U. Valbusa, E. G. Wang, and Zhenyu Zhang. Nanocrystal formation and faceting instability in Al(110) homoepitaxy: *True* upward adatom diffusion at step edges and island corners. *Phys. Rev. Lett.*, 91:016102, Jul 2003.

[208] Wenguang Zhu, Francesco Buatier de Mongeot, U. Valbusa, E. G. Wang, and Zhenyu Zhang. Adatom ascending at step edges and faceting on fcc metal (110) surfaces. *Phys. Rev. Lett.*, 92:106102, Mar 2004.

[209] A. Shabaev, Al. L. Efros, and A. J. Nozik. Multiexciton generation by a single photon in nanocrystals. *Nano Letters*, 6(12):2856–2863, 2006.

[210] Discussion of Multiple Excition Generation Session (featuring Victor Klimov and others), which took place Thursday, June 23, 2011 at The 9th International Conference on Optical Probes of Conjugated Polymers and Organic Nanostructures combined with The 5th Conference on Excited State Processes on Electronic and Bio Nanomaterials in Santa Fe, New Mexico, USA.

[211] Paul M. Zimmerman, Zhiyong Zhang, and Charles B. Musgrave. Singlet fission in pentacene through multi-exciton quantum states. *Nat Chem*, 4(8):648–652, 2010.

[212] Priya J. Jadhav, Aseema Mohanty, Jason Sussman, Jiye Lee, and Marc A. Baldo. Singlet exciton fission in nanostructured organic solar cells. *Nano Letters*, 11(4):1495–1498, 2011.

[213] P. Peumans, V. Bulovic, and S. R. Forrest. Efficient photon harvesting at high optical intensities in ultrathin organic double-heterostructure photovoltaic diodes. *Appl. Phys. Lett.*, 76(19):2650–2652, 2000.

[214] Sebastian Knabe, Nazila Soleimani, Tom Markvart, and Gottfried Heinrich Bauer. Efficient light trapping in a fluorescence solar collector by 3D photonic crystal. *physica status solidi (RRL) Rapid Research Letters*, 4(5-6):118–120, 2010.

[215] Jinming Cai, Pascal Ruffieux, Rached Jaafar, Marco Bieri, Thomas Braun, Stephan Blankenburg, Matthias Muoth, Ari P. Seitsonen, Moussa Saleh, Xinliang Feng, Klaus Mullen, and Roman Fasel. Atomically precise bottom-up fabrication of graphene nanoribbons. *Nature*, 466(7305):470–473, 2010.

[216] Discussions with Chris Godbout and Amy Szuchmacher Blum of the McGill University Chemistry Department that took place in September, 2010.

[217] Markus Kittelmann, Philipp Rahe, Markus Nimmrich, Christopher M. Hauke, Andreé Gourdon, and Angelika Kuühnle. On-surface covalent linking of organic building blocks on a bulk insulator. *ACS Nano*, 0(0), 2011.